Study on Dye Sensitized Solar Cells for Improved Performances

Yimhyun Jo

Department of Chemical Engineering

Graduate school of UNIST

Study on Dye Sensitized Solar Cells for Improved Performances

A dissertation
submitted to the Graduate School of UNIST
in partial fulfillment of the
requirements for the degree of
Doctor of Philosophy

Yimhyun Jo

07. 08. 2014

Approved by
_____
Advisor
Jae Sung Lee

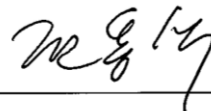# The Study on dye sensitized solar cells for improvement of the performance

Yimhyun Jo

This certifies that dissertation of Yimhyun Jo is approved.
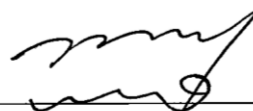
07. 08. 2014

_____
Advisor: Jae Sung Lee

_____
Yongseok Jun

_____
Dongsuk Kim

_____
Jin Young Kim

_____
Tae-Hyuk Kwon

Contents

Abstract

This thesis is focused on the improvement of performance of DSC. Unique materias as Zno, odered mesoporous carbon, graphene-metal nonoparticle composit was introduced to DSC to deveolp the performance.

In this thesis ZnO with novel nanostructure was introdueced with adventage of large surface area and good morphology for penetrating of the dye solution. This work provides intriguing way of structurally designing of ZnO with large surface area and moderate morphology for DSSCs and other applications.

rGO/metal nanoparticle hybrid films and OMC–CNT, where the primary particles of the OMCs are interconnected via the CNTs are introduced for counter electrodes in DSC as Pt replacement counter electrode. The enhanced electrochemical stability of the Au nanoparticles on rGO was attributed to the unique combination of the presence of defects as well as hydroxyl and carboxyl functional groups. the OMC–CNT-based cell showed an excellent cell efficiency which was primarily attributed to its remarkably enhanced electrical conductivity as well as its intrinsic catalytic activity. This work provides an intriguing way of structurally designing a low-cost, Pt-free, high-performance counter electrode material for DSC.

New coating method for DSC working-electrode is introduced, too. The method controls the reaction temperatures with concentrations of N719 in various solvents. Sorts of alcohols and DMSO was invetigaed and can be ideally applied to shorten the coating time to only 3 min which is much improved from the several hour scale needed for the conventional solvents such as acetonitrile and ethanol. The cells were compared by characterization with JV measurement, dye uptake amount, DRIFT, and EIS. Performance and other characteristics of the cells with working electrodes prepared by this new methods were very comparable to those prepared by conventional methods

Chapter 1. Introduction

1.1. Background

1.1.1. The Sun as unlimited energy resource

There are many reason for researching solar energy while fossil fuel is still mainly used for global energy resource. Enormous fossil fuel buried underground enable pursue consuming life style using vehicles and electrical goods for convenience and comfort. It also accelerates progress of technology which need more energy. Energy consumption estimate for seven billion people in the world is about 13 TW and it will go up to 20 TW in 30 years. However fossil fuel resource is limited and used up rapidly with emitting CO_2. Carbon contained fossil fuel burning contribute to increase the concentration of CO_2 in atmosphere which consider as cause a sudden change of greenhouse gas. Increasing concentration of greenhouse gas in atmosphere prevents the normal escape of energy to space from the earth and lead to the temperature of the surface of the earth go up steadily. This phenomenon could lead to changes in wind patterns may cause extension of desert at inland and the oceans to rise. Figure 1-1. show annual global temperature rise and anomaly.
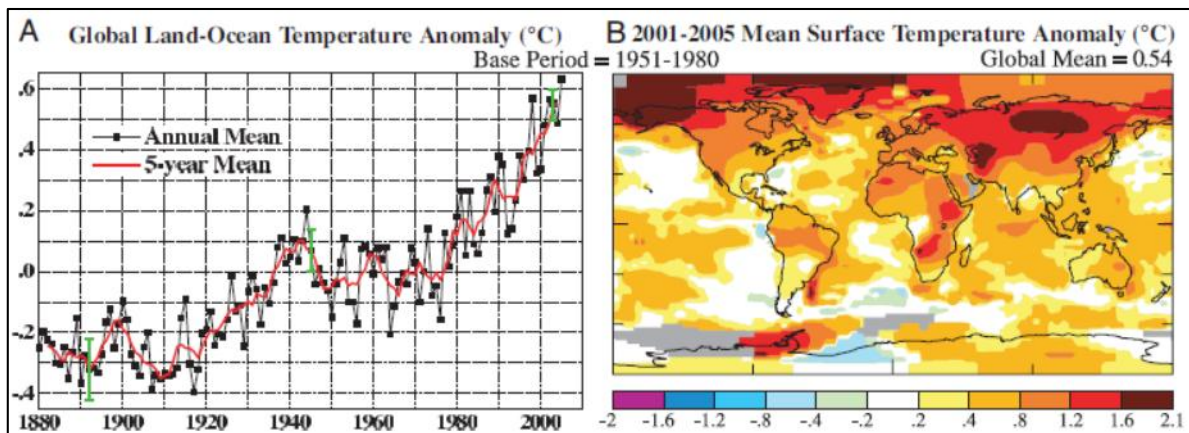
Figure 1-1. (A) Annual global temperature (B) Temperature anomaly[1]

Hence alternative energy resources to meet the demand of the day is urgent to keep the life style and reduce CO_2 emission. Solar energy is ubiquitous and sustainable resource. The total solar energy absorbed by the earth's surface is approximately 3.85×10^{24} J per year. The energy for human civilization for one year is just one hour energy from the sunshine at the earth.[2] The amount of energy get from the sun in a year surpasses buried total fossil fuel with uranium for nuclear generation. Other renewable energy resources as photosynthesis (biomass), hydro power and wind power are small part of the solar energy. (Figure 1-2.) So If the tiny part of that sunlight, which is ubiqutous but not econimical, were captured efficiently by solar cells that turn light energy to electricity, energy problem

would be solved. Solar cell is a simple and promising method of harnessing the energy of the sun.
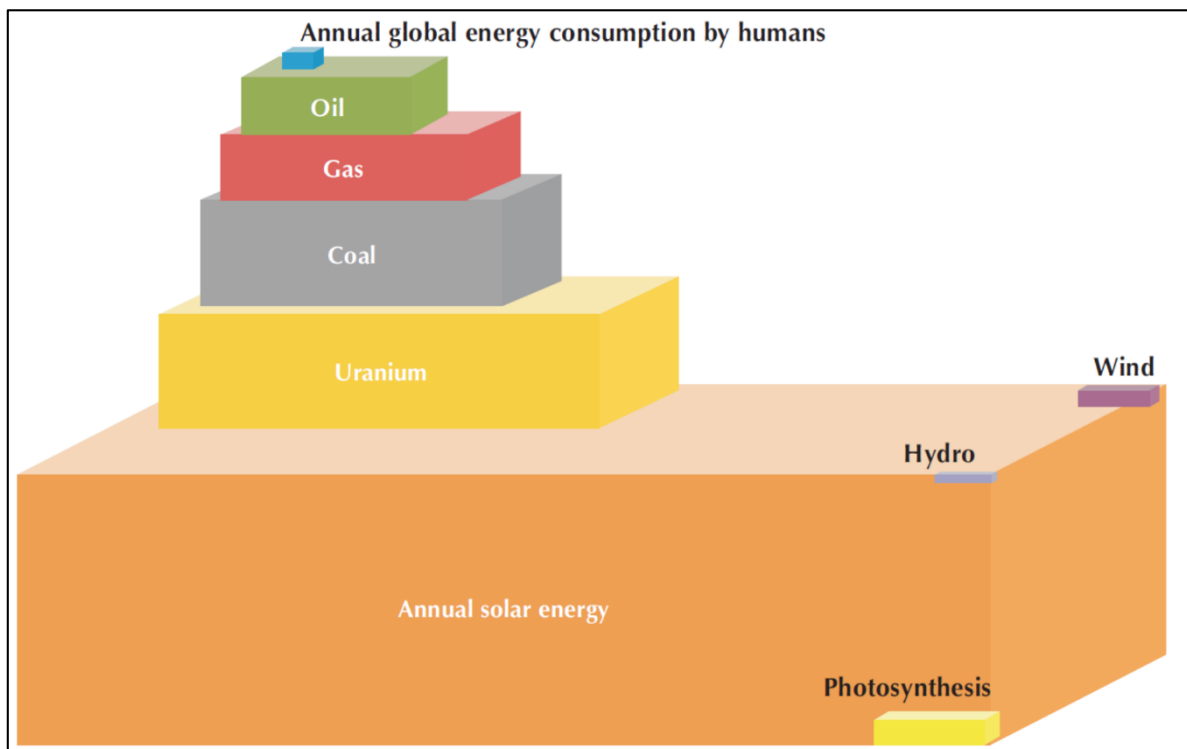
Figure 1-2. Total energy resources (National Petroleum Council, 2007)

1.1.2. Properties of th Sun Light

1.1.2.1. Properties of Light

The energy of photon (E) is function of wavelength (λ) of light.

$$E = \frac{hc}{\lambda} \qquad \text{where}$$

$$h = 6.626 \times 10^{-34}\,J \cdot s \qquad \text{Planck's constant}$$

$$c = 2.998 \times 10^{8}\,m/s \qquad \text{Speed of light}$$

$$hc = 1.99 \times 10^{-25}\,J \cdot m$$

Electron-volt (eV) is easy way to express the energy of quantum particle such as photons or electrons rather than joule (J). $1eV$ is the energy of an electron with 1 volt. In terms of $eV\ and\ n$m, the energy of photon is expressed by

$$1\,eV = 1.602 \times 10^{-19}\,J$$

$$hc = (1.99 \times 10^{-25}\,J \cdot m) \times \left(\frac{1eV}{1.602 \times 10^{-19}\,J}\right) = 1.24 \times 10^{-6}\,eV \cdot m$$

$$E(eV) = \frac{hc}{\lambda} = \frac{1240}{\lambda(nm)}$$

The photon flux ($\emptyset$) is defined how many photons arrived per second per unit area

$$\emptyset = \frac{\# \ of \ photons}{sec \cdot m^2}$$

The photon flux does not contain information of the energy of photons. The multiply of the photon energy and flux is the power density (P) for monochromic light.

$$P\left(\frac{W}{m^2}\right) = \emptyset \times \frac{hc}{\lambda}$$

The spectral irradiance (F) as a function of wavelength is used for characterizing a light. It is the power density at certain wavelength (Wm^{-2}nm^{-1}).

$$F(\lambda) = \frac{P}{\Delta\lambda}$$

The total power density generated from the solar radiation is integrating the spectral irradiance over all wavelengths.

$$P\left(\frac{W}{m^2}\right) = \int_0^\infty F(\lambda)d\lambda$$

1.1.2.2. Solar irradiance on the Earth
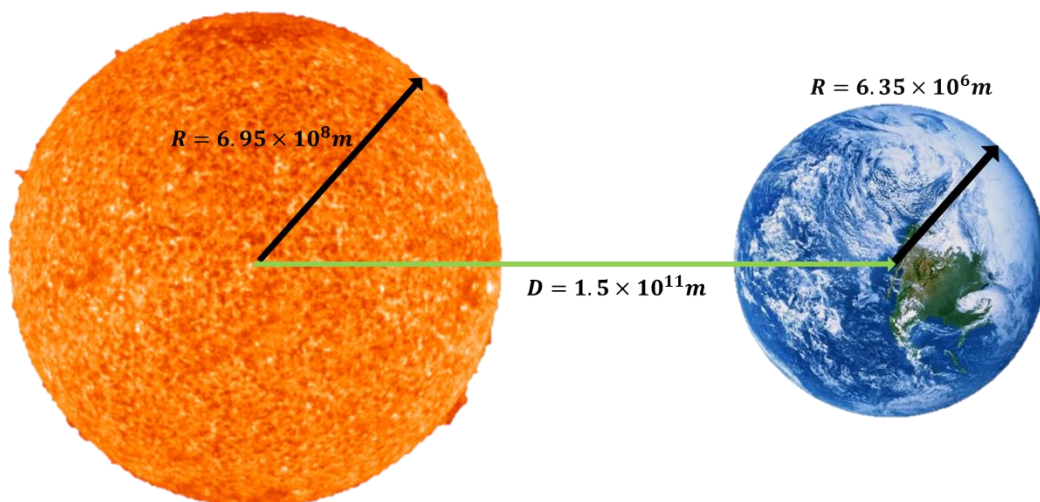
Figure 1-3. Geometric constant of the earth and the sun

Only small portion of the total power of the sun arriving on the earth which is distant from the sun. The solar irradiance (P_0) is the power density of the sunlight on the surface of the earth. The solar

irradiance at the earth from the sun with distance (D) is calculated by division of the total power of the sun by the sphere surface area ($4\pi D^2$) of the radius D. The power density of surface of sun (P_{sun}) is similar with a blackbody at 6000K (~60 MW/m^2) and the total power is multiplying the sun's surface area ($4\pi R^2_{sun}$). Therefore, the solar irradiance on the earth can be calculate by

$$P_0 = \frac{R^2_{sun}}{D^2} \times P_{sun}$$

as a result, the solar irradiance of out of the atmosphere of the earth is about 1366 W/m^2.

1.1.2.3. Air Mass

Atmosphere of the earth influence on the solar radiation at surface of the earth. The solar radiation is reduced due to absorption, scattering and reflection in the atmosphere with the spectral components of the solar radiation is changed. And it is divided into two components as direct radiation and diffuse radiation caused by atmosphere. So the Air Mass (AM) is important for solar cell application in considering the atmospheric effect. The AM is the optical path length in the atmosphere compare to the shortest path length. The AM is defined as

$$AM = \frac{1}{\cos\theta}$$

It is AM1 when the sun locate directly overhead. Above outer of the Earth where no atmosphere considered as AM0.
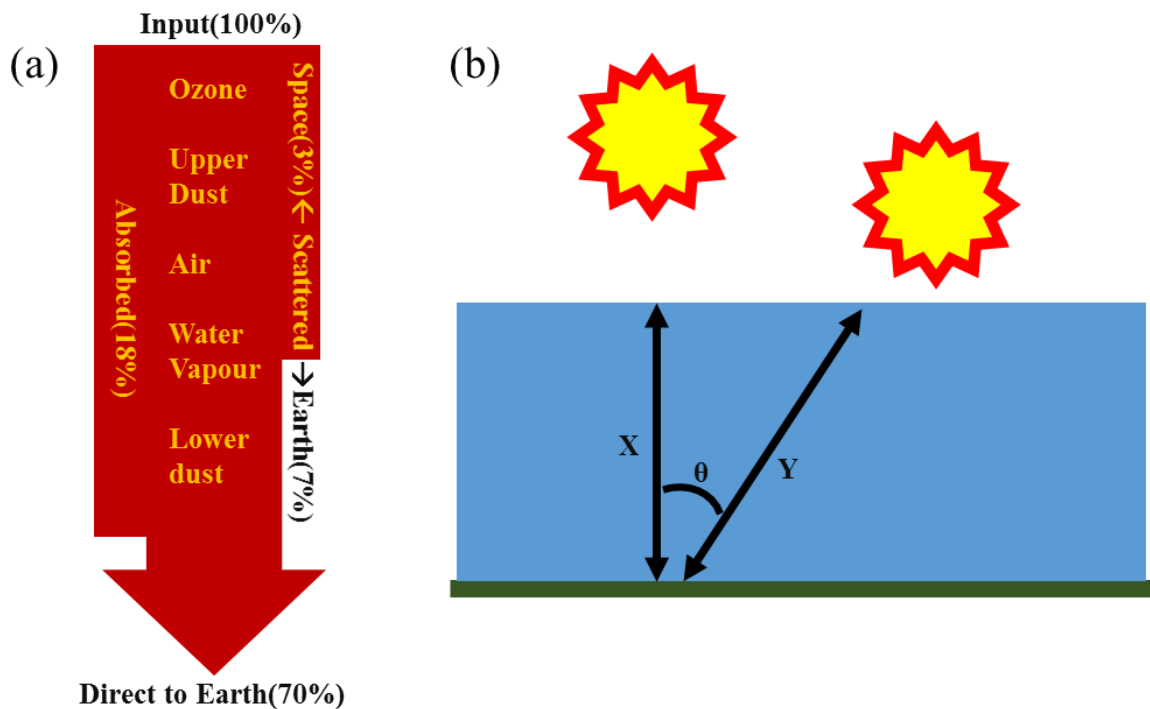
Figure 1-4. (A) Absorption and scattering by atmosphere (B) The AM is $X/Y = 1/\cos\theta$

The performance of solar cells is sensitive to both of power and spectrum of the light. Standard spectrum and power density must be defined for accurate mesurement. The standard spectrum at the surface of the earth is AM1.5G (global) including both of direct and diffuse radiation or AM1.5D including just direct radiation. The global irradiation is 10% higher than the direct one. It is about 970 W/m^2 for AM1.5G. For simplicity, the standard AM1.5G is normalized as 1000 W/m^2.
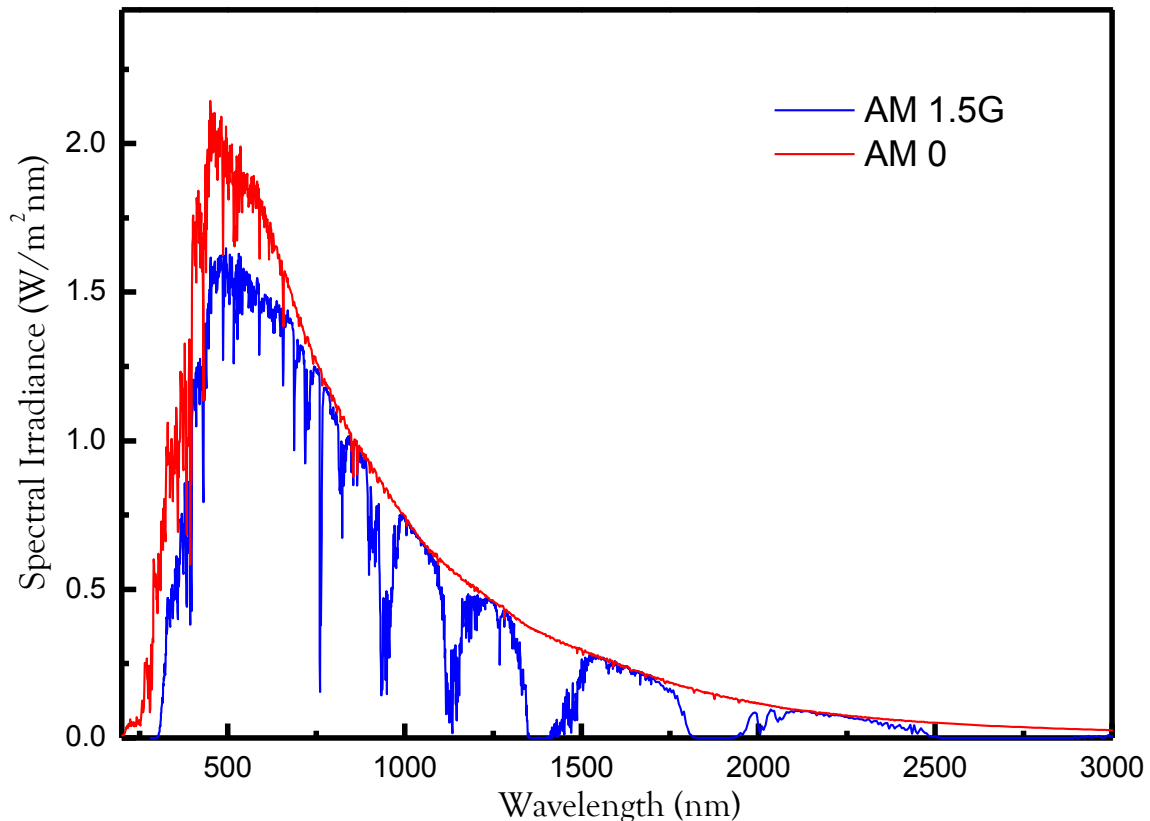
Figure 1-5. Standard Solar Spectra for space and terrestrsolarial use

1.2. Solar Cells

1.2.1. Introduction

A solar cell (called a photovoltaic cell) is the device able to directly converts light into electricity. Photon achive on the solar cell generates both of current and voltage to produce electric power. This device requires the material able to absorb photons to excite an electrons to a high level energy state and the structure that make movement excited electron from the material into an external circuit. Various materials and structure satisfy the ask for photovoltaic energy conversion. The basic mechanisms of the solar cell are

1st. the generation of light-induced carriers.

2nd. the collection of the light-induced carries as current.

3rd. the production of electrical potential across the device.

The solar cell technology has been researched for many years but its application in daily life began only in the last decade with impressive growth rates. The first practical solar cell was developed at Bell laboratory in 1954 with 6% efficiency. In this day, Single *p–n* junction crystalline silicon devices approach the theoretical limitation.[3]
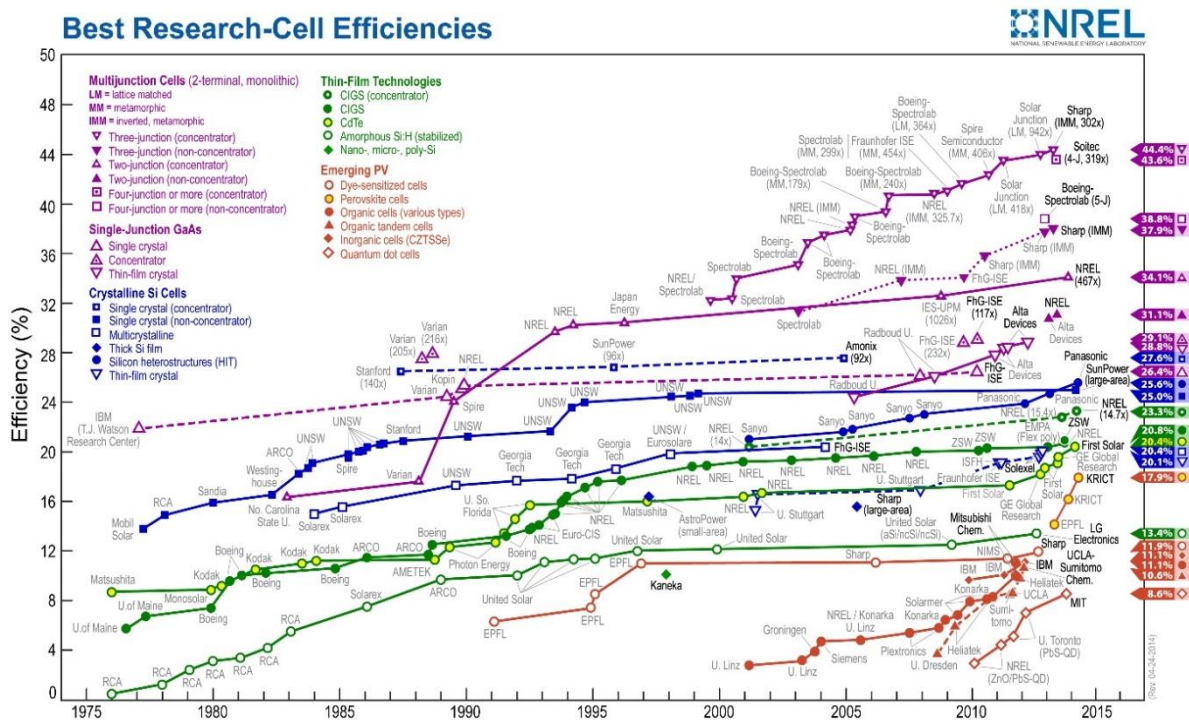
Figure 1-6. Best Research-Cell Efficiencies Table

Single solar cells are assembled into modules and it is linked together to generate power of hundreds MW.

1.2.2. Theory

1.2.2.1. Absorption of Light

Photons crash to the surface of the semiconductor for solar cells are reflected at the top surface or absorbed in the cells. If it is failed either of two processes, photon is transmitted through the semiconductor. Reflection and transmission are negative path for solar cells. Absorbed photon able to excite electrons from valence band to conduction band if the energy of the photon is larger than energy band gap of the semiconductor. The absorption coefficient (*α*) represent light absorption ability of a material.

$$I = I_0 e^{-\alpha x}$$

where α is the absorption coefficient with cm^{-1} unit, x is path length, and I_0, I is the light intensity befor and after passing the material, respectively.
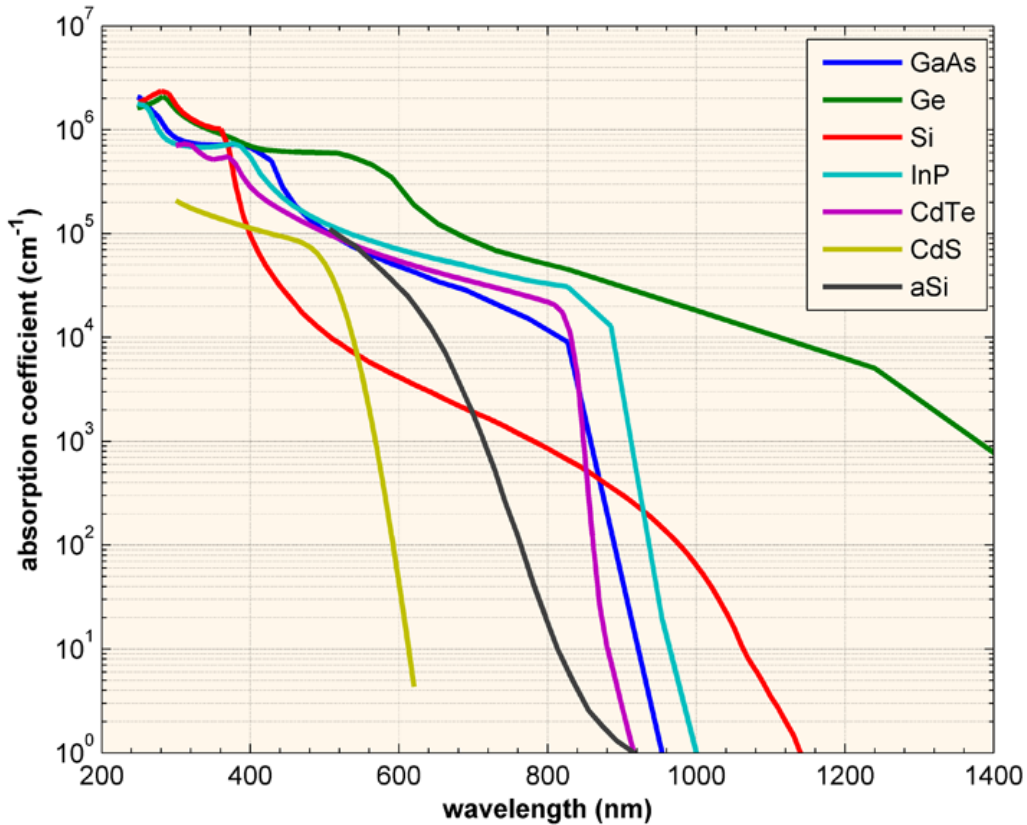
Figure 1-7. The absorption coefficient (α) in various semiconductor materials at 300K.[4-5]

The amount of absorbed light in a material depends on absorption coefficient and thickness. The material has low absorption coefficient is transparent since light is transmitted at that wavelength. The absorption coefficient is function of the material and wavelength of light. Semiconductor have a sharp edge in absorption coefficient because just light which has enough energy larger than the band gap can excite an electron. Blue light with short wavelength has a large absorption coefficient. So it can be absorbed in thin layer. However the red light with long wavelength is absorbed less. So enough thickness of absorber layer is needed for absorption.

1.2.2.2. The photovoltaic effect

The generation rate (G) is the number of electrons generated per second per unit volume. The absorption of photons causes the generation of an excess carriers in the semiconductor. Generation rate (G) is fuction of absortpion coefficient and light flux.

$$G = \alpha \emptyset_0 e^{-\alpha x}$$

This equations show that the generation is highest at the surface and exponentially decreases throughout the semiconductor. The current caused by light-generated electrons are not able to itself give power generation. Voltage should be generated as well as current for generating power. This phenomenon called photovoltaic effect. *p-n* junction of semiconductors is simple and well studied photovoltaic cell. *p-n* junctions are formed by metallic connection of *n*-type has a high electron concentration (majority carrier) and a low hole concentration (minority carrier) and *p*-type has vice versa. Electrons diffuse from *n*-type to *p*-type and holes diffuse vice versa. Then electric field (ε) forms between positive ions in the *n*-type and negative ions in the *p*-type. The absorption of photons produce both a majority and a minority carrier. The concentration of light-generated carriers is orders of magnitude higher than minority carriers and less than majority carriers. So majority carriers does not considered in *p-n* junctions with illumination and minority carrier is important for working of solar cells with *p-n* junctions. This need higher purity of semiconductor for solar cell application that increase the price of the materials. Light-generated carriers is accumulated via electrons on the *n*-type by drift and holes on the *p*-type by drift when external net current is zero. This mechanism cause the voltage between *n*-type and *p*-type semiconductor.
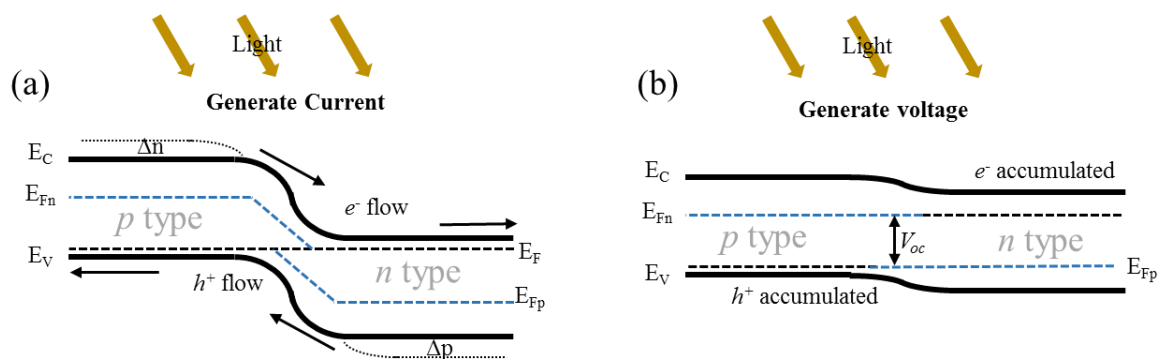
Figure 1-8. (a) The scheme of current generation by illumination (b) of voltage

1.2.2.3. IV Curve

The IV curve of a photovoltaic cell is displacement of the IV curve of diode (in the dark) with the

light-generated current (I_L).[6]
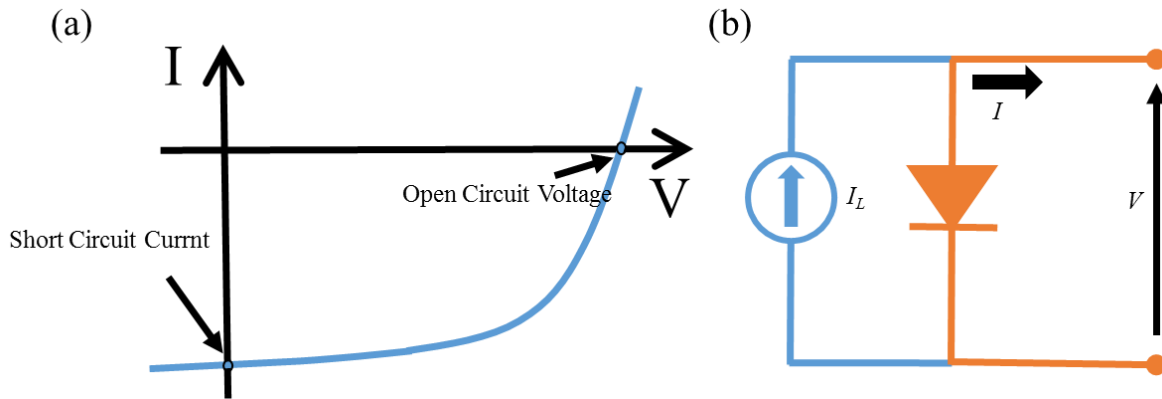
Figure 1-9. (a) The effect of illumination on IV curve of diode (b) Equivalent circit for solar cell

So the equation of solar cell is exactly the same of diode equation except for light generated current (I_L).

$$I = I_0 e^{qV/nkT} - I_L$$

The short circuit current (I_{sc}) is the current when solar cell is at short circuit condition with output voltage of the solar cell is zero. Neglect the loss path way, the I_{sc} and I_L are the same. So the I_{sc} is the largest current generated from solar cell. The short circuit current density (J_{sc}, mA/cm^2) is more useful for laboratory scale.
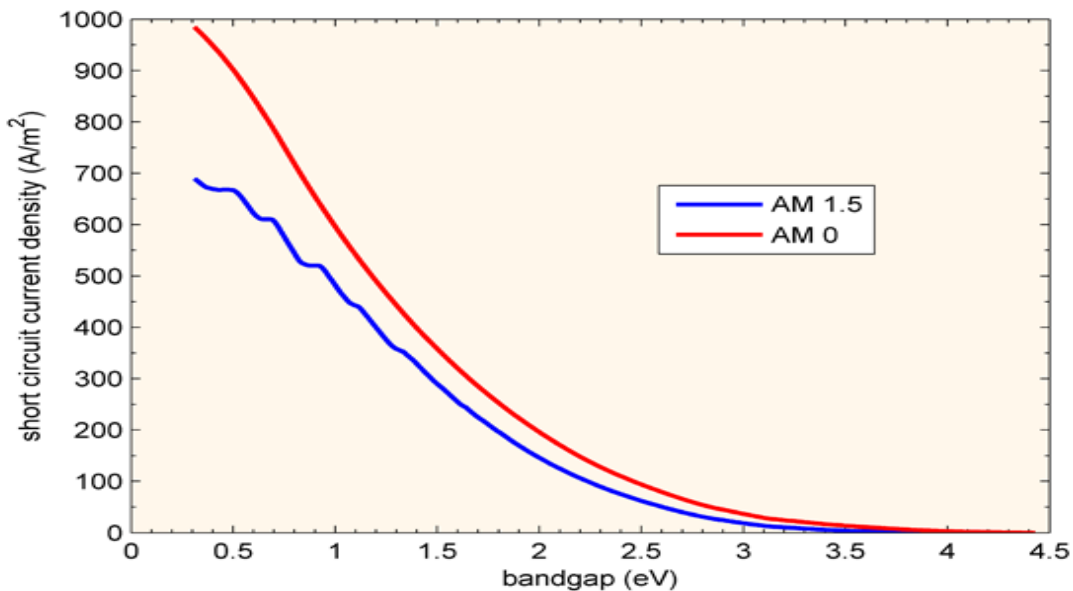
Figure 1-10. A single photon above the band gap generate one carrier in ideal solar cell. So lower band gap material shows higher short circuit current.

The open-circuit voltage (V_{oc}) is the maximum voltage when solar cell can generat at open circuit

condition with zero current. So V_{oc} can expressed by

$$V_{oc} = \frac{nkT}{q} \ln \frac{I_L}{I_0}$$

The open-circuit voltage is the same of forward bias applyed on the solar cell for preventing flow of light generated current. V_{oc} depends on the saturation current (I_0) and the light generated current of the solar cell. V_{oc} is varied by recombination because the saturation current is sensitive to recombination in the solar cell. So mesuring the V_{oc} is one of the method for investigation of the amount of recombination in the device. The V_{oc} is also determined by the carrier concentration.[7]

$$V_{oc} = \frac{kT}{q} \ln \left[\frac{p \cdot \Delta n}{n_i^2} \right]_{p\ type} = \frac{kT}{q} \ln \left[\frac{n \cdot \Delta p}{n_i^2} \right]_{n\ type}$$

where Δn, Δp are the excess minority carrier concentration and n_i is the intrinsic carrier concentration. V_{oc} increases with the band gap increases on the contrary to the I_{sc}.

The fill factor (FF) is important parameter for determination of the maximum power from a solar cell. V_{oc} and I_{sc} are the maximum voltage and current respectively from a solar cell. However, at these points, the output power is zero. The FF is defined as the ratio of the maximum power of the solar cell to the product of V_{oc} and I_{sc}.

$$FF = \frac{A}{B} = \frac{V_{max}I_{max}}{V_{oc}I_{sc}}$$
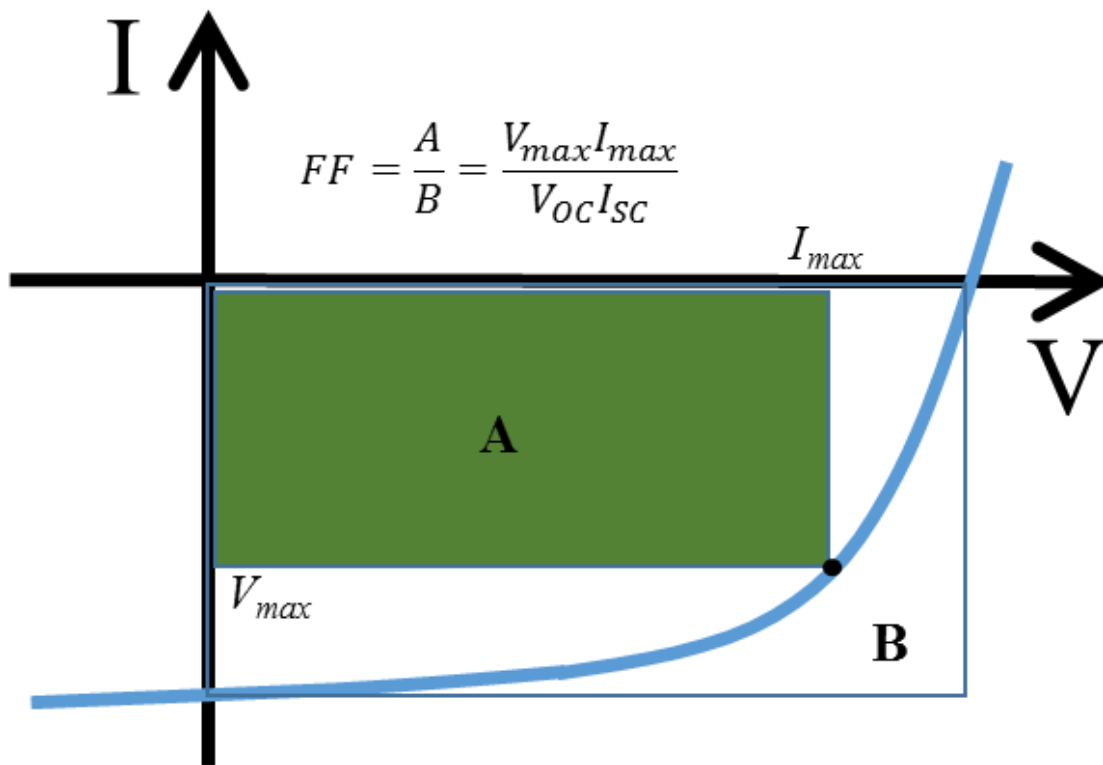
Figure 1-11. The FF is ratio of the maximum power of the solar cell to the product of V_{oc} and I_{sc}

1.2.2.4. Efficiency

The efficiency (η) represent the performance of solar cell. Efficiency is the ratio of maxium output power of the solar cell to input power from the sunlight.

$$\eta = \frac{P_{max}}{P_{in}} = \frac{V_{oc}I_{sc}FF}{P_{in}}$$

The efficiency depends on the componenets of spectrum, intensity of the sunlight, and the temperature of the solar cell. Therefore, The measurment conditions should be carefully controlled for measuring efficiency. The solar cells measured at AM1.5 conditions with a temperature of $25\,^{\circ}C$.

1.2.2.5. Quantum Efficiency

The quantum efficiency (QE) is the ratio of number of collected electrons to the number of photons from incident sunlight. The QE is function of wavelength. If all photons can generate the current, the

quantum efficiency is 1. While QE is ideally square shape, the QE of solar cells is reduced due to several reason. Near UV photons with high energy is absorbed very close to the surface. So high front surface recombination will affect the this region of the QE. Photons at middel range of the QE has a low diffusion length that reduce generated current. Photons with energy about bandgap are low absorption coefficiency and low diffusion length. The external QE of the solar cell covers the effect of optical losses as transmission and reflection. Internal QE does not consider about reflection of transmittion. The external QE can be revised to the internal QE by considering the reflection and transmission of the solar cell.
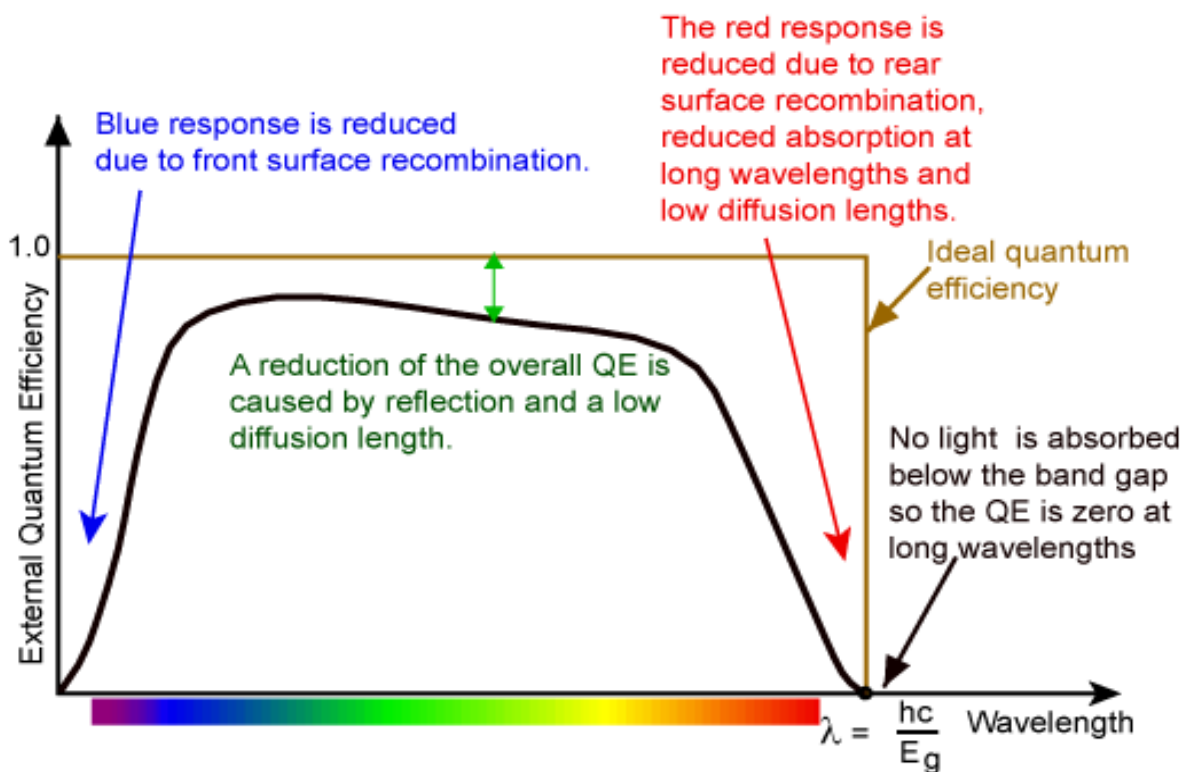
Figure 1-12. The typical quantum efficiency with degradation factors.

1.2.2.6. Resistance

The characteristic resistance (R_{ch}) is outview of resistance when the solar cell operates at maximum power point. If external load is the same of R_{ch}, then solar cell works with maximum power.

$$R_{CH} = \frac{V_{max}}{I_{max}}$$
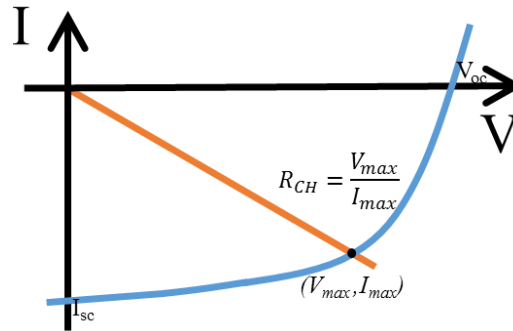
Figure 1-13. The characteristic resistance (R_{ch}) is inverse of slope at maxium point.

Parasitic resistive in the solar cell reduce the efficiency by consuming power in that resistances. Series resistance (R_s) and shunt resistance (R_{sh}) are typical parasitic resistances of the solar cell.
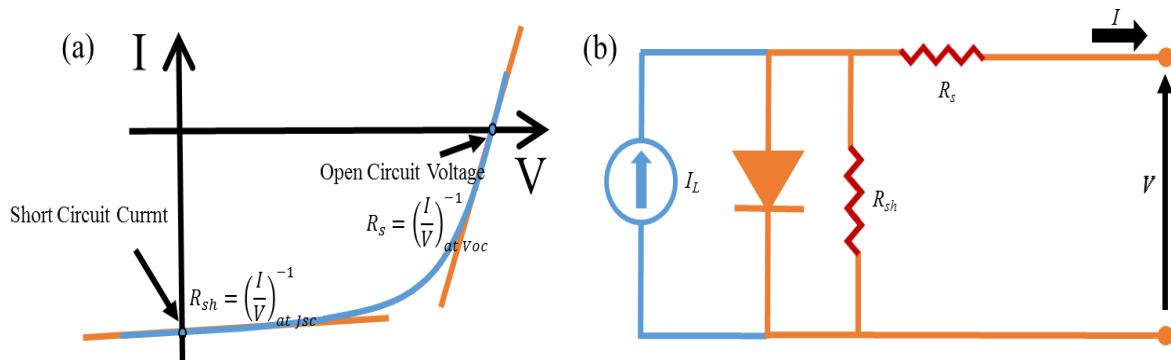
Figure 1-14. Series and shunt resistances in IV curve (a) and equivalent circuit (b) of the solar cell

Parasitic resistance as R_s and R_{sh} is important parameter to cause reducing the fill factor. Since resistance depend on the area of the solar cell, common unit of resistance that multiply resistance by area (Ωcm^2) is useful term to compare the resistance of solar cells with different areas. This normalized resistance is the inverse slope of JV curve.

$$R(\Omega \cdot cm^2) = \left(\frac{J}{V}\right)^{-1}$$

Mainly two factors have a effect on the R_s in a solar cell. the internal resistance of solar cells which disturb movement of carriers. The contact resistace between the electrode and semiconductor material. The R_s is key loss factor of the solar cells via reducing the fill factor, although high enough values of R_s reduce the I_{sc}.value. Diode equation at illumination with R_s is

$$I = I_0 e^{q(V+IR_s)/nkT} - I_L$$

The R_s does not affect on V_{oc} of the solar since total current is zero at V_{oc} point, so IR drop is not involved in V_{oc} condition.

$$V_{oc} = \frac{nkT}{q} \ln \frac{I_L}{I_0} \cancel{-IR_s}$$

However, the IV curve is strongly affected by the R_s near the V_{oc} point. So a easy way of measurement of R_s is characterizing of slope of the IV curve at V_{oc} point. The maximum power with R_s (P'_{max}) is power without R_s in solar cell minus the loss of the power at R_s. Reduced FF is simply expained with reduced power caused by R_s.

$$P'_{max} = V_{max}I_{max} - I^2_{max}R_s = P_{max}\left(1 - \frac{I_{sc}}{V_{oc}}R_s\right)$$
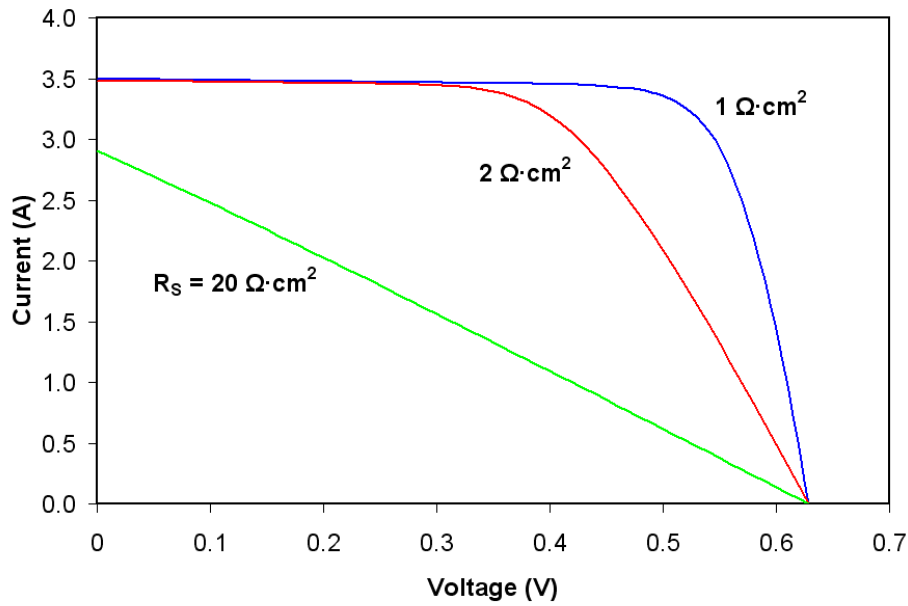
Figure 1-15. Series resistance effect on IV curve of the solar cell

The solar cell with low R_{sh} providing byway of the light generated current show significant degradation due to reducing FF. Such a byway diversion reduces the ouput current and voltage of the solar cell. R_{sh} is effect on significantly degradation of the solar cell at low light intensity. Diode equation at illumination with R_{sh} is

$$I - \frac{V}{R_{sh}} = I_0 e^{qV/nkT} - I_L$$

By measurement of slope of the IV curve at I_{sc} point, R_{sh} can be obtained.
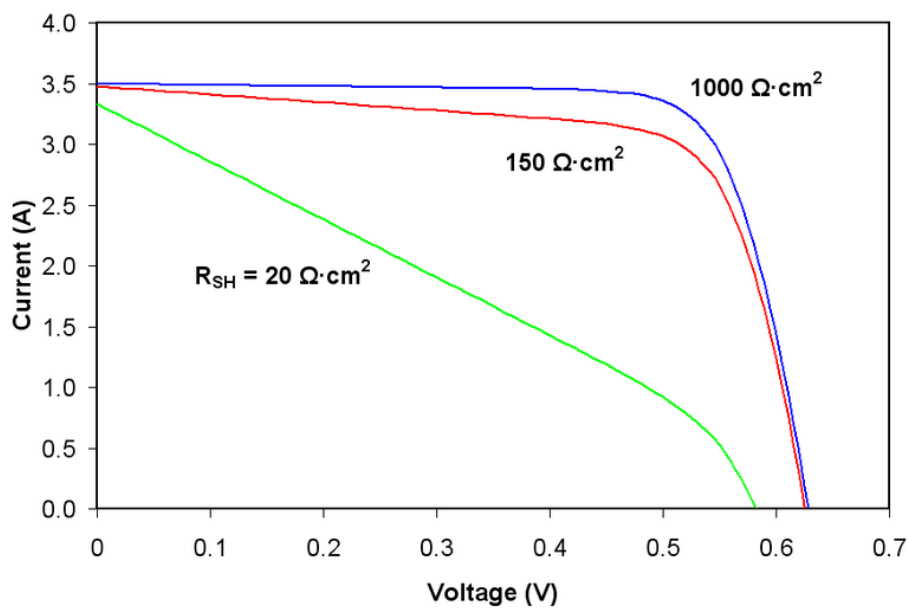
Figure 1-16. Shunt resistance effect on IV curve of the solar cell

The effect of R_{sh} on FF can be calculated by maximum power without R_s in solar cell minus the loss of the power at R_{sh}.

$$P'_{max} = V_{max}I_{max} - \frac{V_{max}^2}{R_{sh}} = P_{max}\left(1 - \frac{V_{oc}}{I_{sc}}\frac{1}{R_{sh}}\right)$$

The diode eqation of the solar cell with both of R_s and R_{sh} is

$$I - \frac{V + IR_s}{R_{sh}} = I_0 e^{q(V + IR_s)/nkT} - I_L$$

Chapter 2. Dye Sensitized Solar Cells

2.1 Photoelectrochemical method to harness the solar energy

Semiconductor has unique properties in electrochemistry as elecrode. The electrolyte solution has redox potential defined by nature and composition. If semiconductor electrode was immersed in electrolyte, charge carriers move to each others for equilibrium. So a space charge region is built up and the Fermi levels of the semiconductors are chaged leading to band bending. In the case of semiconductor electrode palys role as photoanode under illumination, band bending with electrical field drives excited electrons into the semiconductor and holes in the valance band are tranfered to the reductant in the electrolyte. Injected electrons from electrolyte are moved to external circuit and reached to the counter electron where reduction is occurred. In the case of open circuit condition under illumination, a negative potential is induced in the photoanode and the Fermi level shift up to negative direction with reducing the band bending. If intensity is increased, the Fermi level of photoanode shifts up till the band bending dissipate as called flat band condtion. At flat band condition, the photoandode shows maximum photovoltage in the system.
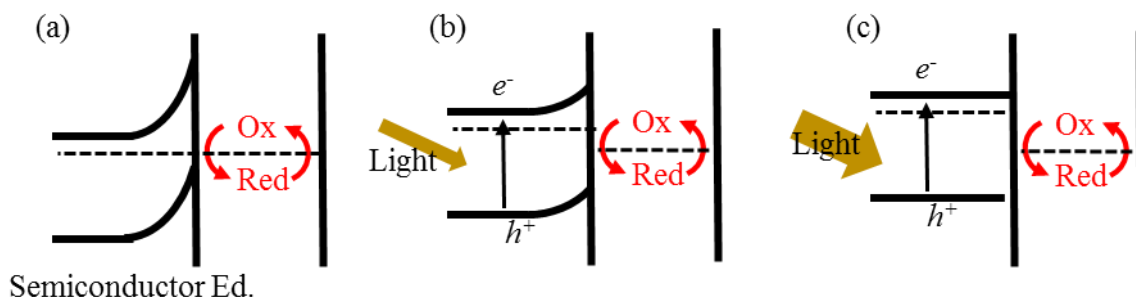
Figure 2-1. Energy band schemes when semiconductor immersed in electrolyte (a) immersed, (b) under illumination and (c) under strong illuminaiotion

In the counter electrode at current flow condition, it is occurred that regeneration of the redox mediator oxidized by holes injected from semoconductor electrode. The redox mediator is recycled, so photoelectrochemical cell is referred to as regenerative solar cell.[8-11] Oxide semiconductor asTiO_2, ZnO, SnO is mainly used for photoelectrode that generate low current with high energy bandgap. The materials with small energy bandgap as Si, Ge, CdS were introduced for photoelectrode but the electrode oxidezed itself easily. To abtain high current flow and prevent the collosion, light absorbing molecule as dye was applied oxide semiconductor electrode and it show outstanding progress.[12]

2.2. Introduction of Dye sensitized solar cells

Photosensitizer was introduced to semiconductor electrode to capture the sun light efficiently. At the

first time, bulk semiconductor was used for photoelectode with sensitizer. This work of dye sensitization of bulk semiconductor electrodes laid the foundation for the development of dye sensitized solar cells.[13-21] Dyesensitized solar cell (DSC) is basically a thin layer solar cell formed by sandwich structure of two transparent conducting oxide (TCO) electrode. The colored working electrode has a few micron thick mesoporous TiO_2 layer adsorbed with dye as photosensitizers. The counter electrode is composed of Pt deposited onto another TCO. The inter layer space is filled with an electrolyte containing a redox mediator, usually a mixture of iodine and iodide in a low viscosity organic solvent such as acetonitrile. Best solar conversion efficiency obtained for this type of DSC is in the rage of 11~12% for laboratory scale cells (<1 cm^2). Figure 2-2. shows typical DSC performance with on the Ru-bpy sensitizer as N719 measured under AM 1.5 sunlight illumination. The active area is 0.212 cm^2. In DSC of lab scale, typical J_{sc} is aroud 15-20 mA/cm^2, V_{oc} is in the range of 650-750 mV, with FF of 0.65-0.80.
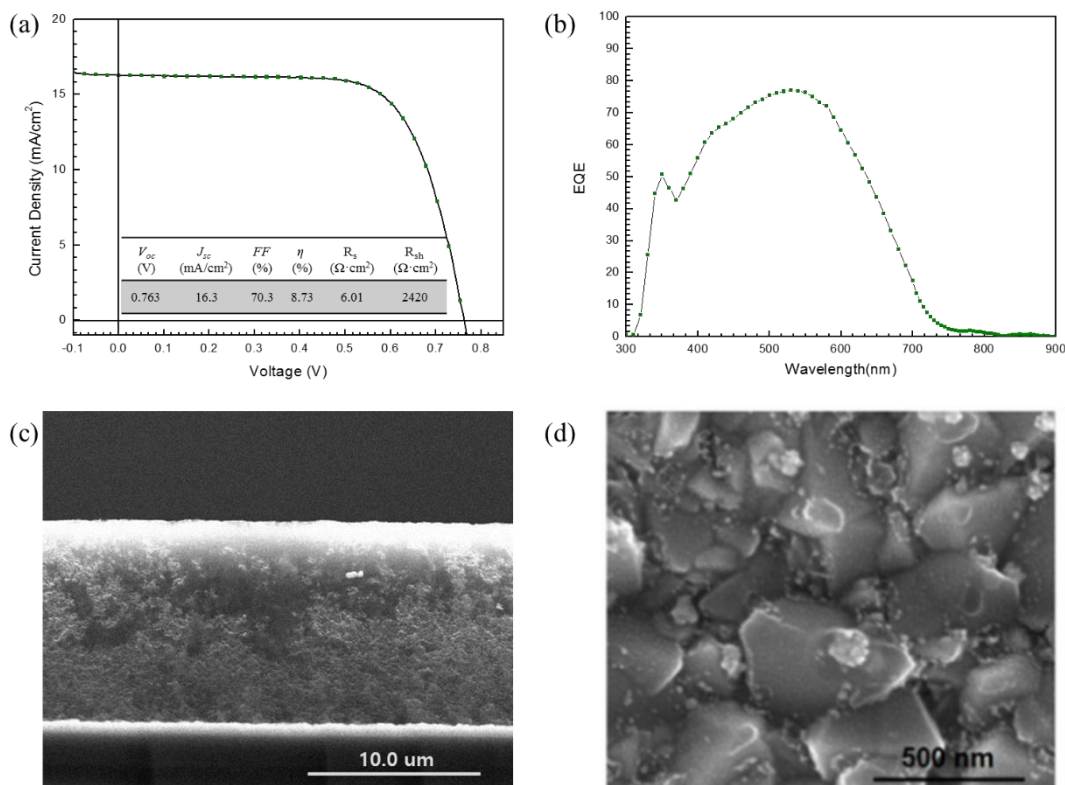
Figure 2-2. JV curve (a) and IPCE (b) of DSC. SEM image of woriking photoelectrode (c) and Pt coated counter electrode (d)

2.2.1. Electron transfer steps of DSC

To understanding of electron transfer in DSC is important to develop the performance of DSC. Absorbed photons to dye molecules (*D*) lead the formation of excited state of the dye (*D*[*])

$$D + h\nu \rightarrow D^*$$
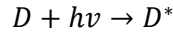
Excited dye molecule can decay back to the ground state of the dye with emission or be oxidized by injecting electrons into the conduction band of TiO$_2$

$$D^* \rightarrow D + h\nu \ (emission)$$

$$D^* \rightarrow D^+ + e^- \ (TiO_2 \ CB)$$
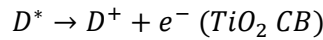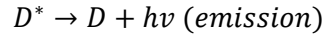
The injected electrons at the conduction band of TiO$_2$ transport through the mesoporous nanostructure to reach the charge collector as TCO and pass through the external circuit to work. Energy consumed electron is reached to counter electrode. The oxidized dye is reduced rapidly to the ground state by the reducing agent (I$^-$) present in the electrolyte.

$$2D^+ + 3I^- \rightarrow 2D + I_3^-$$
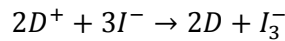
There are probability of recombination as injected electrons to TiO$_2$ from dye molecules by regeneration of excited dye or reduction of oxidizing agent (I_3^-) in electrolyte or intrinsic recombination in TiO$_2$ itself.

$$D^+ + e^-(TiO_2 \ CB) \rightarrow D (recombination)$$

$$I_3^- + 2e^-(TiO_2 \ CB) \rightarrow 3I^- (recombination)$$

$$e^- + h^+ \rightarrow h\nu \ (emission)$$
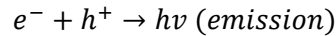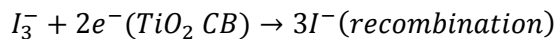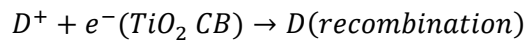
Electrons reaching the counter electrode through the external circuit reduce the oxidized triiodidie (I_3^-). So entire sequence of electron transfer reaction involving the dye and the redox mediator is done.

$$I_3^- + 2e^- \rightarrow 3I^-$$

(1) Direct phtoexcitation
(2) Intrinsic recombination
(3) Electron trapping/detrapping
(4) Interfacial injection
(5) Interfacial recombination
(6) Intermolecular photoexcitaion
(7) Intermolecular recombination
(8) Regeneration
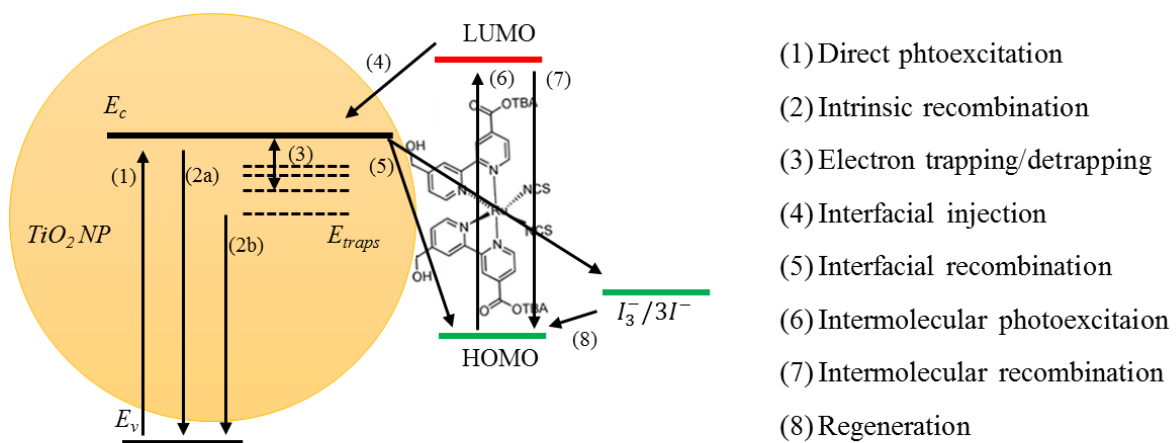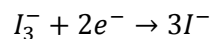
Figure 2-3. Electron transfer at interfacial of TiO$_2$//Dye//Electrolyte.

Kinetic of electron transfer is DSC is important to understand remarkable performance of DSC. It is

reported that timescale in intermolecular recombination in dye molecules is about 60ns and electron injection from the excited dye into the TiO_2 is about 50fs ~ 1.7 ps. Recombination of the electrons in the TiO_2 conduction band with oxidized dye is around few ms scale and with a iodide in the electrolyte is 10 ms scale. The regeneration of the oxidized dye by iodide is 10 ns scale.[22]

2.2.2. Substrates

The DSC has a sandwich structure involving two TCO substrates. The requirements for the TCO substrate are low sheet resistance even after annealing process at 450~500℃ for formation of TiO2 nanostructure and a high transparency in the visible-IR region. Typical sheet resistance of the TCO used is 5-15 Ω/cm^2. The cost of TCOs rises steeply with lower sheet resistance and better light transmittance. The cost of these two substrates for the electrodes account for nearly half of the total cost of the solar cell. Both indium doped tin oxide (ITO) and fluorine doped tin oxide (FTO) have been employed. Sandwich type structure with glasses have an adventage of good protection against penetration of oxygen or water. ITO is the most common substrate used in many photonic and optoelectronic devices. This is possible to manufacture in mass production on the industrial scale. Unfortunately, thermal stability of the ITO is not good for formation of TiO_2 nanostructure. Hence preferred TCO for DSC is FTO. Only two companies (Pilkington and Asahi) produce FTO coated glass with high proce. Since the resistance of the TCO is too high, additional current collectors like silver fingers have to be applied in module scales and lager. Flexible substrate is possible as ITO coated polyethyleneterephalate (ITO-PET) and polyethylenenaphthalate (ITO-PEN). The disadvantages of plastic substrates is limited temperature processing, higher sheet resistance (60 Ω/cm^2 for ITO-PET) and permeability of water and oxygen. Metal foils are possible to apply to DSC as titanium or stainless steel.[23-24]
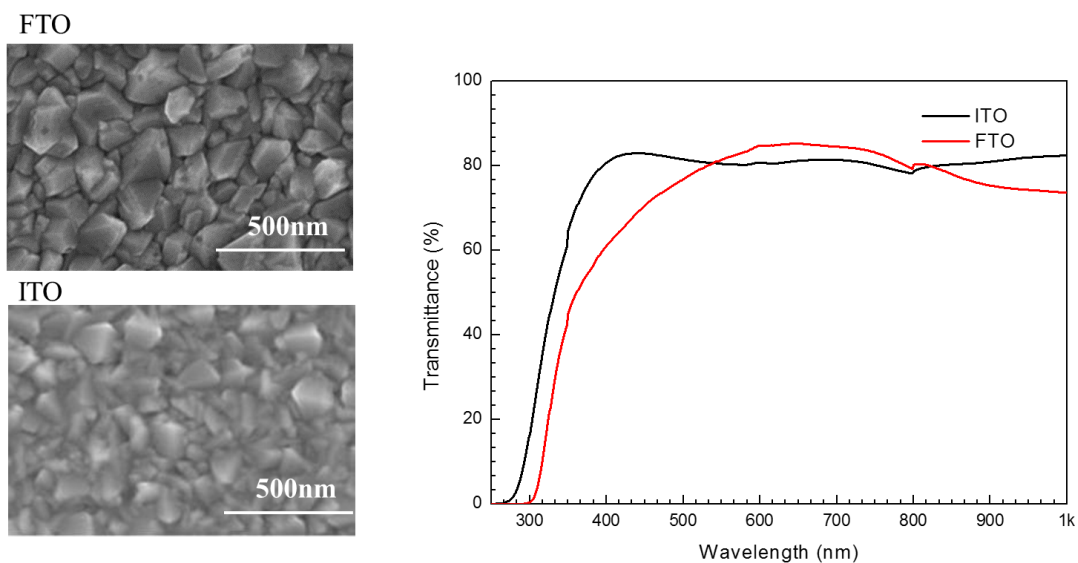
Figure 2-5. SEM image and Transmittance of the TCOs

2.2.3. Photoanode

Various oxide semiconductors with varied nanostructure have been introduced to photoanode of DSC for DSCs.[25-36] Especially, TiO_2 is chemically stable, nontoxic and readily available in vast quantities. Thousands of publications have appeared on the preparation of colloidal particles of titania by the sol-gel hydrolysis route using different precursors. An important requirement for the photoanode of DSC is high transport mobility of the charge carrier to reduce the electron-transport resistance. TiO_2 has many crystalline formsas anatase, rutile and brookite. (Figure 2-6.)
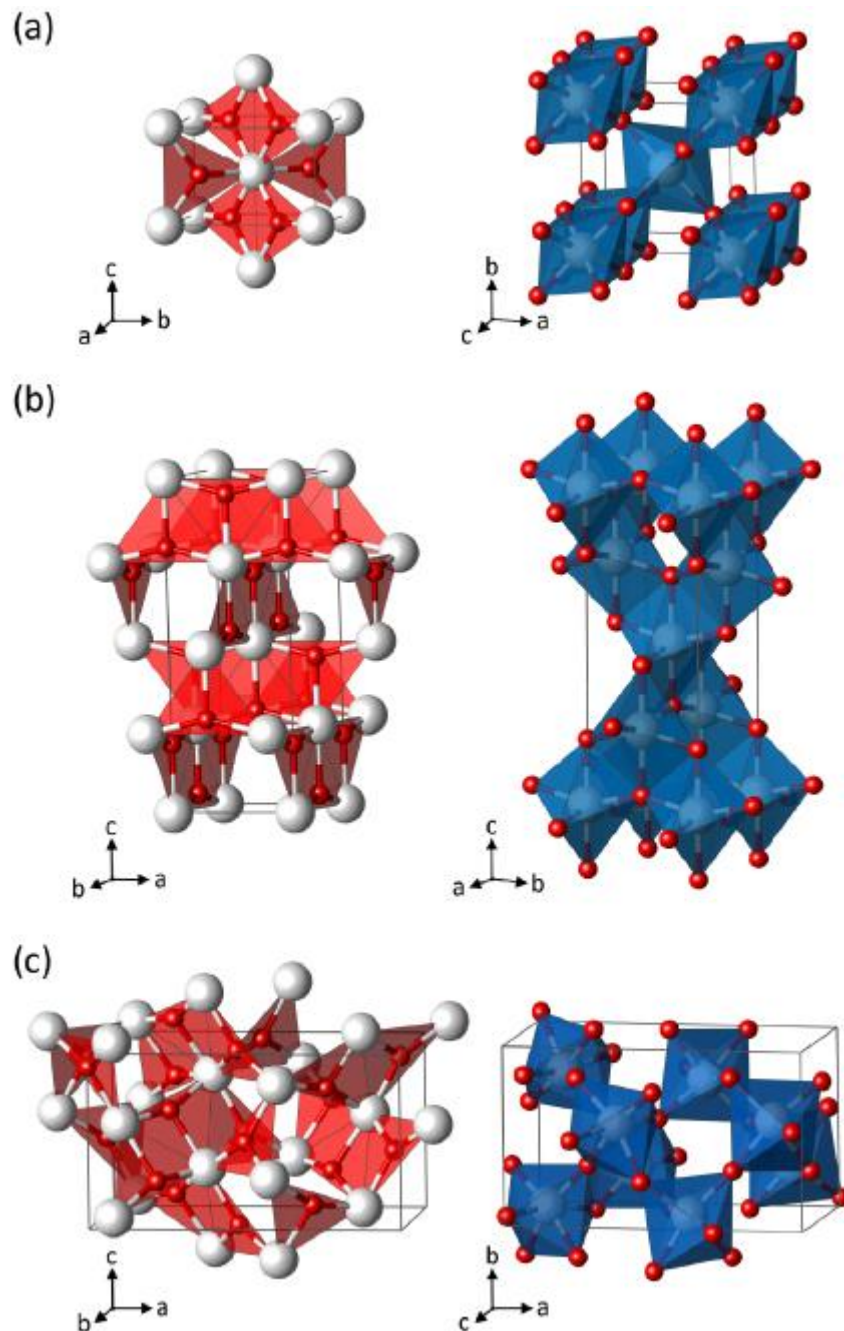
Figure 2-6. TiO$_2$ phases as rutile (a), anatase (b) and brookite (c)[37]

DSC with anatase form TiO$_2$ show better performance than rutile one. It is caused by lower photocurrent of the rutile film as result of lesser amount of adsorbed dye due to smaller surface area. per unit volume compared with that of the anatase film. Furthermore, electron transport throught the rutile film is slower than through the anatase film due to poor interconnection between nanoparticles.[38]

In earlier studies of DSC with single crystal TiO$_2$, the efficiency was quite low less than 1 % due to two important factors. One is the excited-state injection process is efficient only at the monolayer coverage level, the other is poor absorption efficiency (cross section) for visible light by a monolayer

of the dye. An important breakthrough, leading to an enhancement in the conversion efficiency, came about when the available surface area for dye loading was increased considerably in the mesoporous oxide form of thin films.
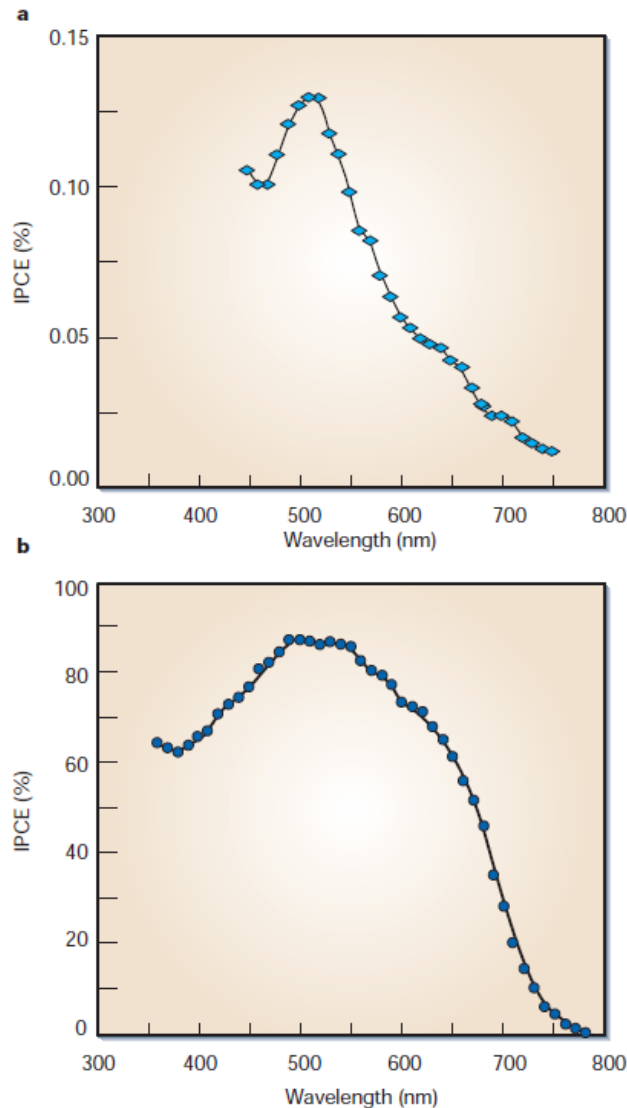
Figure 2-7. IPCE of DSC with (a) single crystal anatase cut in the (101) plane and (b) nanocrystalline anatase nanoparticles.[39]

Figure 2-7. shows difference by comparing the IPCE of the DSC with single crystal anatase cut in the (101) plane and nanocrystalline anatase nanoparticles. The IPCE increased significantly from 10 to 90 % due to more efficient light absorption by large amount of dyes covered the larger area within the mesoporous structure. The photons with low energy show much more efficient in nanocrystalline anatase nanoparticles. It is unique property of the mesoporous film of the nanocrystalline layers. Figure 2-8. shows nanocrystalline anatase nanoparicle with various size via hydrothermal synthesis.
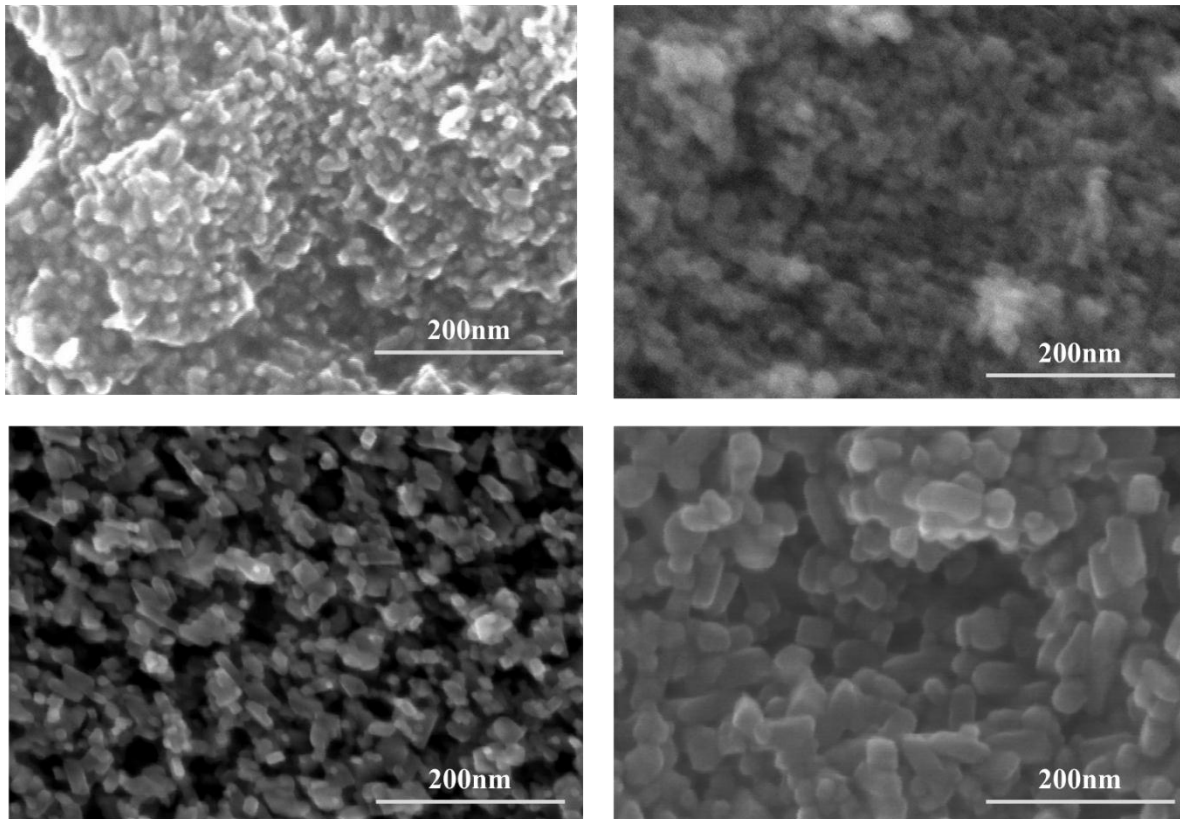
Figure 2-8. Synthsized TiO_2 nanoparticle with average particle size of (a) 15nm, (b) 20 nm, (c) 25 nm, (d) 40 nm.

2.2.4. Dyes

Dye as photosensitizer is key component of the DSC. Dye absorbs the solar radiation and injects electrons into the conduction band of the TiO_2. Organic molecules, coordination complexes of transition metals with polypyridine or porphine ligands have been designed for DSC.[40-48] Desirable properties for dye with high performance are 1. strong light absorption in the visible and near- IR region for efficient light harvesting. 2. good solubility in organic solvents for facile deposition from stock solutions. 3. presence of suitable anchoring ligands such as -COOH to promote the effective interaction of the dye with TIO_2 surface and thus the coupling energy levels. 4. suitable disposition of the HOMO and LUMO of the dye molecule to permit quantitative injection of charges from the excited state. Figure 2-9 shows

typical dyes with Ru as center of molecules.
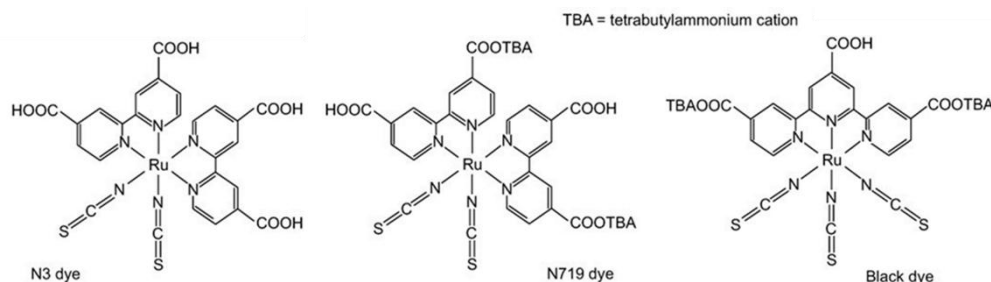
Figure 2-9. Ru dyes of polypyridine family

2.2.5. Electrolytes

The electrolyte plays a very important role in the DSC by facilitating the transport of charge between the working and counter electrodes. The ideal electrolyte solvent is one that has very low viscosity, negligible vapor pressure, high boiling point and high dielectric properties. For industrial view point, factors such as chemical inertness, environmental sustainability, and easy processing are also important. Among the many redox mediators examined, the iodide/triiodide couple has been found to be the best. Under optimized conditions, the iodide has a concentration with range of 10~50 mM and iodine ten times greater in organic solvent as acetonitrile. LiI had been used as the iodide source in earlier studies, but now the ionic liquid such as imidazolium iodide is used. Since the I^-/I_3^- mixture also absorbs in the visible-light region, their concentrations have to be kept as low as possible. The low-viscosity solvent ACN permits the use of low iodide concentrations. Acetonitrile is a proper organic solvent for electrolytes for DSC with high dielectric constant to dissolve many ionic salts and additives. However, it has a low boiling point and cyanide functional group which is hydrolyzed in the long term with presence of small amount of water. These degradation limit usage in DSC. In practical field, DSC should endure outdoor environments such as high humidity and temperature. There are many approaches to jump up these problems. Ionic liquids and electrolytes with nanoparticles or organic polymers have been proposed.[49-54] The eutectic melts is on of the solution for the problem.[55]

2.2.6. Counter Electrode

To regenerate the oxidized form of electolyte component, catalytic counter electrode is necessary to be reduced by the electrons flowing through the external circuit passing through the counter electrode. To reduce losses, the counter-electrode material should show good electrocatalytic properties as Pt. Pt shows excellent chemical stability and very low overpotential for the tri-iodide reduction reaction. For application of DSC, nanosize Pt clusters was prepared by the thermal decomposition of precusor on FTO substrate to maximize the catalytic effect for reduction of iodine or triiodide. Pt counter electrodes

was prepared by electrodeposition, too.[56-57] Electrodeposited Pt counter electrodes are potentially applicable for flexible solar cells for adventage of low temperature process.

Carbon as alternative of Pt in counter electrode was studied.[58] This work has been subsequently adopted for carbon black.[59-60] Since then, there have been a number of studies on the use of different forms of carbon as the counter electrode material for the DSC as graphite, pyrolytic carbon, carbon black, and single and multi walled carbon nanotubes (CNT).

2.3. Characterization of DSC with Electrocheimcal Impedance Spectroscopy.

2.3.1. Basic

Electrochemical Impedance Spectroscopy (EIS) is important tool for investigating the properties and quality of DSC. This method measure the impedance ($Z(\omega)$) of the devices by mesureing the ac current ($\tilde{I}(\omega)$) at a certain angular frequency (ω) when a certain ac voltage ($\tilde{V}(\omega)$) is applied to the device or vice versa. The impedance define as

$$Z(\omega) = |Z| \angle \theta = Z' + iZ'' = \frac{\tilde{V}(\omega)}{\tilde{I}(\omega)}$$

$$\tilde{V}(\omega) = V_0 e^{i\omega t}, \qquad \tilde{I}(\omega) = I_0 e^{i(\omega+\varphi)t}$$

During an impedance measurement, the system is kept in steady state condition with tiny alternating perturbation in frequency range from mHz to 10 MHz with 5-10 measurements per decade. At low frequencies, it takes a long time for mesurement enough to make the system unstable. Nevertheless, measurements at low frequencies are often important. Impedance data is related elements of equivalent circuit give the information of physical properties of the system. Many measurements of EIS can be described by equivalent circuits composed of combinations of a few elements indicated in Table 2.1. Equivalent circuits are formed by connecting these and other elements by wires, representing low resistance paths in the system. Table 2.2 shows the complex elements consist of real part and imaginaty part.

Domination	Symbol	Scheme	Impedance(Z)
Resistance	R		R
Capacitance	C		$\dfrac{1}{i\omega C}$
Inductor	L		$i\omega L$
CPE(Constant Phase Element)	Q_n		$\dfrac{Q}{(i\omega)^n}$

Table 2-1. Basic ac electrical elements

Domination	Definition	Real and Imaginary parts
Impedance	$Z(\omega)$	$Z = Z'+Z''$
Admittance	$Y(\omega)=\dfrac{1}{z(\omega)}$	$Y = Y'+iY''$
Complex capacitance	$C^*(\omega)=\dfrac{1}{i\omega Z(\omega)}$	$C^* = C'+iC''$ $=-\dfrac{Z''}{\omega(Z'^2+Z''^2)} - i\,\dfrac{Z'}{\omega(Z'^2+Z''^2)}$

Table 2-2. Impedance representations

The impedance and Complex capacitance of series contact of R-C is

$$Z(\omega) = R_1 + \frac{1}{i\omega C_1}$$

$$C^* = \frac{C_1}{1 + i\omega\tau}$$

the relaxation time is defined as

$$\tau = R_1 C_1$$

The complex impedance plot is shown in Figure 2-10. Real part shows resistance and imaginary part shows capacitance form a vertical line. Since the impedance of a capacitor is ∞ at low frequency as dc

34

voltage, the dc current is prevented at low frequncy. However, the impedance of the capacitor decreases as the frequency increases, the capacitor indeed becomes a short-circuit at enough high frequncy. Consequently, there remains only the resistance R_1.
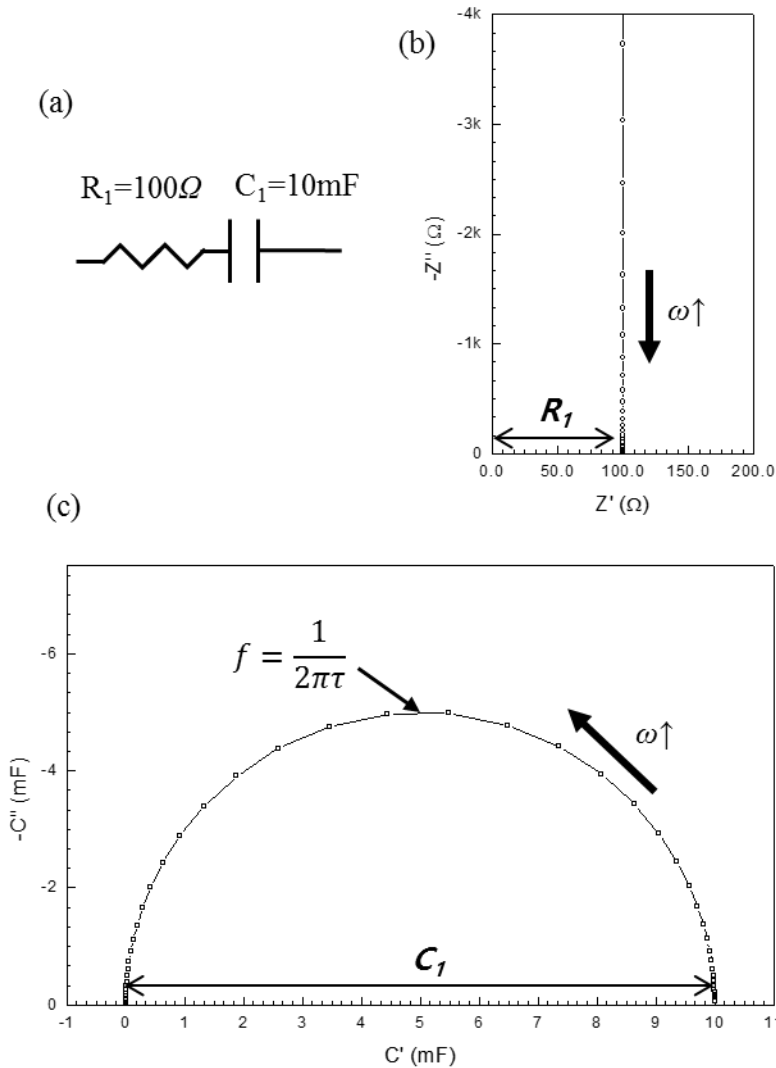
Figure 2-10. Equivalent circuit (a) and impedance (b), capacitance (c) response. $R_1 = 100 \, \Omega$, $C_1 = 10$ mF, $\tau = 1$ s. The thick arrows indicate the direction of an increasing angular frequency (ω).

The plot of the complex capacitance is shown in Figure 2-10.(c). The capacitance displays an arc from the dc value $C^*(0) = C_1$ to the high frequency value $C^*(\infty) = 0$. The top of the arc occurs at the characteristic frequency of the relaxation τ.

The parallel $R_2//C_2$ forms an arc in the complex plane which is shifted positively along the real axis by the series resistance, R_1. Figure 2-11. (c) shows the transition of the resistance from the low frequency ($R_{dc} = R_1 + R_2$) to the high frequency value (R_2). This high frequency value occurs due to the capacitor

impedance disappears at very high frequency. In EIS, capacitances play important role, since different elements with similar resistance show very distinct spectral features if their capacitances differ sufficiently. Therfore, the capacitance is a key to the understanding of the origin of the measured resistances.
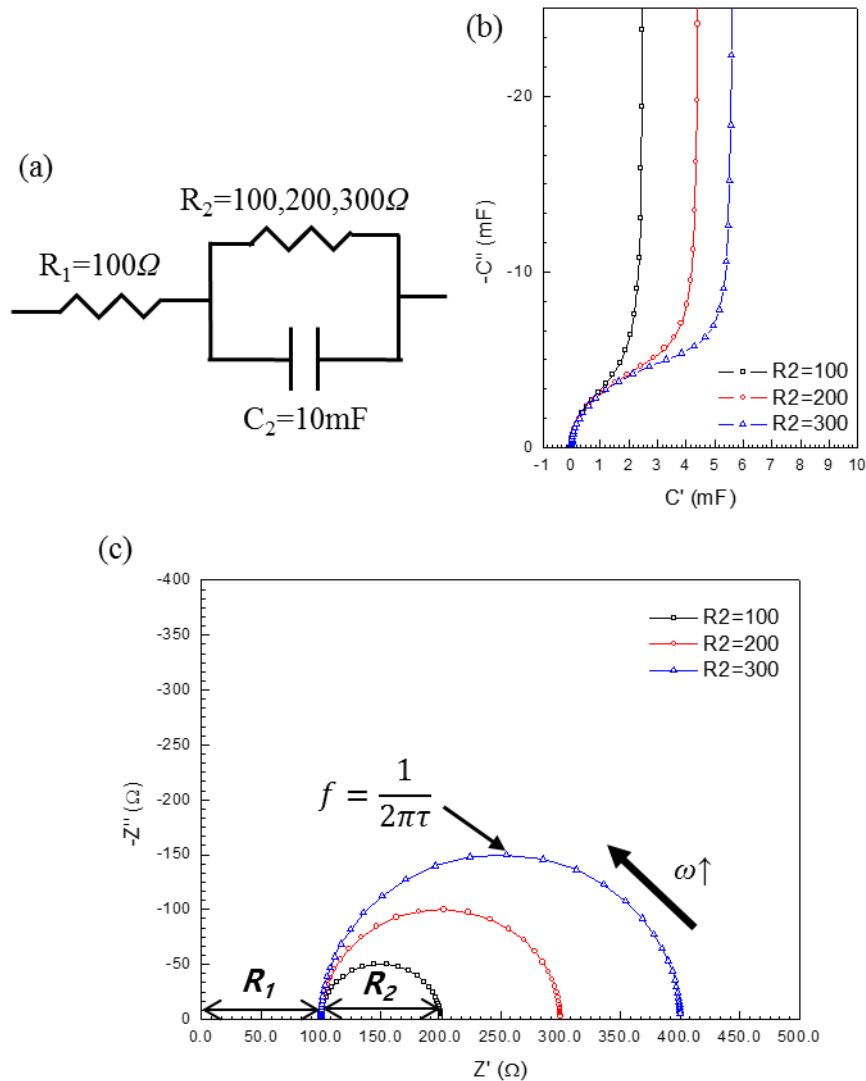
Figure 2-11. Equivalent circuit (a) and capacitance (b), impedance (c) response of Randle circuit.

2.3.2. Physical models for DSC

For obtaining physical information from EIS data, it is necessary that proper equivalent circuit of the system. DSC is little different with p-n juntion solid solar cells. Figure 2-1. Shows simple DSC model considered as ELH layer consist of electron transport layer (E) with injected carriers density (Δn), light absorber (L) with thickness L, and hole trandport layer (H).
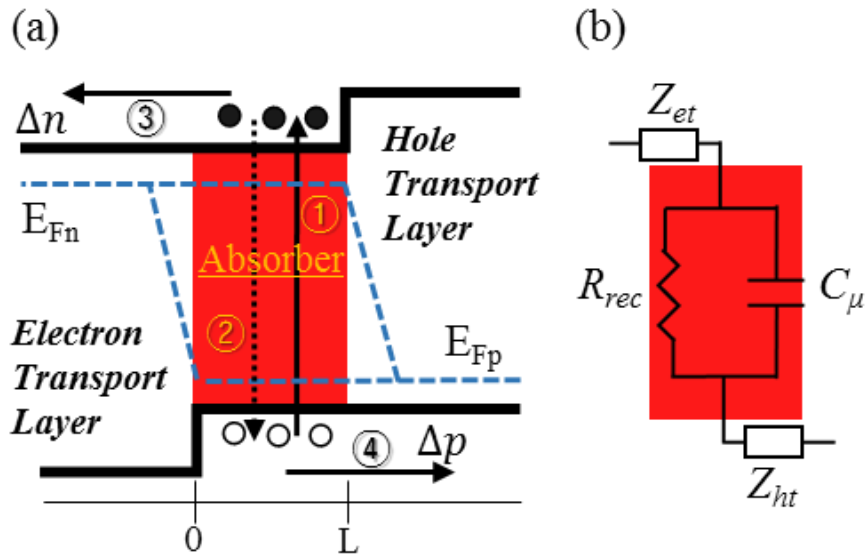
Figure 2-12. Simple DSC model as EAH layer and eqivalent circuit

This model shows diode chracteristic as *p-n* juntion

$$I = I_0 \left[e^{-\frac{qV}{nkT}} - 1 \right] - I_L$$

There are four majot pathways of carrier transport

1. Electron excitation via absorption of photon. Chemical capacitance (C_μ) represent this pathway produces a votage by split Fermi level in equivalent circuit.

2. Recombination corresponding to the diode at *p-n* junction.

3. Electron injection and transport.

4. Hole injuction and transport.

The conservation equation of electron is

$$\frac{dn}{dt} = \frac{d\Delta n}{dt} = \frac{1}{q}\left(\frac{\partial J_n}{\partial x}\right) + G - U_n$$

where G is the rate of optical photogeneration per unit volume due to the illumination. U_n is the rate of recombination of electrons per unit volume as function of carrier density and elextron life time (τ_0).

$$U_n = \frac{n}{\tau_0}$$

The diffusion current of electron (J_n) is flux of carriers with diffusion coefficient (D_n) and gradient of concentration.

$$J_n = q \frac{\partial n}{\partial x}$$

For simplicity, It is assumed that photogeneration of carriers is homogeneous (thin absorber alyer) and D_n value is large enough to maintain the flux of carriers flowing with very small gradient of concentration. Then flux of diffusion current of conservation equation become independent of position.

$$\frac{\partial J_n}{\partial x} = \frac{J_n(L) - J_n(0)}{L}$$

and the right contact blocks the electrons

$$J_n(L) = 0$$

Therefore, the output current through electron transport layer is

$$J_n = qL \left[G - U_n - \frac{d\Delta n}{dt} \right]$$

In order to calculate the EIS data, we should consider all physical quantities A are composed of a stationary part ($\bar{A}$) and a small perturbation part ($\tilde{A}$).

$$E_{Fn}(t) = \overline{E_{Fn}} + \widetilde{E_{Fn}}(t) = \overline{E_{Fn}} + q\tilde{V}$$

$$n(t) = n(E_{Fn}) = \bar{n} + \tilde{n}(t) = \bar{n} + q\frac{\partial n}{\partial E_{Fn}}\tilde{V}$$
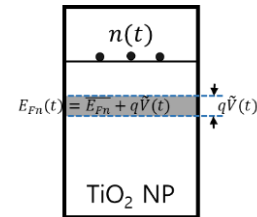
Microscopic chemical capacitance (c_μ, F/cm^3) is defined as number of particle change per deviation of chemical potential (μ) in single TiO$_2$ particle.
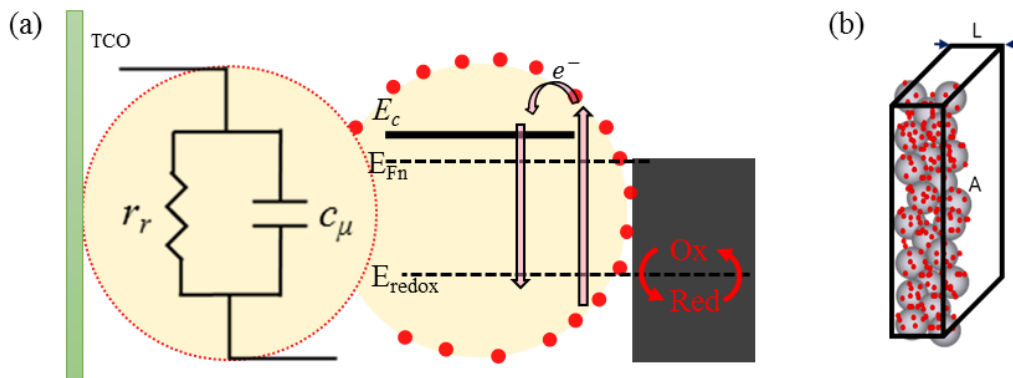
Figure 2-13. Basic equiavalent circuit for single TiO$_2$ nanoparticle in DSC (a), Scheme for calculating macroscopic parameters (b)

$$c_\mu = \frac{Charge}{Potential} = \frac{q\partial N_{e^-}}{\frac{1}{q}\partial \mu_{e^-}} = q^2\frac{\partial n}{\partial E_{Fn}} = \frac{q^2}{kT}N_c e^{-(E_c - E_{Fn})/kT} = \frac{q^2}{kT}n$$

Macroscopic chemical capacitance (C_μ, F) is function of film thickness (L), area (A), and porosity(p).

$$C_\mu = LA(1-p)\, c_\mu$$

So relationship between small perturbation of carrier density and voltage is

$$\tilde{n}(t) = q \frac{\partial n}{\partial E_{Fn}} \tilde{V} = \frac{1}{q} c_\mu \tilde{V}$$

The recombination rate U_n is

$$U_n(t) = \overline{U_n} + \widetilde{U_n} = \overline{U_n} + \left(\frac{\partial U_n}{\partial n}\right)\tilde{n} = \overline{U_n} + \left(\frac{\partial U_n}{\partial n}\right)\frac{c_\mu}{q}\tilde{V} = \overline{U_n} + \frac{1}{qr_r}\tilde{V}$$

where microscopic recombination resistance per unit volume ($\Omega\cdot$cm^3) is

$$r_r = \frac{1}{c_\mu}\left(\frac{\partial U_n}{\partial n}\right)^{-1} = \left(q^2\frac{\partial n}{\partial E_{Fn}}\right)^{-1}\left(\frac{\partial U_n}{\partial n}\right)^{-1} = \left(q^2\frac{\partial U_n}{\partial E_{Fn}}\right)^{-1}, r_r c_\mu = \tau_0 = \left(\frac{\partial U_n}{\partial n}\right)^{-1}$$

Macroscopic recombination resistance is

$$R_r = \frac{1}{LA(1-p)}r_r$$

The conservation equation can be described as

$$J_n = \overline{J_n} + \widetilde{J_n} = qL\left(\overline{G} - \left(\overline{U_n} + \widetilde{U_n}\right) - \frac{d\tilde{n}}{dt}\right)$$

$$\widetilde{J_n} = -qL\left(\widetilde{U_n} + \frac{d\tilde{n}}{dt}\right) = -qL\left(\frac{1}{qr_r}\tilde{V} + \frac{c_\mu}{q}\frac{d\tilde{V}}{dt}\right) = -L\left(\frac{\tilde{V}}{r_r} + c_\mu\frac{d\tilde{V}}{dt}\right)$$

Then electron lifetime can be obtained by applying a perturbation and let the system decay by itself when it occurred at open circuit condition.

$$\widetilde{J_n} = 0 = \frac{\tilde{V}}{r_r} + c_\mu\frac{d\tilde{V}}{dt} \rightarrow \frac{d\tilde{V}}{dt} = -\frac{\tilde{V}}{c_\mu r_r} = -\frac{\tilde{V}}{C_\mu R_r} = -\frac{\tilde{V}}{\tau_0}$$

This equation means the exponential decay of a small step of excess carrier concentration by recombination. the time constant of the decay process is electron life time (τ_0).

At open circuit condition under illumination, the net rate of electron injection into the mesoporous TiO$_2$ nanoparticle oxide must be the same with the net rate of back reaction as electron transfer to I_3^- ions in electrolyte and the oxidized dye molecules. Back reaction to oxidized dye molecules can be neglected due to the kinetic of dye regeneration by I^- ions in electrolyte is much faster than back reaction.

$$\frac{dn}{dt} = v_{inj} - v_{br} = 0$$

Here, v_{inj} and v_{br} are volume rates for electron injection and back reaction of electron to I_3^-, respectively. Measurements of the conduction band electron density directly in a DSC are difficult. One of possible method to monitor changes in conduction band electron density is measuring the conductivity of the mesoporous oxide.[61-63] The most important indirect measurement of the electron density of conduction band is measuring the V_{oc}. In the dark condition, electrons in the TiO$_2$ nanoparticle are in equilibrium with the I^-/I_3^- redox system of electrolyte with redox potential ($E_{F,redox}$). In DSC, the conduction band of TiO2 is believed to be located approximately 1.0 eV above the redox potential.[64] The electron density of equilibrium with redox (n_r) system is

$$n_r = N_c e^{-(E_c - E_{F,redox})/kT} \approx 10^4 \text{ cm}^{-3}$$

where N_c is the effective density of state of conduction band at TiO$_2$ nanopartucle about 10^{21} cm^{-3}.[65] At illumination, The V_{oc} correspods to the change in Fermilevel in the TiO$_2$ as fuction of electron density of conduction band.

$$V_{oc} = \frac{1}{q}(E_{Fn} - E_{Fredox}) = \frac{kT}{q} \ln \frac{n_l}{n_r}$$

Electron density at conduction band at illumination can be calculated through the V_{oc} as 0.75V.

$$n_l = N_c e^{-(E_c - E_{Fn})/kT} = n_r e^{qV_{oc}/kT} \approx 10^{17} \text{ cm}^{-3}$$

2.3.3. Transmission line model

One of important equivalent circuit for DSC is transmission line (TL) model shown in Figure 2-14.
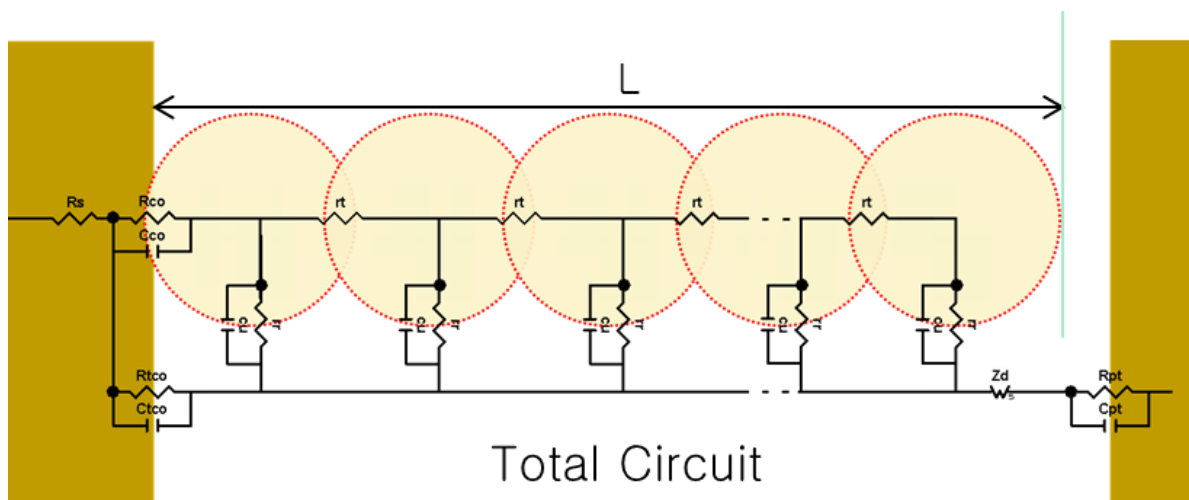
Figure 2-14. General transmission line equivalent circuit for porous electrode.

Parameters in equivalent circuit is changed with bias forward voltage. In no bias condition, electron recombination resistance is enough large to be neglected such as shown in Figure 2-15.
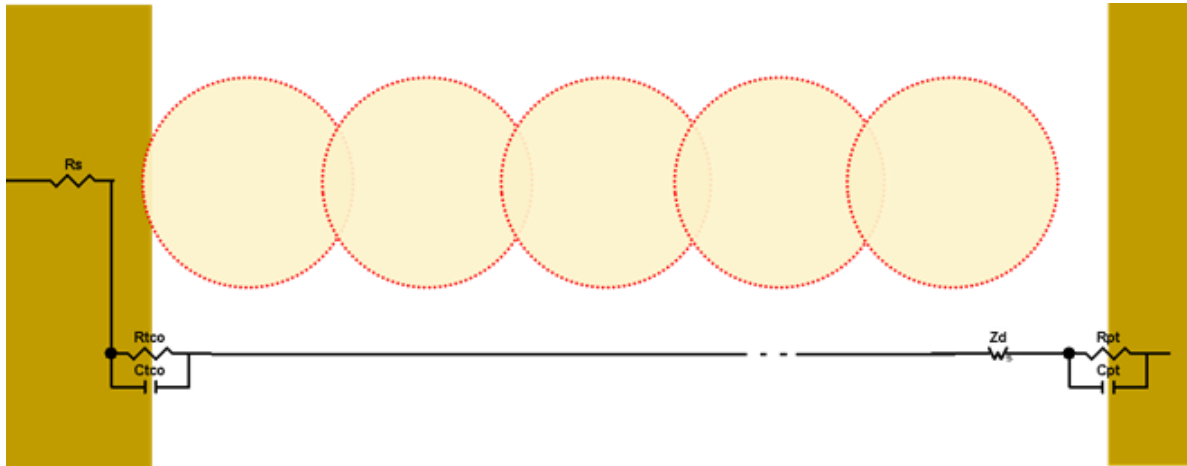
Figure 2-15. TL model in no bias condition.

If high forward bias is applied, recombination resistance is reduced caused by riching charge carriers in TiO_2. So electron transfer resistance at TCO//Electrolyte interfaces can be neglected. (Figure 2-16.)
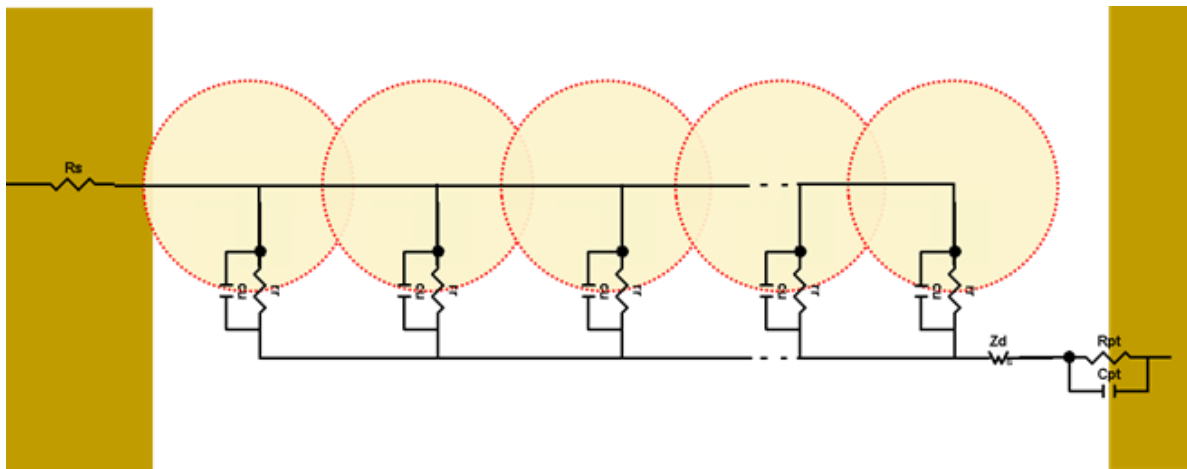
Figure 2-17. TL model with high bias potential.

In this condition, EIS measurement shows 3 semicircles. The first arc at the high frequency represents the charge transfer at the interface of the counter electrode and electrolyte. The second semicircle with middle frequency represents the charge transfer through the dye/TiO_2/electrolyte interface. The additional third semicircle is attributed diffusion of redox components in the electrolyte. (Figure 2-18.)
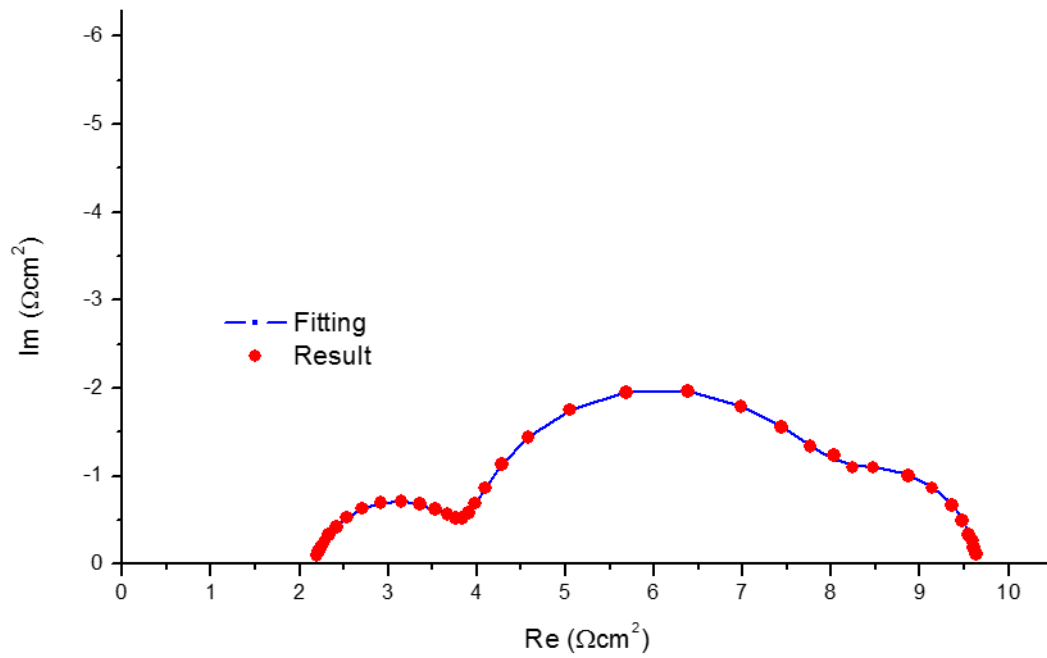
Rs $(\Omega \cdot cm^2)$	Rct-Pt $(\Omega \cdot cm^2)$	Rct-TiO$_2$ $(\Omega \cdot cm^2)$	Rd $(\Omega \cdot cm^2)$	$1/\omega_d$	$D_{I_3^-}$ (cm^2/s)
2.172	1.746	4.016	1.684	0.316	1.98×10^{-5}

$$Z_d = R_d \frac{\tanh(\iota\,\omega/\omega_d)^{1/2}}{(\iota\,\omega/\omega_d)^{1/2}} \qquad \omega_d = \frac{D_{eff}}{L_{eff}^2}$$

Figure 2-18. EIS data and fitting, 3rd semicircle shows diffusion coefficient of I_3^- in electrolyte.

Chapter 3. ZnO nanostructure for photoanode of DSC

3.1. Introduction

ZnO is a wide band-gap semiconductor that has a similar structure and physical properties to those of TiO$_2$ and thought to be a promising alternative owing to its ease of crystallization, anisotropic growth, and higher electronic mobility for better electron transport and overall low recombination losses.[66] Large internal surface area is the foremost requirement of the photoelectrode film in DSSCs to ensure that sufficient dye molecules can be adsorbed to capture the incident photons. The controlling synthetic parameter of inorganic semiconductor nanostructures in terms of size, shape, and area is strongly motivated by their size and shape dependent properties,[67] especially in the case of ZnO. In the nanometric domain, controlling the morphologies of the synthesized nanostructures is one of the most challenging issues.[68] Notably, Yang et al. have intensively studied the synthesis of various morphologies by a vapor transport process.[69] Zhu et al. prepared a tower-like structure of ZnO.[70] Wang et al. synthesized ZnO nanobelts by evaporating metal oxide powders.[71]

The conventional method of synthesizing ZnO nanoparticles with an average diameter ranging from ten to several tens of nanometers entails preparing ZnO sols in ethanolic solutions with precursors of lithium hydroxide and zinc acetate.[72-74] Further process is performed on these sols to yield films by spin-coating or dip-coating liquid sol onto a solid wet gel. The gel is thermalized so as to generate a porous structured film on the substrate. The doctor-blade method is also frequently adopted for the preparation of ZnO nanocrystalline films.[75-76] Besides nanoparticulate films, nanoporous structured ZnO films were also studied for use as photoelectrodes in DSSCs due to the high porosity of the films.[77-81] Among these methods, electrochemical deposition and chemical bath deposition show characteristics that are advantageous for forming nanoporous films with nanowalls vertically grown on the substrate. Here we study solution-based method to prepare densely packed setose ZnO nanorod arrays on ZnO nanosheet layer. We used a curved plate ZnO nanosheet (CPZ) layer to control the population and nucleation event of ZnO nanorod grouth. To synthesize the CPZ layer, colloidal solution of the precursor was prepared through hydrolysis of zinc salts in the presence of poly-ethylenimin and then coated by airbrush method on ZnO initial seed layer. ZnO nanorods have been grown on the CPZ layer with chemical bath deposition method. To compare conventional method of growing ZnO nanosheet layer, methanolic solution based ZnO nanosheet (MSZ) layer has been synthesized by methanolic solution bath deposition method and ZnO nanorod have been grown on it. A power conversion efficiency of DSSCs with photoanode of setose ZnO nanostructurer was enhanced to 3.04 %.

3.2. Experimental

3.2.1. Preparation of ZnO nanostructured photoanode.

An F-doped SnO_2 conducting glass substrate (FTO, TEC 8, 2.3 mm, Pilkington) was cleaned with detergent, D.I. water, acetone and isopropanol, and dried in a dry-oven at 120 ℃ for 30 min. The dried FTO substrate was subjected to UV treatment to render the surface hydrophilic. For the initial seed layer, 3 g of poly vinyl alcohol (fully hydrolyzed, Sigma) and zinc acetate dehydrate (99.999 %, Sigma) were dissolved in 50 mL of D.I. water under continuous stirring at 95 ℃ for 24 hr. The prepared solution was coated on a UV treated FTO substrate by spin-coating at 5000 rpm f-or 1 min. The coated FTO glass was annealed at 520 ℃ for 1 hr in a muffle furnace.

ZnO nanosheet layers have been synthesized by two different methods. For the growth curved plates of ZnO nanosheet layer (CPZ layer), 11 mg of zinc acetate dehydrate (99.999 %, Sigma) and 2 mg ethylene imine polymer (M_w~2000, 50 wt.% in H_2O, Sigma) were dissolved in 50 ml of D.I. water with continuous stirring for 2 hr. The solution was then coated on the initial seed layer coated FTO glass using spray coating by an air brush with O_2 gas (O_2 gas flow : 3 L/min, solution flow : 2 mL/min) and then dried under room temperature for 4 hr. The sprayed ZnO layer was then annealed at 520 ℃ for 1 hr in a muffle furnace. MSZ layer has been synthesized by chemical bath deposition method. 9 g of zinc acetate dehydrate (99.999 %, Sigma) was dissolved in 200 ml anhydrous methanol (99.8%, Simgma) and initial seed layer coated FTO glass was immersed in the solution at room temperature for 3 days.

Oriented ZnO nanorod was grown on both ZnO nanosheet in an aqueous solution containing 5 mM zinc nitrate hexahydrate (99.0 %, Sigma) and 5 mM hexamethylenetetramine (99.5 %, Sigma) at 85 ℃ for 6 hr. The substrate was placed in an inverted position. After the growth, the electrode was rinsed with D.I. water and further annealed at 520 ℃ for 1 hr.

3.2.2. Fabrication of dye sensitized solar cells with ZnO photoanode

The ZnO nanorods oriented on ZnO nanosheet electrodes prepared as described above, were soaked in a dye solution by instant method. The electrodes immersed in 20 mM $(Bu_4N)_2[Ru(dcbpyH)_2(NCS)_2]$ (N719) in heated ethylene glycol (1,2-ethanediol, 99.9%, Sigma) with 100 ℃ for 3min. and washed out the residual dye solution by lukewarm (~40 ℃) ethanol. The dye coated ZnO photoanode was assembled with platium coated FTO glass as the counter electrode. The sandwiched cells were sealed using 25 μm transparent (Surlyn 1472) polymer film at 100 ℃ with pressure. Finally, the electrolyte was introduced to internal space through small holes drilled in the counter electrodes, which were immediately sealed and covered with slides and additional strips of Surlyn film to avoid leakage of any

electrolyte.

3.2.3. Characterization of properties

The photoelectrochemical properties of the solar cell were studied by recording the current-voltage characteristics of the cell measured by using a computer-controlled digital source meter (model 2400, Keithly) and a solar simulator (AM 1.5, 100 mW/cm^2 ; model ORIEL-Sol-3A, Newport) as a light source. The light intensity was adjusted with a reference Si photo-device. The active area of the dye-coated ZnO electrode was 0.18 cm^2. The incident photon to current conversion efficiency (IPCE) was measured by IPCE equipment (model QEX7 series, PV measurements, Inc.). The synthesized product was characterized by FE-SEM (Quanta 200, FEI, USA), TEM (JEOL JEM-2010), XRD (Rigaku, with Cu $K\alpha$ radiation and Raman spectra meter (Raman microscope, Renishaw)

3.3. Result & Discussion

Figure 3-1. (a)-(e) present field emission scanning electron microscopy (FE-SEM) images of ZnO nanostructures formed on the FTO glass. Figure 3-1. (a) is 45 ° tilted image of the ZnO initial seed layer grown by spin-coating method. It shows a uniform, continuous, and porous seed layer with film thickness of ~200 nm. Figure 3-1. (b) shows CPZ layer built by an air brush method with a layer thickness of ~2 μm. The layer consist of saddle like nanosheets with a sheet thickness of ~70 nm. Figure 3-1. (c) shows MSZ layer with thickness of ~ 2 μm, which form well connected networking. Figure 3-1. (d), (e) show   high resolution image of the prickled rough surfaces (rods) on the nanosheet layers. Well grown hexagonal nanorods was observed at CPZ layer with diameter of 50(±1) nm and average length of 300(±30) nm in Figure 3-1. (d). However nonarods on MSZ layer were blunt and short with average aspect ratio of ~1.2 in Figure 3-1. (e). It is thought that surface of saddle like nanosheets of CPZ layer was exposed with (001) plane of ZnO when building up with air brush method, so nanorods could be grown well on it with [001] direction.
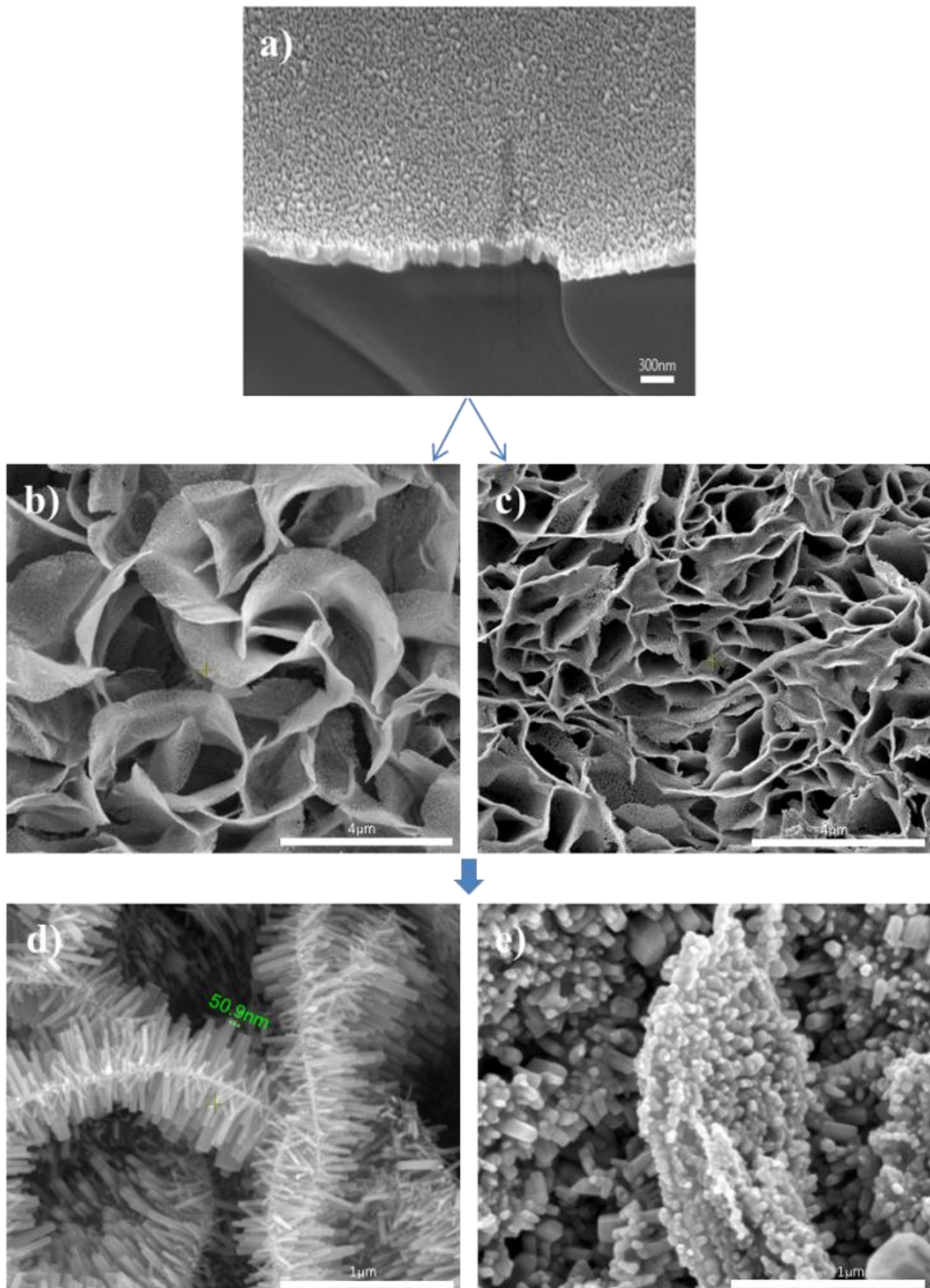
Figure 3-1. FE-SEM image of (a) ZnO initial seed layer (b) CPZ layer and (c) MSZ layer synthsized on initial seed layer. ZnO nanorods on (d) CPZ layer and (e) MSZ layer

Figure. 3-2. (a) shows XRD patterns of the synthesized ZnO nanostructures. The observed diffraction peaks are assigned to the hexagonal-phase of ZnO reported in the literature. (JCPDS card no. 36-1451; Wurtzite-type, space group P63mc (a = 3.249Å , c = 5.206 Å with a unique polar axis parallel to the c-axis). The peak intensities of (100), (002) and (101) planes are 59, 47 and 100 on MSZ layer, and 87, 58 and 100 on CPZ layer, respectively. So the XRD pattern of nanostructure on MSZ layer shows almost random orientation and on CPZ layer shows a bit prefer orientations with [002] direction. Figure. 3-2. (b) shows a HR-TEM image of nanorod on CPZ layer and a fringe distance of 0.26 nm was observed, consistent with a wurtzite structure. Selected area electron diffraction (SAED) patterns show a single crystalline nature. In addition, the spots are very clear, showing a two-fold symmetry of synthesized ZnO nanocrystals, in good agreement with hexagonal wurtzite phases with [0002] direction. SAED taken from individual nanorods, as shown in the inset, indicate a single crystalline morphology in nature and the spots clearly exhibit a two-fold symmetry.
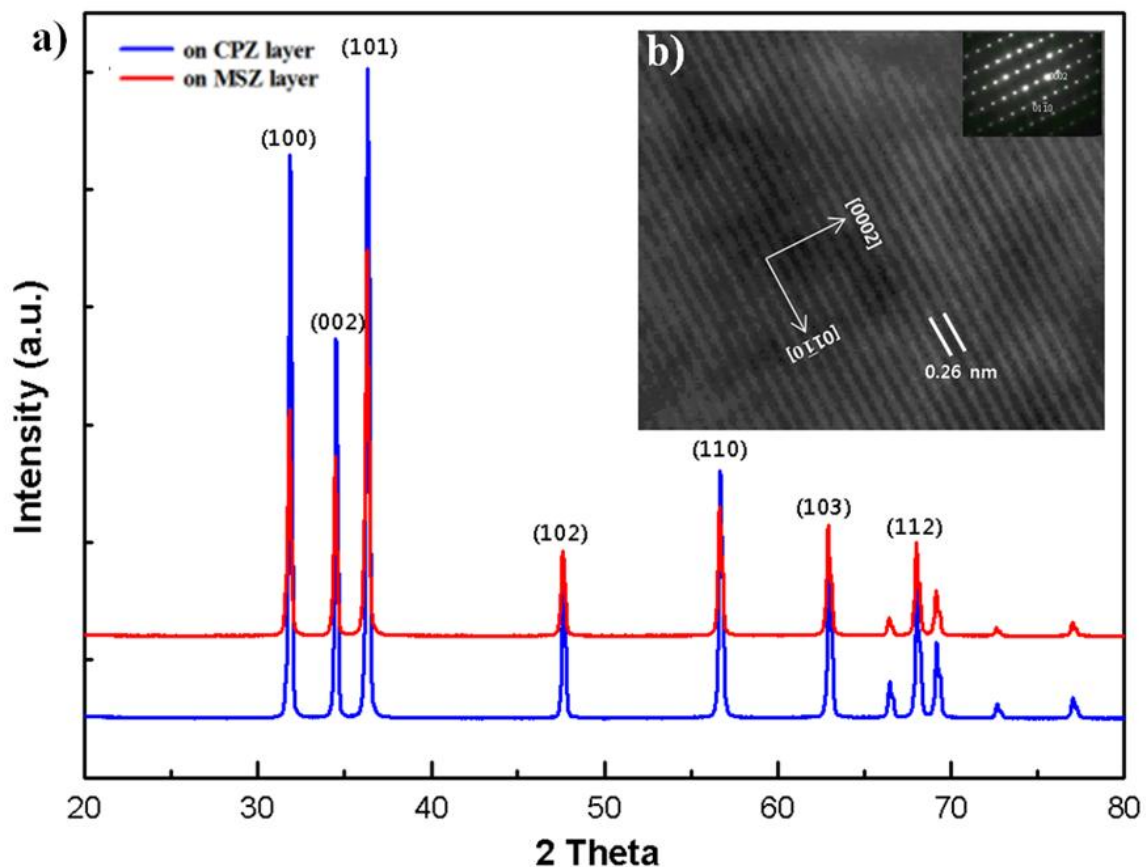
Figure. 3-2. (a) X-ray diffraction patters of grown ZnO nanostructure on CPZ layer (blue) and MSZ layer (red), (b) HR-TEM image and SAED pattern showing single crystal of the ZnO nanorod

Figure. 3-3. depicts the Raman spectra of synthesized oriented ZnO nanocrystal arrays obtained by a mild solutions route on FTO glass. The Raman spectra are an important tool to study ZnO nano/micro

crystals. Four Raman peaks, at 331, 378, 436, and 576 cm^{-1}, were observed with the dominant peak at 436 cm^{-1}. The three Raman bands located at 436, 378, and 331cm^{-1} are ascribed to ZnO E_2, A_{1T} mode, and the multiphonon process for a ZnO single crystal, respectively.[82] The low intensity peak of oxygen deficiency related to the Raman peak at 576 cm^{-1} suggests the presence of few oxygen vacancies in our synthesized samples. The Raman peak at 378 cm^{-1} is attributed to the A_1 mode of ZnO. In our samples, the broad, sharp dominant peak at 436 cm^{-1} is attributed to the main ZnO peak and is typical of E_2 of wurtzite hexagonal ZnO structures, thus showing the main component in these samples is wurtzite phases, consistent with the XRD patterns. Furthermore, no impurities or reaction product peaks were observed in the synthesized samples, further verifying the high quality of our synthesized samples.[83]
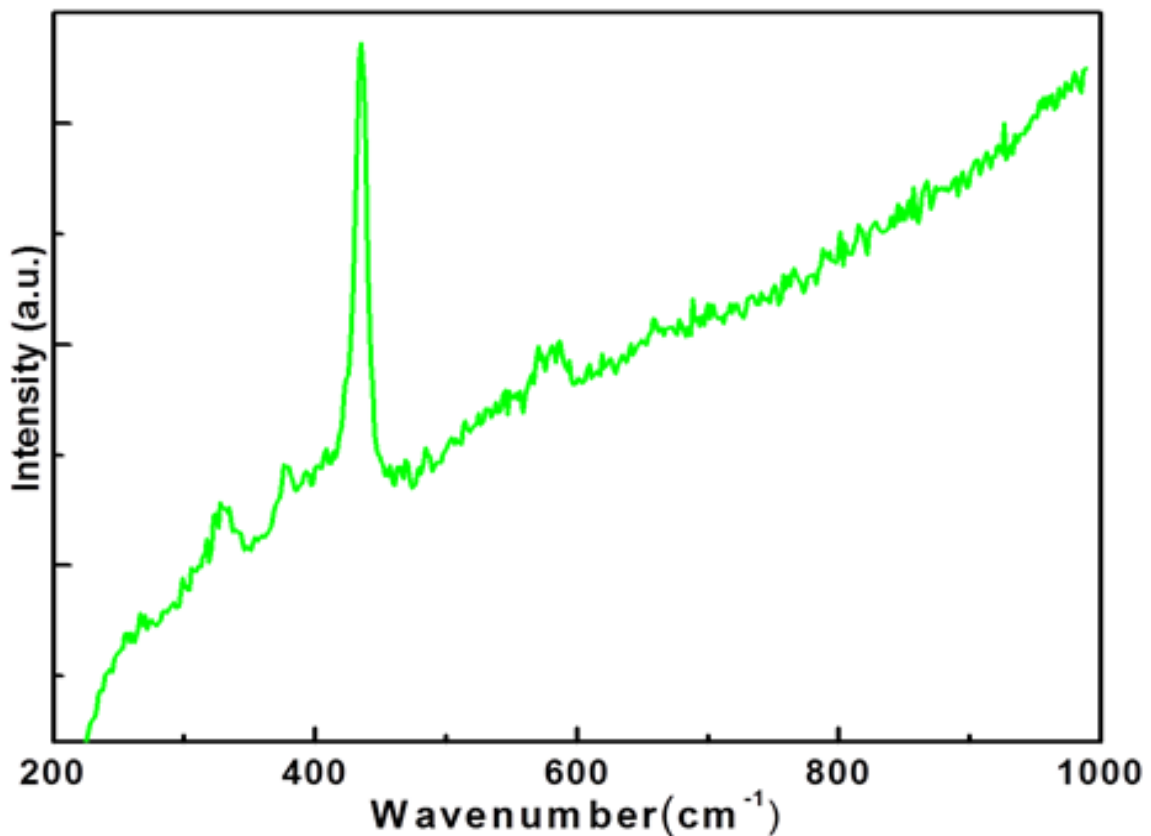
Figure 3-3. Raman spectra of setose ZnO nanorods on CPZ layer which has been built up by air-brush method.

The photovoltaic performance of the the cells are show in Figure 3-4. and Table 3-1. The cell with MSZ layer exhibits a power conversion efficiency(PCE) of 0.84 % and short circuit current (J_{sc}), open circuit voltage (V_{oc}), and fill facot (*FF*) of 6.4 mA/cm^2, 0.72 V, and 0.66, respectively. On the cell with CPZ layer, the J_{sc} increases by 49 % to 6.4 mA/cm^2 with an increase of the PCE up to 3.04 %. The IPCE spectra in Figure 3-4. (b) show J_{sc} enhancement of the cells with CPZ layer and MSZ layer that havr maximum absorption of 39% and 25 % at 550 nm, respectively.
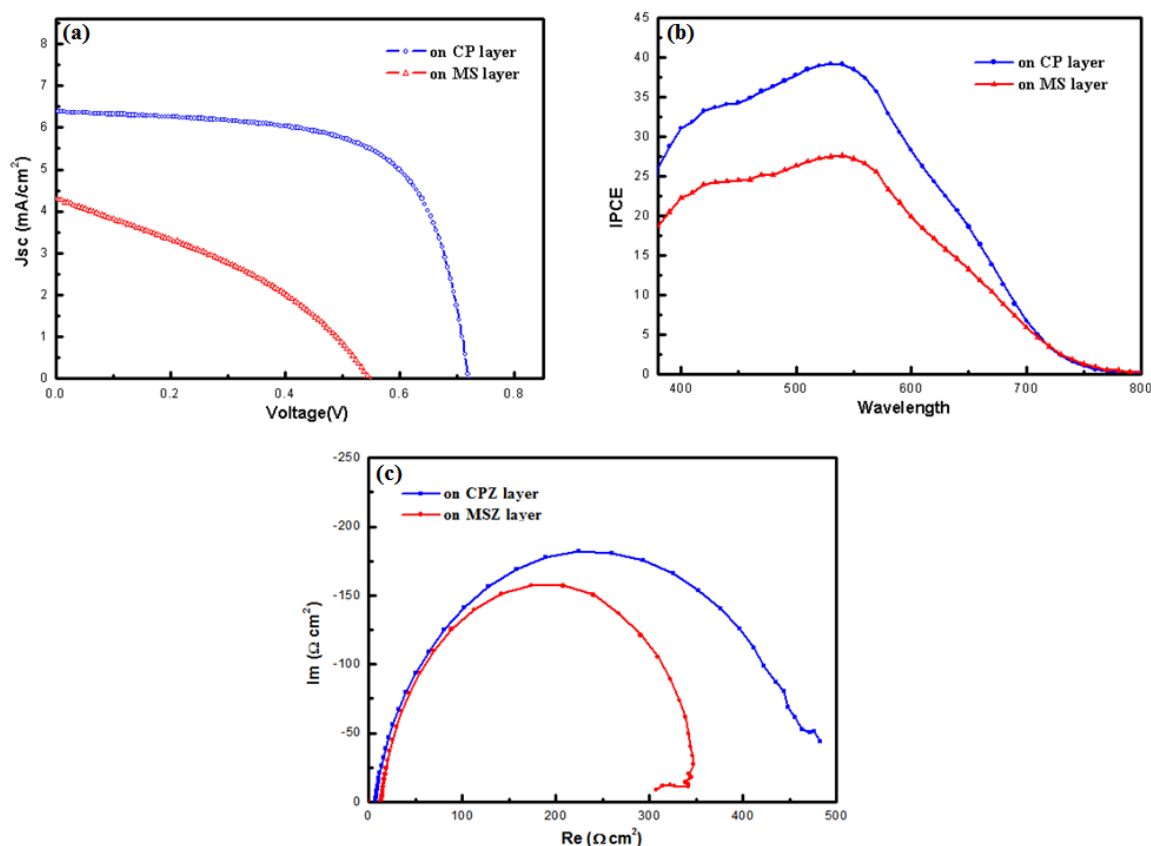
Figure 3-4. (a) J-V curve, (b) incident to photocurrent efficiency (IPCE) and (c) Nyquist plots of ZnO nanorod on CPZ layer (blue), MSZ layer (red)

ZnO electrode	PCE(%)	J_{sc}(mA/cm^2)	V_{oc}(V)	FF	Dye loaing[a] (mol/cm^2)
CPZ layer	3.04	6.4	0.72	66.0	4.21×10^{-8}
MSZ layer	0.84	4.3	0.55	36.1	1.75×10^{-8}

[a] Amount of adsorbed dye on ZnO measured by UV-Vis Spectrascopy

Table 3-1. Photovoltaic performance of cell with CPZ layer and MSZ layer

For comparison of amount of dye adsorption, the dye coated working electrodes were immersed into a NaOH aqueous solution. The basic solution removes all the dye molecules from the ZnO surface, and the amount of dye can be compared by UV spectroscopy analysis. A concerntration of adsorbed dye on the ZnO nanorod electrode of CPZ layer is 4.21×10^{-8}, and of MSZ layer is 1.75×10^{-8}. This result explain the enhancement of J_{sc} is due to large surface area of setose ZnO nanostructure of nanorods with CPZ

layer. Electrochemical impedance spectroscopy (EIS) was employed to investigate the interfacial properties of DSSCs. To investgate interface of TiO_2/electrolyte, EIS was took on the condition of 0.5 V in the dark. Figure 3-4. (c) shows the Nyquist plots of DSSCs with photoanode of ZnO nanostructure represent TiO_2/electrolyte interface. The cell with MSZ layer shows lower charge transfer resistance than CPZ layer's one. (348 $\Omega \cdot cm^2$ and 452 $\Omega \cdot cm^2$, respectively) These results indicated that recombination between TiO_2 and electrolyte occurred well in this interface. MSZ layer with the nanoplate between the nanowalls impedes penetrating of dye solution to bottom of ZnO nanostructure. We applied instant adsorption method, bottom of ZnO nanostructure contact with dye solution insufficiently and the region remain naked. The electrons, which come from excied dye to ZnO, were recombined with electrolyte through the naked region. For this reason, Voc and FF show low value in cell with MSZ layer. On CPZ layer, there is no obstacles for penetrating of dye solution, the photoanode of the cell with CPZ layer was fully adsorbed by N719 dye.

3.4. Conculsion

In this study, we showed a novel ZnO nanostructure for photoanode of DSSCs. The air brush method provide well-built seed layer as CPZ layer for ZnO nanorod growth. Setose ZnO nanostructure with CPZ layer have adventges for application in DSSCs as large surface area and good morphology for penetrating of the dye solution. The cell with CPZ layer shows developed power conversion efficiency that surpass the cells with conventional method of synthesis. This work provides intriguing way of structurally designing of ZnO with large surface area and moderate morphology for DSSCs and other applications.

Chapter 4. Mesoporous carbon for counter electrode of DSC

4.1. Introduction

The CE is one of the most important components in the DSSCs; it returns electrons to the electrolyte via iodide reduction.[84] The materials for CE should provide sufficient electrocatalytic activity for iodine reduction and facilitate fast diffusion of electrons and ions. Yet, thus far, only a limited number of materials have been successfully used as CEs owing to the corrosion of metals by the iodine electrolyte. Vapor-deposited Pt is currently the prevalent material of choice, primarily because of its high electrocatalytic activity. However, prohibitively high costs and limited supplies of Pt has triggered a great deal of recent efforts toward seeking low-cost alternatives for Pt. For instance, metal sulfides,[85-86] nitrides,[87-88] and carbides[89-90] that have previously shown Pt-like catalytic activity in heterogeneous catalysis have been utilized as DSSC CEs. As more cost-effective materials for CEs, a variety of carbons have been exploited,[91] examples of which include activated carbons,[60] carbon nanotubes (CNTs),[92-94] carbon nanofibers,[95] graphene,[96-98] graphite,[99] and ordered mesoporous carbons (OMCs).[100-102] In particular, recently discovered nanostructured carbons such as CNTs, graphene, and OMCs have appealing structural properties that are beneficial for DSSCs including high electrical conductivity and well-developed porous structures. As such, these nanocarbon-based CEs have shown promising applicability for DSSCs. However, the efficiency of these DSSCs is lower than that of DSSCs with a Pt-based CE.

Herein, we report the preparation of nanocomposites of OMC and CNTs in a single step from a single precursor and their successful application as novel, Pt-free, highly efficient and durable DSSC CEs. OMC–CNT nanocomposites have a unique structure wherein the primary particles of the OMC are interconnected via the CNTs, thus exhibiting a nanomedusa-like morphology. Most importantly, the OMC–CNT nanocomposites combine the advantageous properties of both OMC and CNTs. The high surface area of OMC provides numerous catalytically active sites for iodine reduction while its three-dimensionally (3-D) interconnected mesoporous structure allows for the facile transports of ions and electrons. In addition, CNTs can function as electrical bridges that interconnect separated OMC primary particles, thus generating fast electrical networks. We show that the DSSC employing the OMC–CNT-based CE exhibits an excellent cell efficiency, which rivals that of the DSSC cell with a conventional Pt-based CE. Furthermore, we demonstrate that the DSSC with the OMC–CNTs-based CE shows remarkable stability in a long-term efficiency test.

4.2. Experimental

4.2.1. Synthesis of OMC–CNT nanocomposites

A hexagonally ordered OMS template was synthesized following the literature method for SBA-15 silica[103-104] with the modification of hydrothermal treatment temperature at 150℃. The OMC–CNT nanocomposites were synthesized by a solid state nanocasting method using OMS and Ni-phthalocyanine (NiPc, Aldrich) as a template and as a precursor, respectively.[105] 1.0 g of calcined OMS was mixed with 1 g of NiPc, and the mixture was grinded for 10 min in a mortar and transferred to an alumina crucible. The mixture was then heated to 900℃ with a ramping rate of 2.5℃ min^{-1} and remained at that temperature for 3 h under Ar flow. The resulting carbon-silica composite was then washed twice with hydrofluoric acid (50 wt%, J.T.Baker) at room temperature for 1 h to remove the OMS template. The synthesis of OMC was achieved using the same procedure as that for the OMC–CNT nanocomposites, except for the use of phthalocyanine (Pc, Aldrich) as the carbon precursor.

4.2.2. DSC tests

FTO glass (TEC-8, Pilkington) was cleaned by sonicating in ethanol, acetone, and then isopropanol for 10 min and UV exposure for 20 min. A Doctor blade process was applied to evenly apply TiO_2 paste (ENB Korea, 20 nm) on cleaned FTO glass with a thickness of around 12   m, and the sample was subsequently sintered at 500℃ for 80 min. $TiCl_4$ treatment was carried out by placing the sample in 40 mM $TiCl_4$ aqueous solution for 30 min followed by sintering at 500℃ again for 30 min. Dye coating was performed in 0.3 mM of N719 solution in acetonitrile/ter-buthanol (1:1 vol.) for overnight. The counter electrode (CE) was prepared with materials of interest. For a reference, CE with Pt was prepared by spin-coating (2000 rpm, 5 times) 20 mM of H_2PtCl_6 solution in isopropanol on FTO glass 5 times and sintering at 400℃ for 1 h. For the OMC–CNT nanocomposites and OMC, each material was dispersed in an organic vehicle (2-methoxy-ethanol), and an ultrasonic disperser (Sonics, 750) was applied for 5 min, and composition ratio was set at 1:100 (wt %). The mixture was loaded on FTO glass by spin-coating (1500 rpm, 3 times) and sintering at 400℃ under Ar condition. Finally, the electrodes were assembled, and an electrolyte was added through a pre-drilled hole. The hole was sealed with Surlyn and a piece of thin glass. The composition of the electrolyte was 0.5 M 1-hexyl-2,3-dimethylimidazolium iodide (99.9%, C-tri), 0.02 M iodine (ACS regent, Aldrich), 0.5 M 4-tert-buthylpyridine (Aldrich), and 0.05 M lithium iodide (Aldrich) in acetonitrile. J-V characterization was carried out under 1 Sun condition with Oriel SOL3A solar simulator by obtaining open circuit voltage (V_{oc}), short circuit current (J_{sc}), fill factor (FF), and overall efficiency (η).

4.2.3. Electrochemical and physicochemical characterizations:

Electrochemical impedance spectroscopy (EIS) and cyclic voltammetry (CV) were completed with Solartron. For CV, Ag/AgNO$_3$ and Pt mesh were used as a reference electrode and counter electrode, respectively. The electrolyte for CV was prepared with 1 mM I$_2$, 10 mM Lithium iodide, and 100 mM LiClO$_4$ in N$_2$ purged acetonitrile, and the scan rate was 100 mV/s. Morphology of the samples was analyzed by scanning electron microscope (SEM) using a FEI Quanta 200 microscope operating at 15 kV, whereas internal pore structures were visualized by transmission electron microscope (TEM) images using a JEOL JEM-2100F microscope at an accelerating voltage of 200 kV. X-ray diffraction (XRD) patterns of the samples were measured with a Rigaku D/Max 2500V/PC X-ray diffractometer equipped with a Cu K$_\alpha$ source at 40 kV and 200 mA. Porous structures of the samples were analyzed by nitrogen adsorption at - 196℃ using a BEL Belsorp-Max machine. Surface areas and pore size distributions of the samples were calculated by using the Brunauer-Emmett-Teller (BET) equation and the Barrett-Joyner-Halenda (BJH) method, respectively. The carbon and nitrogen contents in the samples were determined by Thermo Scientific Flash 2000 elemental analyzer. Themogravimetric analysis (TGA) was conducted in air and argon atmospheres at a heating rate of 10℃min^{-1}, using a TA Hi-Res TGA 2950 thermogravimetric analyzer.

4.3.   Result & Discussion

Our fabrication approach for OMC-CNT nanocomposites is shown in Figure 4-1. Our synthesis was achieved via the nanocasting route using SBA-15-type, hexagonally ordered mesoporous silica (OMS)[103-104] as a template and nickel phthalocyanine (NiPc) as a precursor.[105] NiPc has previously been shown to be an effective source for CNT growth, wherein the aromatic functional groups of NiPc are used as a carbon source and the Ni metal acts as a catalyst.[106] In the present work, NiPc was used as a source for an OMC structure as well as for CNTs. For the preparation of an OMC-CNT nanocomposite, NiPc was first mixed with an OMS template in solid state and subsequently infiltrated into the mesopores of OMS during a high-temperature treatment under inert atmosphere. After carbonizing and removing the OMS template with HF, the OMC–CNT nanocomposites were generated. These nanocomposites represent the first example of simultaneous one-step formation of OMC and CNTs from a single precursor. On the other hand, when the carbon source was substituted with metal-free phthalocyanine (Pc), the resulting carbon nanostructure was composed of only CMK-3-type OMC without the formation of any CNTs.
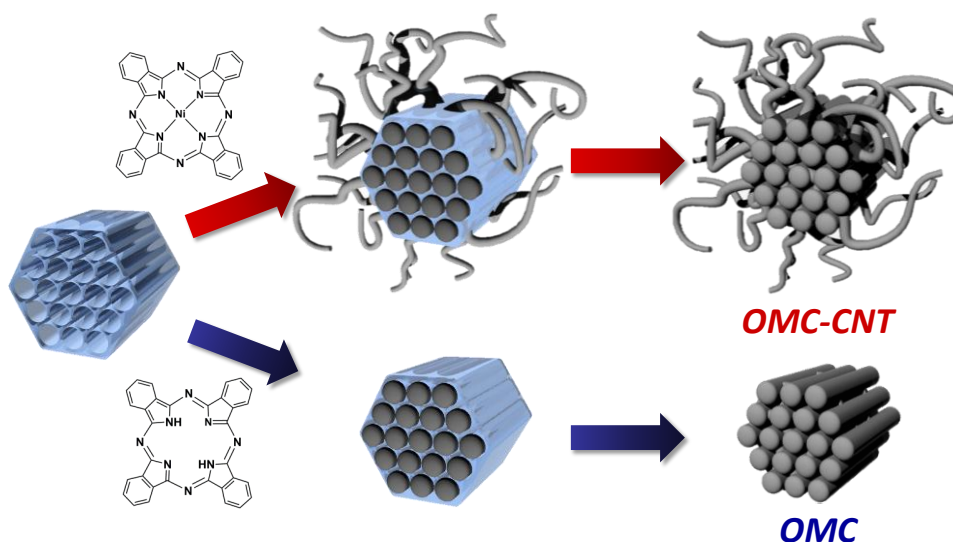
Figure 4-1. Schematic illustration for the preparation of OMC-CNT and OMC

We first examined the evolution of morphologies and pore structures of the templated carbon materials by scanning and transmission electron microscopies (SEM and TEM, respectively) as shown in Figure 4-2. The SEM image of the OMS (Figure 4-2.a) showed short rod-like, near–spherical morphology. The TEM image of the OMS viewed along the channels (Figure 4-2.b) clearly showed the hexagonal arrangement of uniform mesopores with a diameter of around 12 nm. The SEM image of the OMC derived from Pc (Figure 4-2.c) was very similar to that of the OMS, indicating that the original morphology of the OMS was maintained after carbon replication. The TEM image of the Pc-based OMC (Figure 4-2.d) indicated that the internal pore structure of the OMS was completely reversed in the OMC because the mesopores and silica walls of the OMS were replicated into carbon frameworks and mesopores of the OMC, respectively. In contrast, the carbon nanostructure prepared from the NiPc precursor showed clearly different morphology from that of OMS and OMC. The SEM (Figure 4-2.e and g) and TEM (Figure 4-2.f and h) images of the NiPc-driven carbon nanostructure indicated that CNTs as well as spherical OMC particles were formed after carbon replication and that the primary particles of the OMC were interconnected via the CNTs, thus forming medusa-shaped OMC–CNT nanocomposites. A closer observation of the OMC–CNT nanocomposites (Figure 4-2.g and h) revealed that the CNTs protruded from the OMC particles. It was found that during high-temperature treatment NiPc precursors were sublimated and carbonized inside the mesopores of the OMS, thus forming the rigid carbon structures throughout the mesopores of the OMS. Meanwhile, the precursors that adsorbed on the surfaces or the pore mouth of the OMS were converted into CNTs. The distribution of elements in the OMC–CNT nanocomposites analyzed by energy dispersive X-ray spectroscopy (Figure 4-3.) revealed that nitrogen, nickel, and carbon were all uniformly distributed over the OMC–CNT particles. Thermogravimetric analysis (Figure 4-4.), in combination with inductively coupled plasma analysis,

indicated that the OMC–CNT nanocomposites consisted of 69 wt% OMCs, 28.5 wt% CNTs, and 2.5 wt% Ni metal.
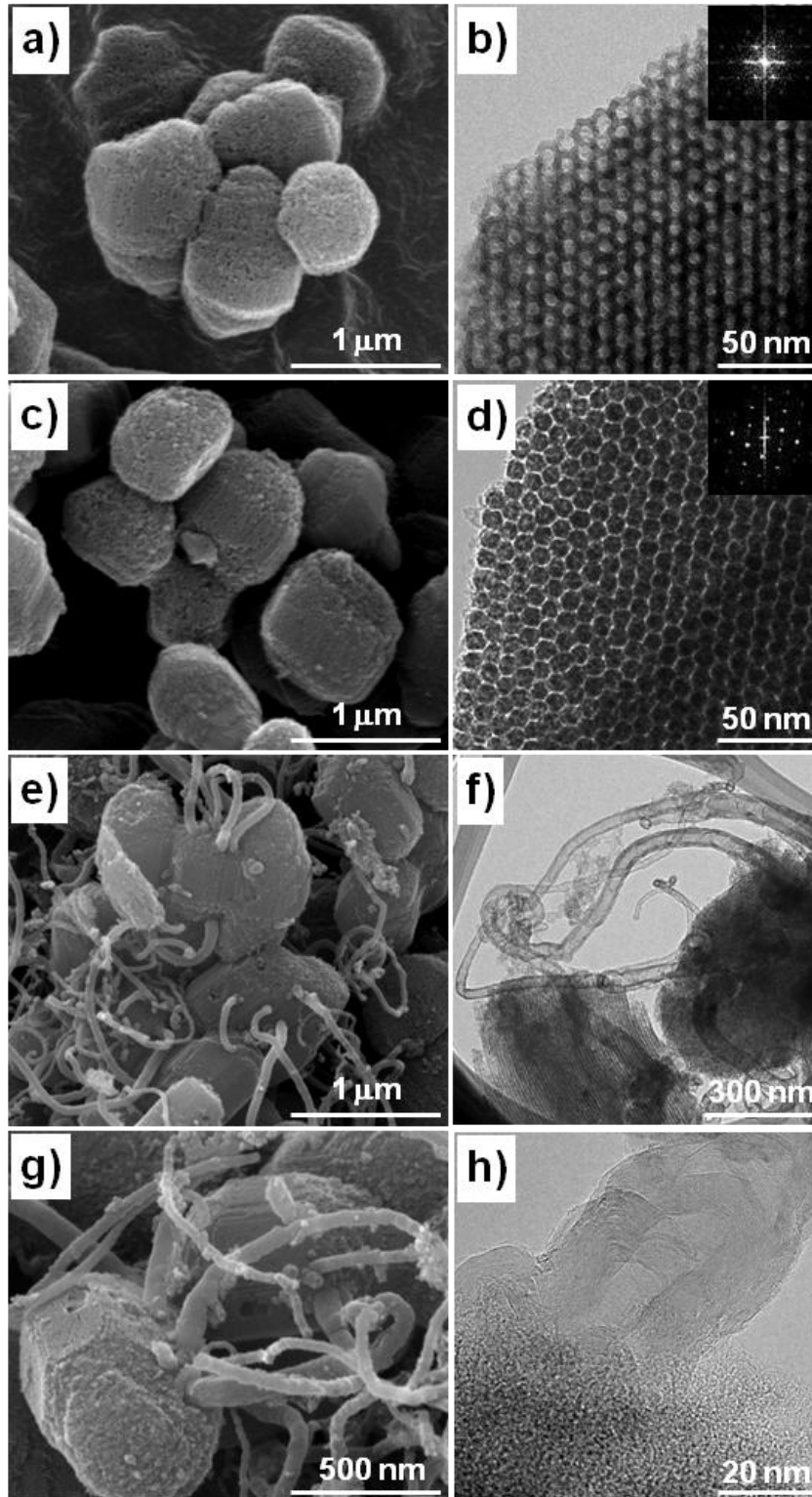
Figure 4-2. SEM (a,c,e,g) and TEM (b,d,f,h) images of the samples: (a,b) OMS, (c,d) OMC, and (e–h) OMC–CNT. Insets in (b) and (d) are electron diffraction patterns for OMS and OMC.
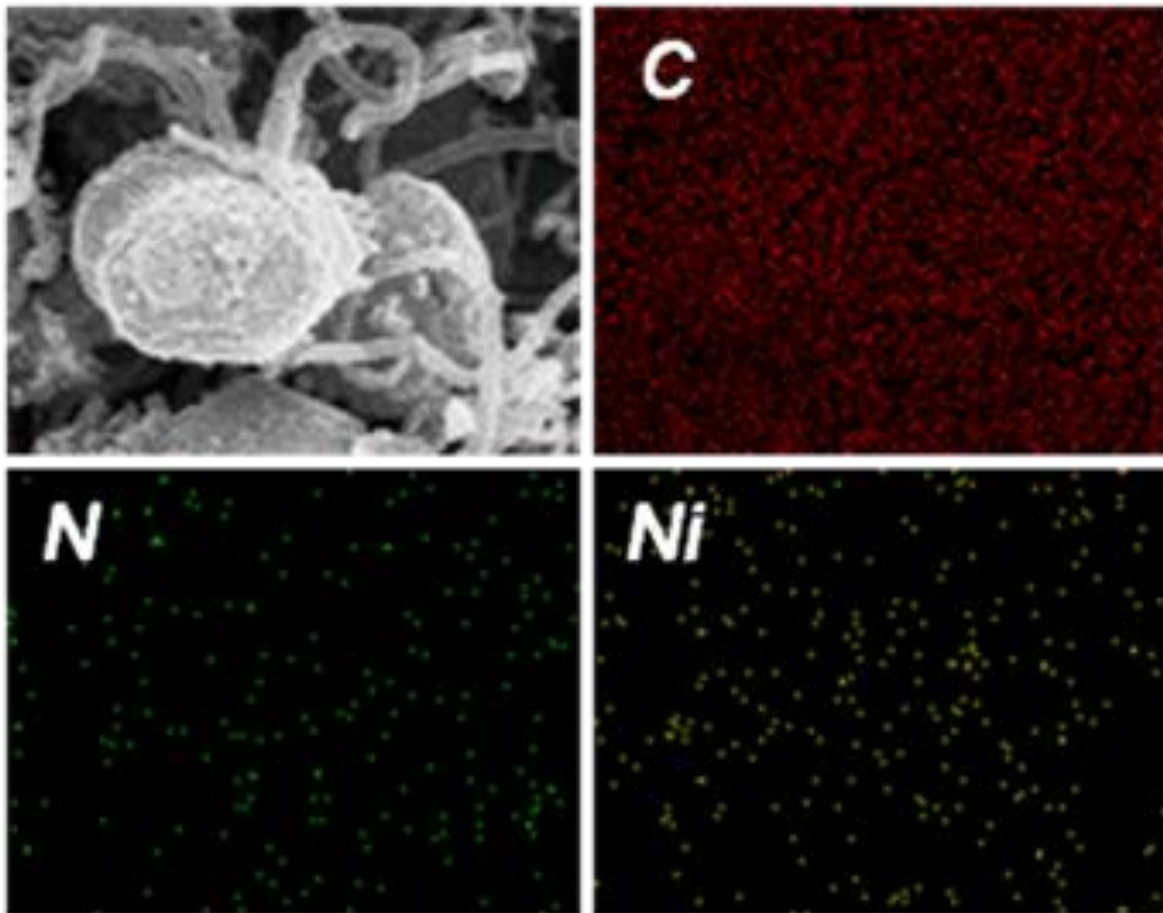
Figure 4-3. Energy dispersive X-ray spectroscopy analysis of OMC–CNT
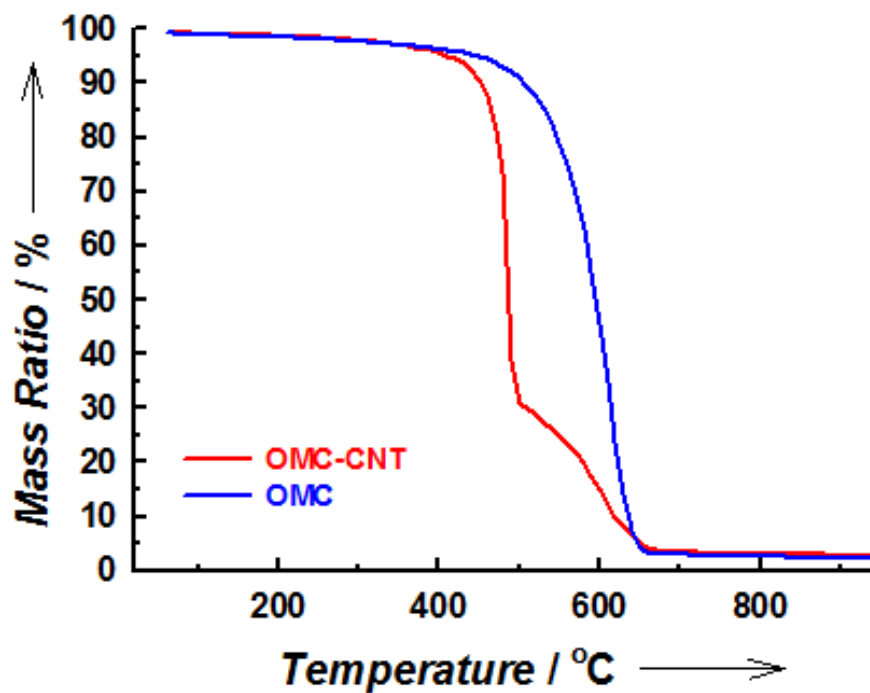
Figure 4-4. Thermogravimetric analysis of OMC–CNT and OMC samples

The structural properties of the OMC and OMC–CNT nanocomposites were investigated by X-ray diffraction (XRD) (Figure 4-5.a and b). The low angle XRD patterns of both OMC and OMC–CNT nanocomposites showed three distinct XRD diffraction lines that corresponded to the (100), (110), and (200) reflections of a hexagonal mesostructure, which are similar to that of the OMS. This indicated that the hexagonal structure of the OMS template was maintained in both the OMC and OMC–CNT replicas, which was consistent with the TEM observations. In high angle XRD patterns (Figure 4-5.b), the OMC showed a featureless, broad peak around 24° indicative of an amorphous nature of the carbon framework. In contrast, the OMC–CNT exhibited a very sharp peak centered at 26.3°, corresponding to the (002) diffraction of graphite. We suggest that the graphitic character of the OMC–CNT nanocomposites may originate from the graphitized OMC frameworks catalyzed by the Ni species as well as from the highly graphic CNTs. It is worth noting that the characteristic peaks for Ni or NiO were detected at 43-45°, indicating that the existence of Ni species that could be used for CNT growth.
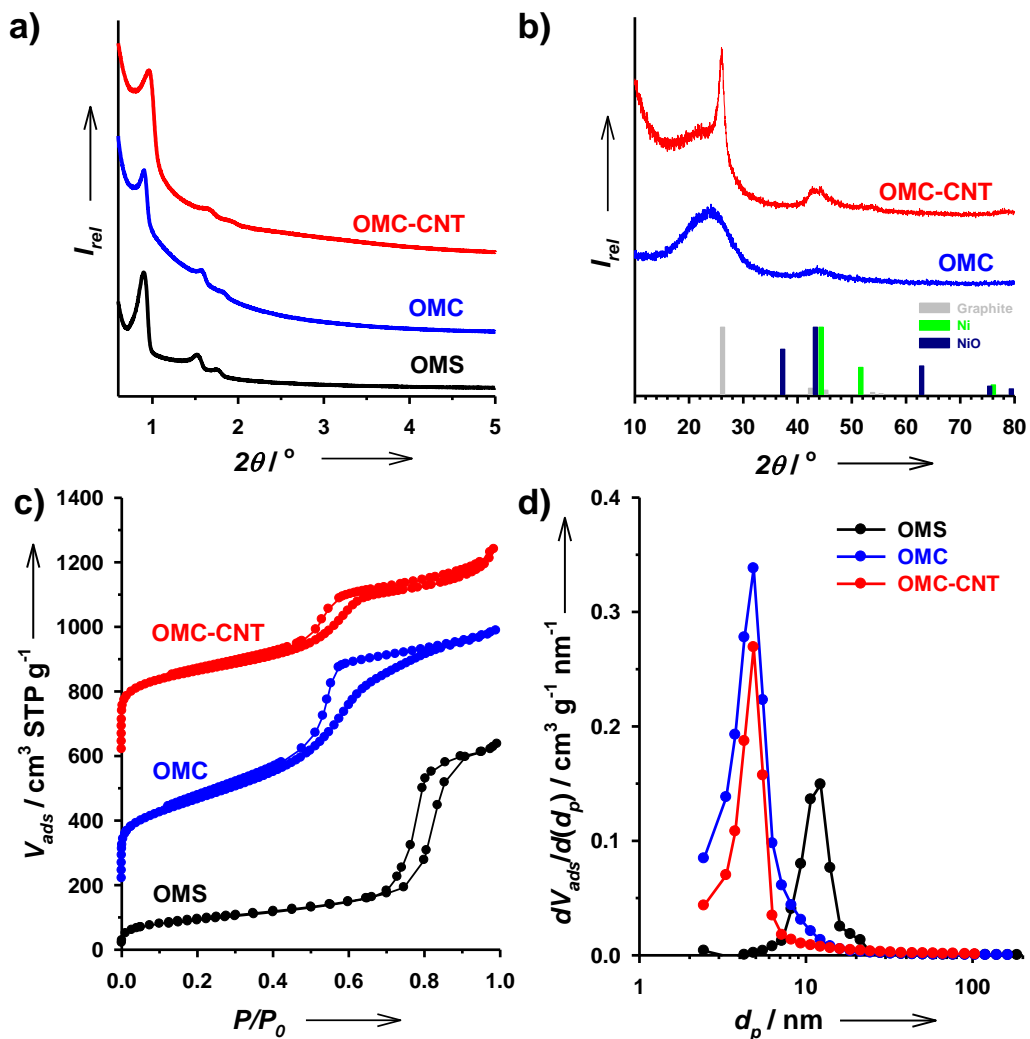
Figure 4-5. a) Low angle and b) wide angle XRD patterns, c) nitrogen adsorption isotherms, and d) pore size distributions of OMS, OMC, and OMC–CNT samples. In (c), isotherms of OMC and OMC–CNT samples were shifted upwards 200 and 600 cm^3g^{-1}, respectively, for clarity.

The pore structures of the materials were assessed by performing nitrogen adsorption experiments (Figure 4-5.c and d). The OMS template exhibited a type–IV isotherm with a hysteresis loop typical of SBA-15-type mesoporous silica. The templated OMC and OMC–CNT nanocomposites showed a similar shape of isotherms and the same pore size of 4.9 nm. This indicated that the formation of CNTs did not clod the mesopores of the OMC-CNT nanocomposites and the open uniform mesopore system of the OMC was maintained in the OMC–CNT nanocomposites. The BET surface areas and pore volumes of the OMC and OMC–CNT nanocomposites were as follows: 950 m^2g^{-1} and 1.22 cm^3g^{-1} for the OMC, and 940 m^2g^{-1} and 0.99 cm^3g^{-1} for the OMC–CNT nanocomposites.

The physicochemical characterizations of the replicated carbon structure confirmed the fact that new, medusa-shaped nanocomposites of two distinct carbon entities - OMC and CNTs - were successfully prepared. The key factor in the preparation of the OMC–CNT nanocomposites was the use of NiPc as a precursor for the carbon nanostructures. The preparation of similar OMC–CNT nanocomposites has been reported previously.[107] However, it required a laborious multi-step process: the preparation of an OMC, a Ni catalyst deposition, and the growth of CNTs. In contrast, the OMC–CNT nanomedusa structures could be obtained from a single precursor, NiPc, in a single step. The resulting OMC–CNT nanocomposites combined the advantages of the two materials, such as high surface area, interconnected mesopore structure, and high electrical conductivity. We consider that the OMC–CNT nanocomposites could be used as new, efficient materials for energy devices wherein the combination of the afore-mentioned attributes is expected to help enhance the device performance. We explored such a possibility by applying the OMC–CNT nanocomposites as the CE of DSC.

We compared the efficiencies of DSSC cells with different CEs: OMC–CNT nanocomposites, OMC, CNTs, and conventional Pt. Figure 4-6. shows photovoltaic characteristics of the samples, and Table 4-1. summarizes the parameters of the DSSCs with different CEs. Most importantly, the OMC–CNT-based cell showed quite a high efficiency (8.4%) that even rivaled that of a Pt-based cell (8.3%), whereas the OMC- and CNT-based cells showed much lower efficiencies (6.7% and 4.0%, respectively) than the Pt reference cell. Slopes at the open circuit voltage (V_{oc}) region are often used to calculate series resistance of devices that consequently affects fill factor (*FF*). When a series resistance is high, the *J-V* curves are contorted like a curve for the CNT-based cell in Figure 4-6. While the OMC–CNT-based cell showed comparable *J-V* curves to the Pt-based cell, the other two carbon-based cells showed much higher series resistances and relatively low *FF*s. We believe that the CNT- and OMC-based cells could have high contact resistances either between carbon particles themselves or between carbons and the

FTO substrate. In contrast, in the case of the OMC-CNT-based cell, CNTs may electrically interconnect the OMC islands, which might facilitate the electron transfers between the OMC particles, thereby lowering the series resistance. Our reasoning could be further substantiated by sheet resistance measurements for the sample electrodes by a four-point probe station. The sheet resistances for the Pt and the OMC–CNT treated electrodes were 8 Ω/cm^2, whereas the sheet resistance for the OMC-covered electrode showed a much higher resistance of 10-100 Ω/cm^2 depending on the thickness, which ranges from 0.5 to 10 μm.
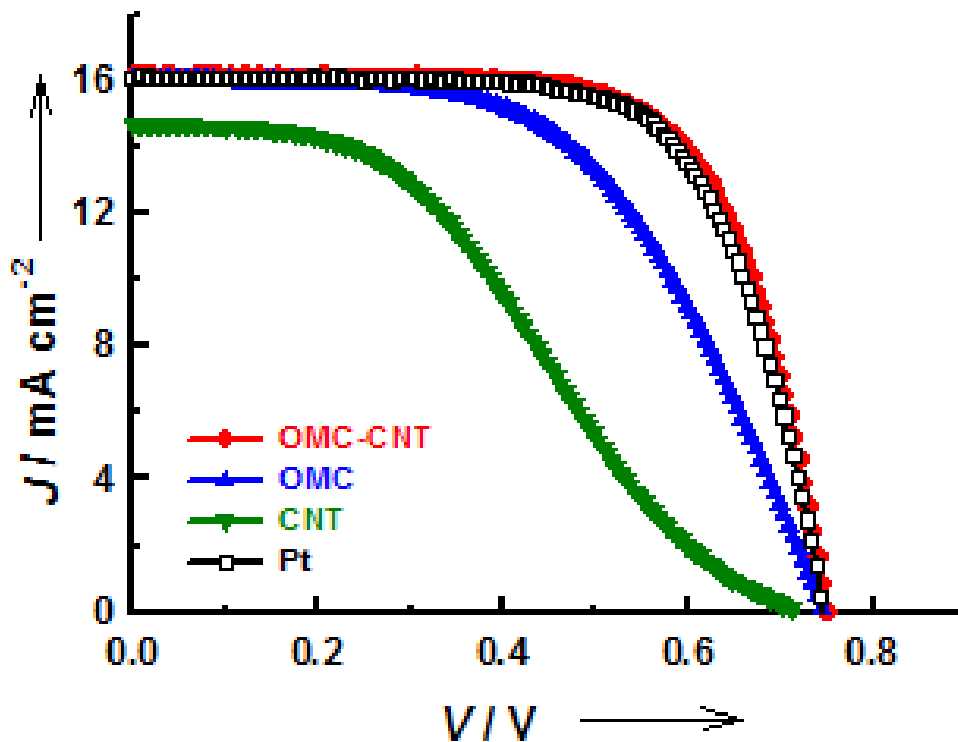
Figure 4-6. Comparison of *J-V* characteristics of DSSCs employing CEs with OMC–CNT, OMC, and Pt.

Sample	V_{oc} (V)	J_{sc} (mA cm^{-2})	FF (%)	(%)	R_{ct} (Ω cm^2)	Z_w (Ω cm^2)	R_s (Ω cm^2)
OMC–CNT	0.749	16.2	69.1	8.4	1.37	7.47	0.74
OMC	0.744	16.0	55.9	6.7	52.75	43.56	1.01
CNT	0.719	14.7	38.0	4.0	2.49	17.01	0.94
Pt	0.749	16.1	68.7	8.3	1.40	6.85	0.68

Table 4-1. Photovoltaic parameters for DSSCs employing different counter electrodes and EIS parameters of dummy cells assembled from these electrodes

Electrochemical impedance spectroscopy (EIS) with a commonly suggested circuit was employed to investigate the interfacial properties of DSC. (Figure 4-7. Figure Figure 4-8.) A Nyquist plot usually shows three arcs, which correspond to resistances at the CE/electrolyte interface, TiO_2+dyes/electrolyte interface, and electrolyte. The first arc is accurately related to electron transfer at the CE/electrolyte interface. When more catalytic effect is observed, a smaller arc (lower resistance) is expected. Figure 4a shows the observed resistances for DSSCs prepared in these experiments, and Table 1 summarizes the values in terms of the first arc resistance as R_{ct}. As expected, the OMC–CNT-based cell showed a similar charge transfer resistance (~ 1.37 Ωcm^2) at the CE/electrolyte interface to the Pt CE (1.40 Ωcm^2). However, the OMC-based cell and CNT-based cells showed higher values (52.7 Ωcm^2 and 2.49 Ωcm^2, respectively) for the first arc. These results indicated that the connection between OMC particles and CNTs synergistically lowered charge transfer resistance in the CE.
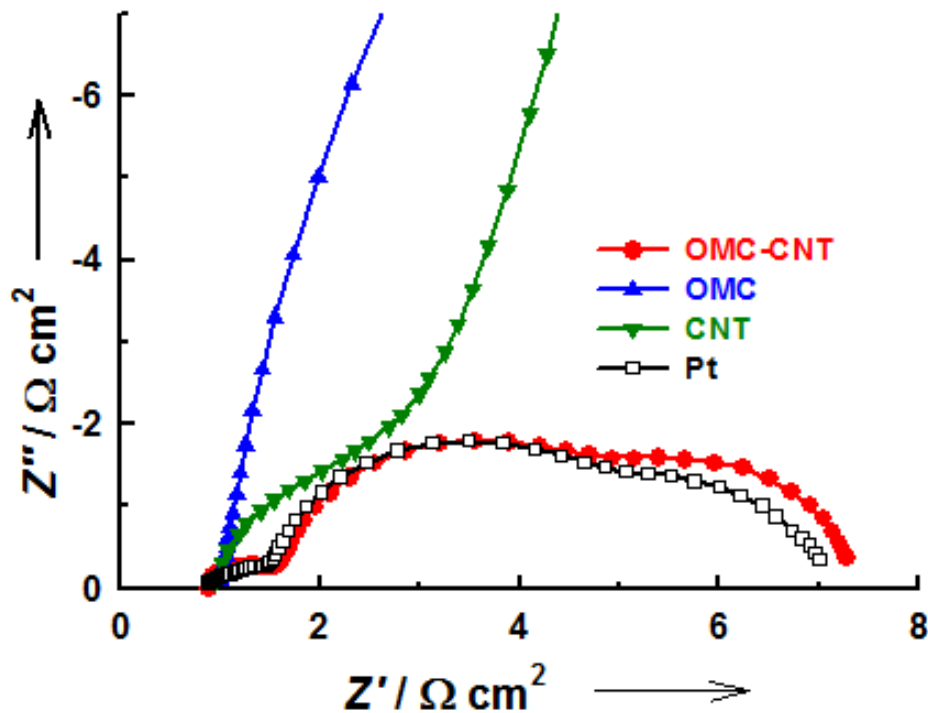
Figure 4-7. Nyquist plots of devices with OMC–CNT, OMC, and Pt under the 1SUN condition
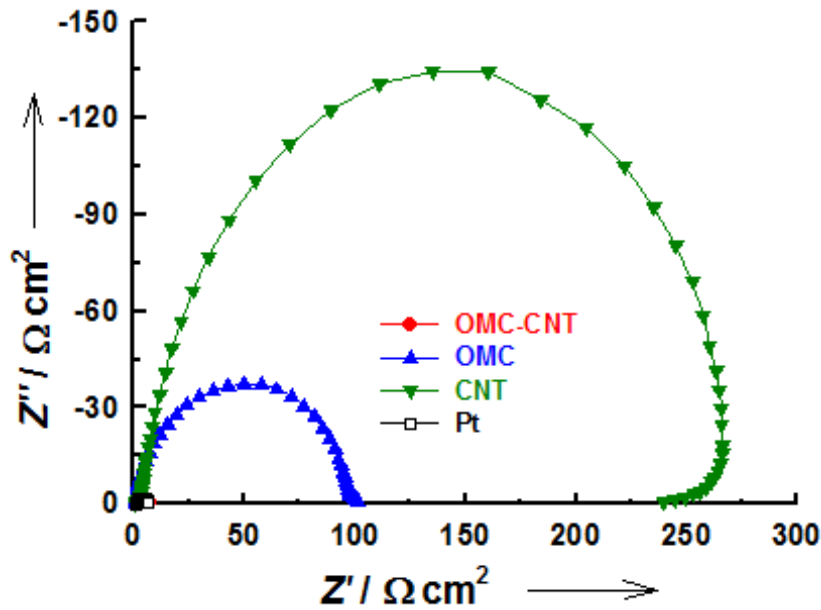
Figure 4-8. Nyquist plots of devices with OMC–CNT, OMC, and Pt under the 1 SUN condition.

The catalytic activities of the samples were investigated by cyclic voltammetry (CV) with a scan rate of 100 mVs^{-1}. As shown in Figure 4-9., the CEs based on the OMC–CNT nanocomposites and Pt showed very similar shapes in terms of redox peak positions and current densities. The reduction/oxidation peaks for the Pt and the OMC–CNT nanocomposites appeared at -0.163 V/0.242 V and -0.152 V/0.262 V, respectively. However, when the CE was replaced with the OMC- or CNT- only electrode, the peaks were shifted to -0.203 V/0.403 V or -1.560 V/0.423 V. The shift might also be due to resistance between either the carbons themselves or between the carbons and the FTO substrate. Comparing the current densities of the samples, the OMC–CNT nanocomposites and Pt exhibited higher values than the OMC or CNT, suggesting their higher intrinsic catalytic activity for iodine reduction.
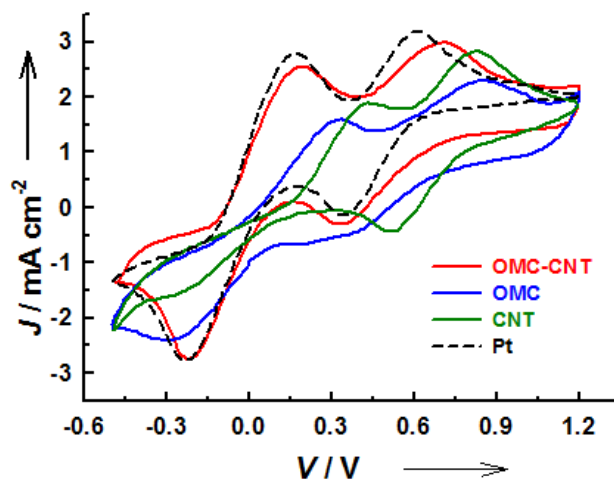
Figure 4-9. Cyclic voltammograms for each sample on FTO glass

We next examined the long-term stability of DSSCs that is critical for their practical application. The efficiencies of cells based on the OMC–CNT nanocomposites, OMC, and Pt-based CEs were monitored for 30 days. (Figure 4-10.)
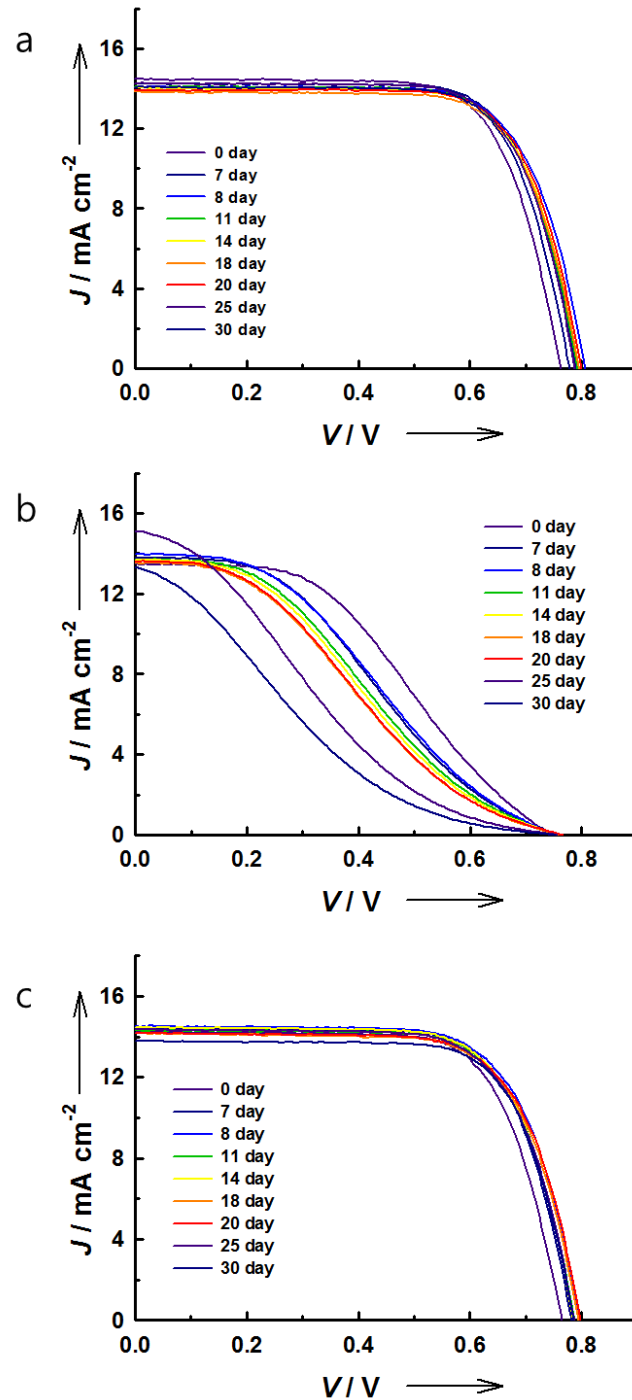
Figure 4-10. *J-V* characteristics of the DSSC employing (a) OMC–CNT (b) OMC (c) Pt based CE in a long-term stability test.

Figure 4-11.a displays the changes of DSSC efficiencies with time. While the Pt- and the OMC–CNT-based cells were quite stable for 30 days, the performance of the OMC-based cell was drastically declined after only 5 days. This drop was mainly due to the reduction of catalytic ability of the OMC. To confirm this, the changes of J-V curves (Figure 4-10.b) and EIS (Figure 4-11.b) of the OMC-based cell with time were investigated. Although the changes of V_{oc} and short circuit current (J_{sc}) were not noticeable with the aging of the cell, a drastic change was observed with the drop of FF, which goes parallel with the efficiency decrease. This change of FF may originate from the resistance change, which was investigated by EIS analysis. As shown in Figure 4-11.b, the first arc that corresponds to the resistance at an interface between the CE and an electrolyte drastically increased during aging. The weak interaction between the OMC and either an FTO substrate or the OMC themselves may cause disengagement of the OMC to the electrolyte. In contrast, in the OMC–CNT nanocomposites, CNTs could combine OMC islands and FTO substrate, which is suitable for long period applications without noticeable wrecks.
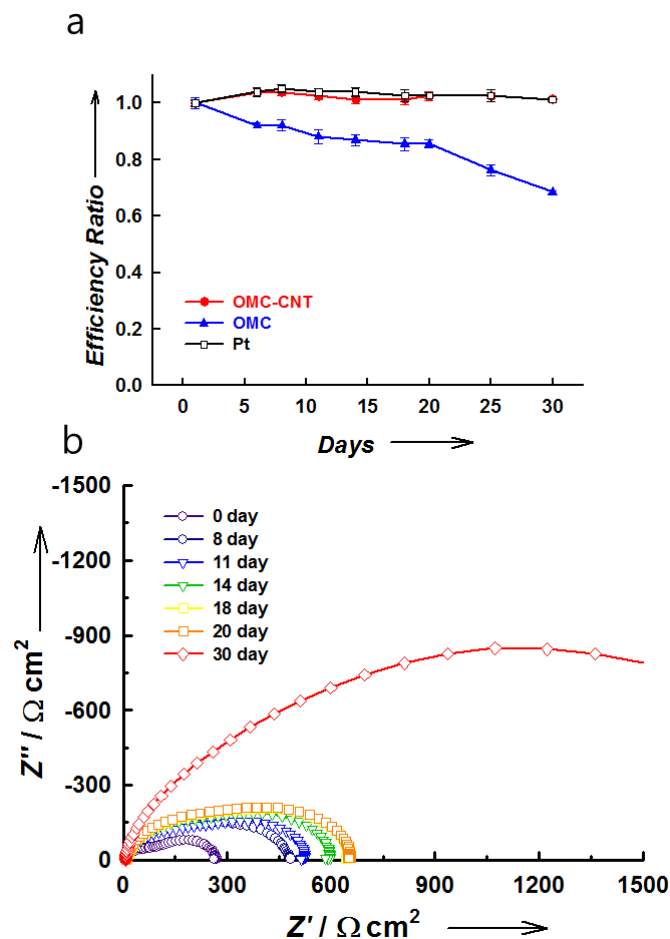
Figure 4-11. (a) Long-term stability for DSSCs with OMC-CNT, OMC, and Pt as counter electrode for 30 days. (b) Nyquist plots of the device with OMC-based CE in a in a long-term stability test.under the 1SUN condition

4.4. Conclusion

we have reported a new, medusa-shaped nanocomposite, OMC–CNT, where the primary particles of the OMCs are interconnected via the CNTs. In particular, the OMC–CNT nanocomposites represents the first example of simultaneous one-step formation of OMCs and CNTs from a single precursor. When applied as the CE for DSSCs, the OMC–CNT-based cell showed an excellent cell efficiency that rivals cells with a Pt-based CE and is superior to cells based on the OMC and CNTs, which was primarily attributed to its remarkably enhanced electrical conductivity as well as its intrinsic catalytic activity. Furthermore, the DSSC employing the CE with the OMC–CNT nanocomposites exhibited a remarkable stability as the initial catalytic activity was maintained after a long term (1 month) test, whereas the cell based on the OMC-based CE suffered a significant activity loss (70% of the initial value). This work provides an intriguing way of structurally designing a low-cost, Pt-free, high-performance CE material for DSSCs. Given their advantageous structural and electrical properties, the extensive applications of the OMC–CNT nanocomposites as advanced electrode materials for fuel cells and Li-ion batteries are envisaged and currently underway.

Chapter 5. Graphene oxide for Counter electrode of DSC.

5.1. Introduction

A typical DSSC consists of a dye-sensitized mesoscopic TiO_2 photoanode, a Pt/fluorinated tin oxide (FTO) counter electrode, and an electrolyte with an I_3^-/I^- redox couple. The operation of the DSSC is initiated by the light-induced oxidation of dye molecules. The electrons from the dyes gather at the substrate and enter an outer load toward the Pt counter electrode. The oxidized dye molecules accept electrons from iodide ions in the electrolyte, and the resulting triiodide ions are reduced back to iodide ions at the counter electrode. One important challenge in the practical development of DSSCs is to substitute the Pt counter electrode while maintaining high conversion efficiency, as Pt is a rare and expensive material, which may inhibit large-scale fabrication. To replace Pt as the counter electrode requires materials with high charge exchange current during the redox reaction (high electro catalytic activity), resistance to corrosive electrolytes containing iodide, and transparency. Thus far, several studies have sought possible substitutes, with CoS and carbonaceous materials such as carbon black and carbon nanotubes showing some but limited potential.[108-111] Most electrodes based on carbon exhibit low charge exchange current and therefore require thick coating to achieve high surface area. This however results in opaque DSSCs. For example, while DSSC with the Pt NP/MWNT counter electrode showed higher short-circuit current density and power-conversion efficiency due to higher catalytic ability for I_3^- reduction by large electrochemical active surface area than DSSC with bare Pt counter electrode, transmittance of Pt NP/MWNT counter electrode was 40-50%. Recently DSSCs with graphene counter electrodes have been shown to exhibit relatively high efficiency (a maximum of 90% of a conventional DSSC with a Pt counter electrode).[98, 112-113]

Herein we describe hybrid films of partially reduced graphene oxide (rGO)/metal nanoparticles. Thin films of reduced GO decorated by metal nanoparticles were fabricated via highly controllable layer-by-layer (LbL) assembly. Specifically, rGO/metal films consisting of Au, Ni, and Pt nanoparticles, for comparison, were fabricated. It is particularly interesting that Au and Ni in the form of nanoparticles on top of rGO can be utilized as a counter electrode since they are easily etched away by iodide/tri-iodide electrolyte. These metals have not been used in DSSC devices because they are not electrochemically stable in the presence of the iodide/tri-iodide electrolyte. Therefore, the use of metals like Au and Ni in the iodide electrolyte system is an important issue in terms of scientific discovery as well as economical fabrication of DSSCs. Our results demonstrate that integration of a variety of metal nanoparticles with rGO appears to increase their chemical stability in the presence of the electrolyte, which allows them to be used as an effective counter electrode material in DSSCs. We propose that, as a result of first-

principles calculations, the enhanced stability of Au nanoparticles on rGO can be attributed to strong anchoring of Au nanoparticles in the presence of carboxyl and hydroxyl functional groups that help desorption of iodides on Au surfaces.

5.2. Experimental

5.2.1. Preparation of negatively and positively charged GO

Graphite oxide was synthesized by the modified Hummers method and exfoliated to give a brown dispersion of graphene oxide under ultrasonication. The resulting graphene oxide (GO) was negatively charged over a wide pH range, as the GO sheet contains chemical functional groups such as carboxylic acids. Positively charged GO was synthesized using N-ethyl-N'-(3-dimethyl aminopropyl) carbodiimidemethiodide (EDC, 98%, Alfa Aesar) and ethylenediamine (99%, Sigma-Aldrich). Negatively charged GO suspension (50 mL) was combined with EDC (600 mg) and ethylenediamine (4 mL) and stirred for 4 h, and afterwards the mixture solution was dialyzed for 24 h to remove EDC and ethylenediamine. The MWCO of the dialysis tubing (Spectra/Por dialysis membrane) was 12~14 kD. A dark brown positively charged GO suspension was obtained.

5.2.2. Preparation of rGO/Pt and rGO/Au hybrid films on FTO for the counter electrodes

Fluorine-doped tin oxide FTO substrates (Pilkington TEC Glass-TEC 8) were cleaned with oxygen plasma to create a hydrophilic surface. Positively charged GO solution (0.5 mg/mL) at pH 4 was dropped onto the FTO substrate and loaded onto a spin coater (ACE-200, Dong Ah Tech), held there for 2 min after which it was spun at 3,000 rpm for 30 seconds. As a rinsing step, DI water at the same pH was dropped onto the substrate coated with positively charged GO held for 2 min and spun at 3,000 rpm for 30 seconds. Next, negatively charged GO solution (0.5 mg/mL) at pH of 10 was spin-coated using the same procedure, and was followed by a rinsing step. We then obtained one bilayer of a GO sheet. This procedure can be repeated to obtain multiple bilayers of GO sheets. The substrate was then dipped into $AuCl_3$ (25 mM) or H_2PtCl_6 (25 mM) aqueous solution. After 30 minutes, the substrate was dried with nitrogen gas. The as-prepared samples were thermally annealed at 550 ^{o}C in a vacuum for 30 min to partially reduce the GO and enhance the electrical conductivity.

5.2.3. DSC fabrication:

FTO glass substrates were washed in a detergent solution, DI water, an ethanol-acetone mixture solution (v/v=1/1), and 2-propanol in an ultrasonic bath for 5 min, in turn, and then treated by a UV-O$_3$ system for 15 min. The cleaned FTO glasses were then immersed in a 40 mM aqueous solution of TiCl$_4$

at 80 ^{o}C for 30 min and rinsed with DI water and an ethanol-acetonitrile mixture solution (v/v=1/1). Nanocrystalline TiO$_2$ paste (20 nm, ENB-Korea) was coated onto FTO glass using a doctor blade. The TiO$_2$-coated FTO glasses were aged at 60 ^{o}C for 1 h and annealed at 500 ^{o}C for 1 h to create a TiO$_2$ film with a thickness of 12 μm. The nanocrystalline TiO$_2$ paste (500 nm, ENB-Korea) was coated onto the TiO$_2$ film, aged at 60 ^{o}C for 1 h, and annealed at 500 ^{o}C for 1 h to create a TiO$_2$ film with total thickness of 16 μm. The TiO$_2$ substrate was then treated with 20 mM of an aqueous solution of TiCl$_4$ at 80 ^{o}C for 30 min and rinsed with DI water and an ethanol-acetonitrile mixture solution (v/v=1/1). The substrate was heated to 500 ^{o}C, cooled to 80 ^{o}C, and immediately immersed in 0.5 mM (Bu4N)$_2$[Ru(dcbpyH)$_2$(NCS)$_2$] (N719) in a mixed solvent of acetonitrile and tert-butanol (v/v=1/1). The substrate in the N719 solution was then maintained at room temperature for 20 h. A 50 μm-thick Surlyn film (DuPont) was placed over the prepared dye-coated TiO$_2$ electrode and the counter electrode was subsequently placed. Sealing of the cell was achieved by pressing the electrodes at 120 ^{o}C for 5 sec. Electrolyte was added to the system, and a final sealing completed the fabrication of the cell. The composition of the electrolyte was 0.6 M 1-hexyl-2,3-dimethyl-imidazolium iodide, 0.1 M lithium iodide, 0.05 M iodine, and 0.5 M 4-tert-butylpyridine in acetonitrile.

5.2.4. Characterization:

Photocurrent-voltage (J-V) curves of DSSCs were obtained by current-voltage characteristics measurements (Keithley, Digital Source Meter, model 2400) under AM 1.5G light of 100 mW/cm^2 (Newport, ORIEL-Sol-3A). The symmetrical sandwich cell is as close as possible to the actual situation in DSSC. It was fabricated from two identical FTO substrates (or GO/metal-coated FTO substrates) which were separated by 70μm thick Surlyn tape (DuPont) as a spacer. The cell was filled with acetonitrile electrolyte with 0.1 M lithium iodide, 0.01 M iodine, and 1 M tetrabutylammonium perchlorate. The surface morphologies of the rGO and rGO/metal hybrid films were investigated by scanning electron microscopy (FEI, Nova Nanosem 230). The films were also characterized by x-ray photoelectron spectroscopy (Thermo Fisher, K-alpha). The thickness of the rGO thin films was measured by ellipsometry (J. A. Woollam Co. Inc., EC-400 and M-2000V). The transmittance of the GO and GO/metal hybrid films was characterized by UV/VIS spectroscopy (VARIAN, Cary 5000).

5.3. Result & discussion

Figure 5-1. shows rGO/metal nanoparticle hybrid films as counter electrodes on FTO anode which can be incorporated in DSSC. The detailed description of the GO preparation, thin film deposition, and device fabrication are given in the experimental section. Briefly, for uniform deposition of GO thin

films, we initially synthesized negatively and positively charged GO, which allowed the use of Layer-by-Layer (LbL) assembly of the oppositely charged sheets. Given that LbL assembly affords precise control of the thickness of GO thin films, an optimized film thickness was investigated by measuring the efficiency of DSSCs with different number of GO bilayers. (Table 5-1. and Figure 5-2.) Based on these initial results, we selected 2 bilayers of GO as the optimal film thickness. (The thickness of the film was around 6.5 ± 0.3 nm when 2 bilayers of GO were coated onto a flat Si wafer because the thickness could not measured on rough FTO substrate).
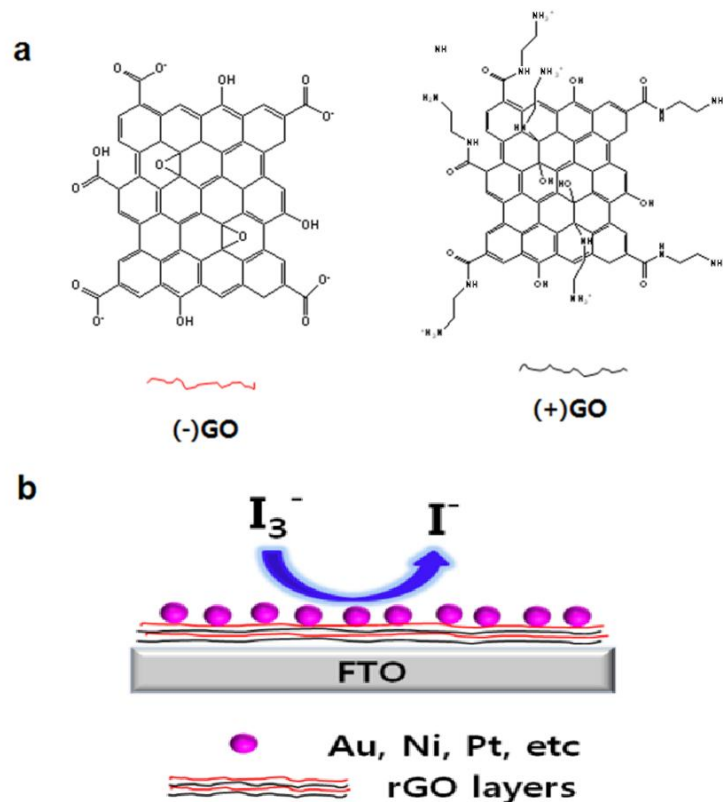
Figure 5-1. a) Schematic showing molecular structures of negatively charged (-) and positively charged (+) GO. (b) Schematic showing metal nanoparticles on reduced graphene oxide (rGO) 2 bilayers.
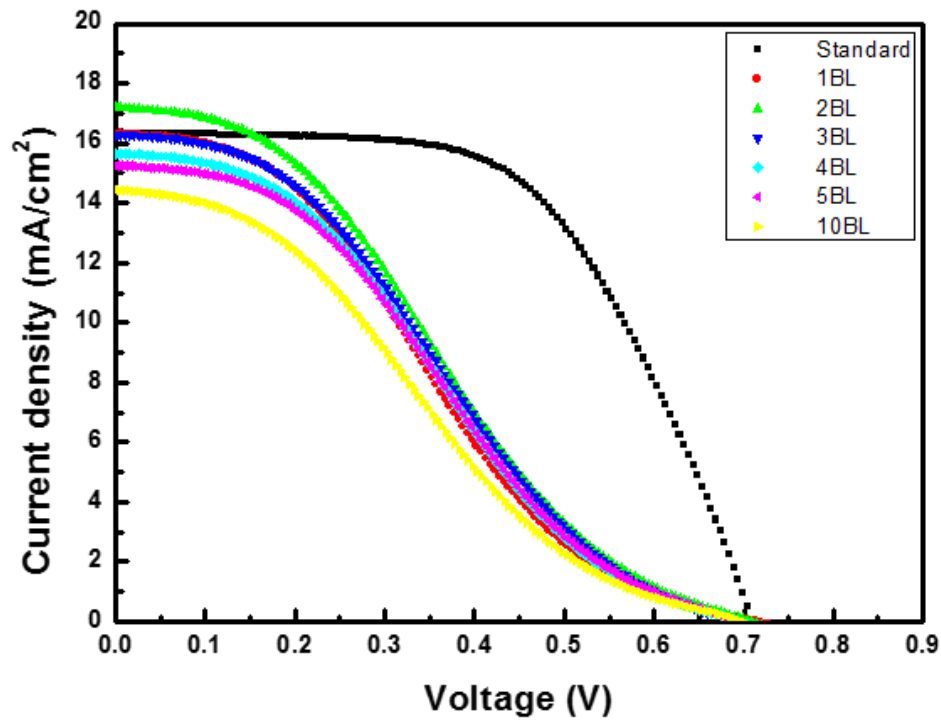
Figure 5-2. J-*V* curves of DSSCs with different rGO bilayers.

Counter electrode	E_{ff} (%)	V_{oc} (V)	J_{sc} (mA/cm^2)	FF	Percentage(%)
Pt	6.8	0.7	16.2	0.571	100
1 bilayer of rGO	3.2	0.72	16.2	0.278	49
2 bilayers of rGO	3.7	0.71	17.2	0.292	57
3 bilayers of rGO	3.3	0.69	16.1	0.301	50
4 bilayers of rGO	3.2	0.69	15.8	0.305	49
5 bilayers of rGO	3.2	0.69	15.3	0.306	49
10 bilayers of rGO	2.8	0.7	14.0	0.291	43

Table 5-1. Photovoltaic characteristics of DSSCs with different number of rGO bilayers.

In the subsequent step, a metal layer was coated on 2 bilayers of GO by immersing the GO thin film

on FTO into a solution with metal precursors and heating to 550 ºC. The formation of metal nanoparticles on rGO sheets is well known.[113-116] The SEM images of (a) an uncoated FTO surface, (b) Pt thin film coated FTO (i.e the conventional counter electrode), (c) rGO/Pt-coated FTO, (d) and rGO/Au-coated FTO are shown in Figure 5-3. The Pt film on the rough FTO surface was found to be non-uniform while discrete, homogeneous nanoparticles are clearly visible in Figure 5-3. (c) and (d). The uniformity of the nanoparticles in 2(c) and 2(d) suggests that the binding of the metal nanoparticles is facilitated by GO. The thin rGO/metal nanoparticle hybrid films were transparent as indicated in insets of Figure 5-3. (a), (c), and (d), which show optical images of bare FTO, rGO/Pt on FTO, and rGO/Au on FTO, respectively. The rGO/Pt and rGO/Au nanoparticle films showed lower transmittance by 8.2 and 11.6 % at 550 nm, respectively, compared to FTO. (Optical images and transmittance of bare FTO, rGO on FTO, rGO/Pt on FTO, and rGO/Au on FTO are shown in Figure 5-4.)

Further analysis of the metal nanoparticles on the rGO surface was performed by X-ray Photoelectron Spectroscopy (XPS), the results of which are also shown in Figure 5-3.XPS revealed that the metal nanoparticles in Figure 5-3. (c) and (d) are reduced Pt and Au, respectively, as indicated by the two peaks of the Pt 4f core electrons that appear at 71.7 and 74.8 eV in Figure 5-3. (e) and by the two peaks of the Au 4f core electrons at 83.6 and 87.3 eV in Figure 5-3. (f). The C 1s binding energy peaks in rGO/Pt and rGO/Au hybrid films are shown on Figure 5-3. (g) and (h), respectively. The C 1s peaks after metal nanoparticle decoration are consistent with those of partially reduced GO.[117-121] That is, similar C 1s peak shape is observed in GO that has been reduced by thermal annealing at intermediate temperatures. In the partially reduced GO, substantial hydroxyl groups are expected to evolve during annealing but some will remain while the carboxyls at the edges are more robust and unlikely to leave at the modest annealing temperatures.
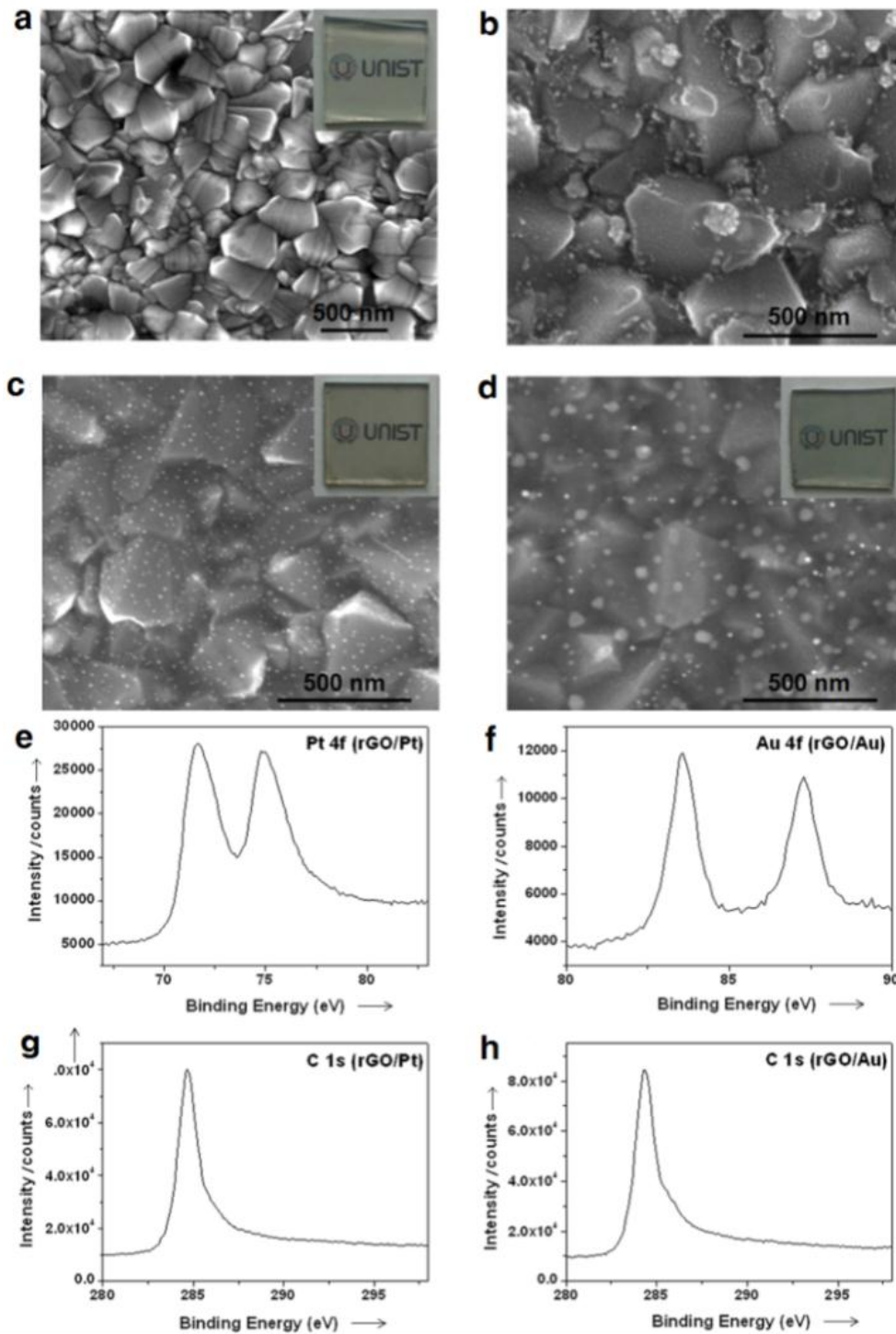
Figure 5-3. Characterization of the rGO/metal hybrid films. SEM image and optical image (inset) of (a) a bare FTO substrate, (b) Pt-coated FTO substrate, (c) rGO/Pt hybrid film, and (d) rGO/Au hybrid film on FTO, respectively. XPS spectrum for the binding energy of (e) the Pt 4f core electron in the rGO/Pt hybrid film, (f) the Au 4f core electron in the rGO/Au hybrid film, (g) the C 1s core electron in the rGO/Pt hybrid film, (h) the C 1s core electron in the rGO/Au hybrid film, respectively
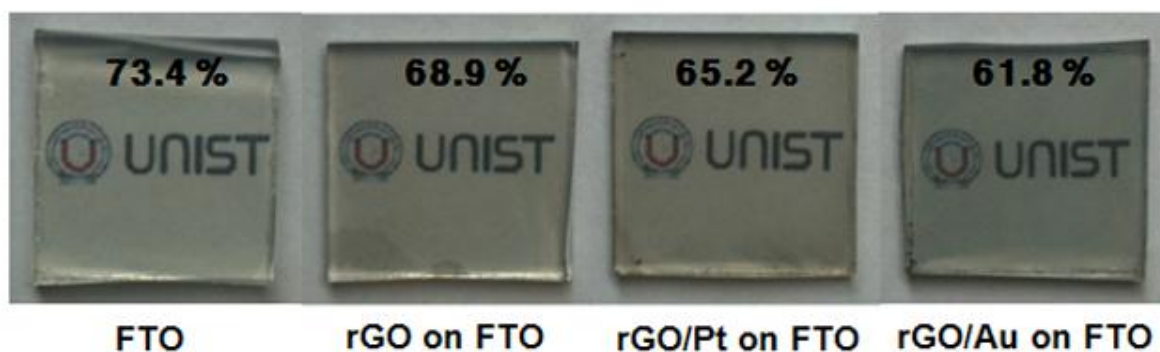
Figure 5-4. Optical images of bare FTO, rGO on FTO, rGO/Pt on FTO, and rGO/Au on FTO. The rGO/Pt and rGO/Au films showed lower transmittance by only 8.2 and 11.6 % at 550 nm, respectively, compared to FTO

It is important to note the significance of successful implementation of Au nanoparticles as DSSC counter electrodes with rGO. Thus far, Au has not been utilized as a counter electrode material because it is readily corroded by the iodide/tri-iodide electrolyte. Thus, it is interesting that Au in the form of a hybrid film with rGO can be used as a counter electrode without degradation. That is, the efficiency of the DSSC with rGO/Au nanoparticle hybrid thin film counter electrode remained at this level for 1 month without a significant decrease. (Figure 5-5.) (See Table 5-1. for the performance of DSSC) As a control experiment, a DSSC with pristine Au as the counter electrode showed efficiency of around 0.04 % (Figure 5-6. and Table 5-2.)
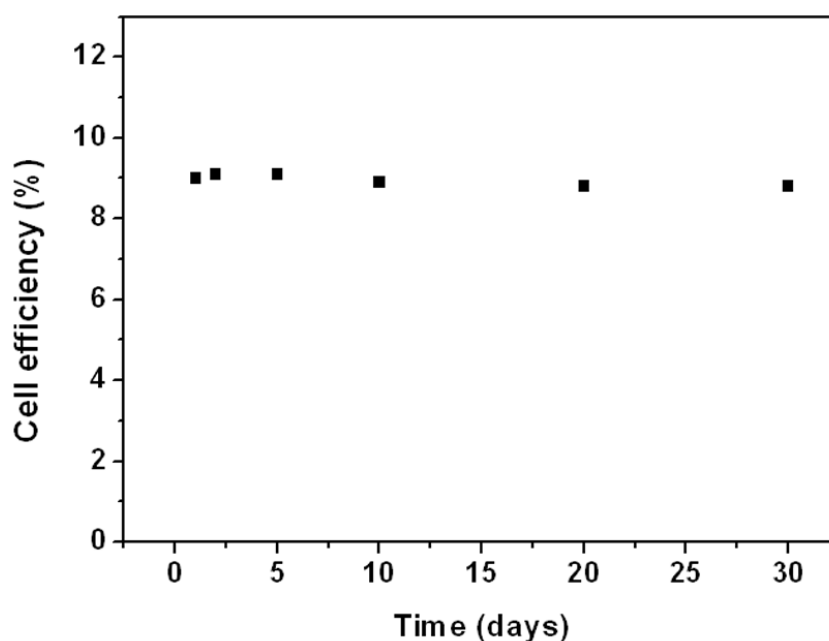
Figure 5-5. The change of cell efficiency in DSSC with the rGO/Au hybrid film as a counter electrode. The cell efficiency after 30 days was not measured because of a leakage of the electrolyte in the cell
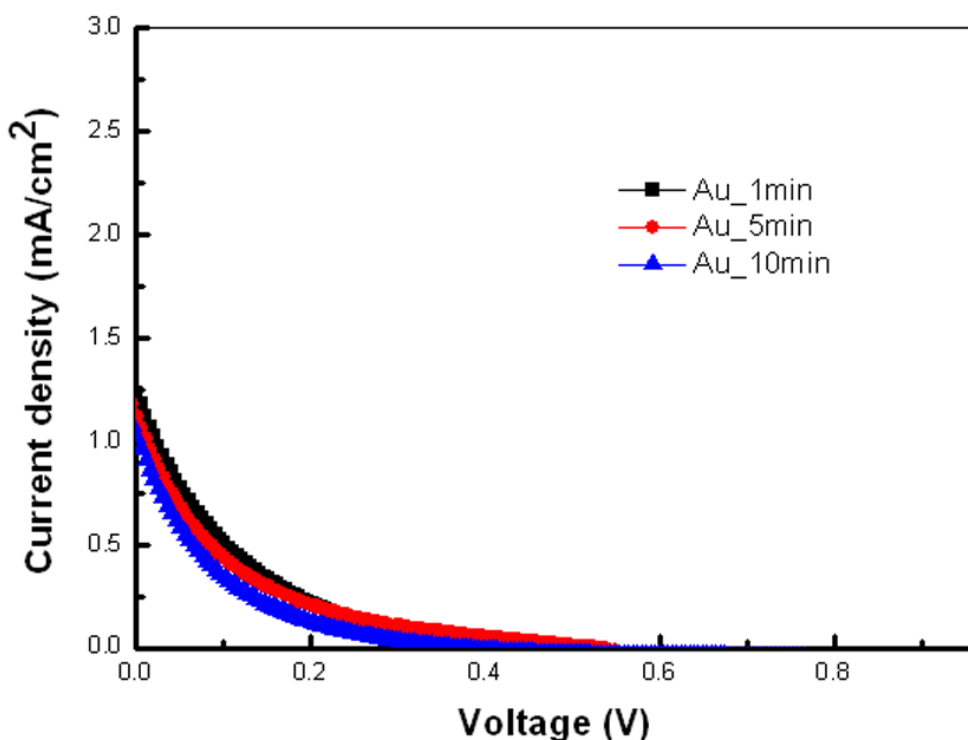
Figure 5-6. Photovoltaic characteristics and *J-V* curves of DSSC with a Au counter electrode as a function of time.

Time	E$_{ff}$(%)	*V$_{oc}$*(V)	*J$_{sc}$*(mA/cm^2)	FF
1 min	0.052	0.408	1.2	0.103
5 min	0.045	0.523	1.1	0.076
10 min	0.034	0.372	1.0	0.091

Table 5-2. Photovoltaic characteristics and *J-V* curves of DSSC with a Au counter electrode as a function of time.

It was confirmed from SEM images that Au in the rGO/Au nanoparticle hybrid film did not corrode after the operation of the DSSC (Figure 5-7.a). The stability of the rGO/Au nanoparticle films in DSSCs is consistent with the results of Kou et al. who attributed the stability of Pt nanoparticles in oxygen reduction fuel cells to strong interactions between Pt and defects/functional groups on graphene using density functional theory (DFT) calculations. Similar effect is also present in our cases: we performed first-principles computations and found that Au nanoparticles strongly anchored onto defect sites of graphene are more stable. (See the result later) The stability of the rGO/Au catalyst was also apparent in the repeated CV scans of a three-electrode system (Figure 5-7.b), which did not show any change in

the reduction peaks of I_3^- after many scans, whereas the Au catalyst showed considerable changes with repeated CV scans.
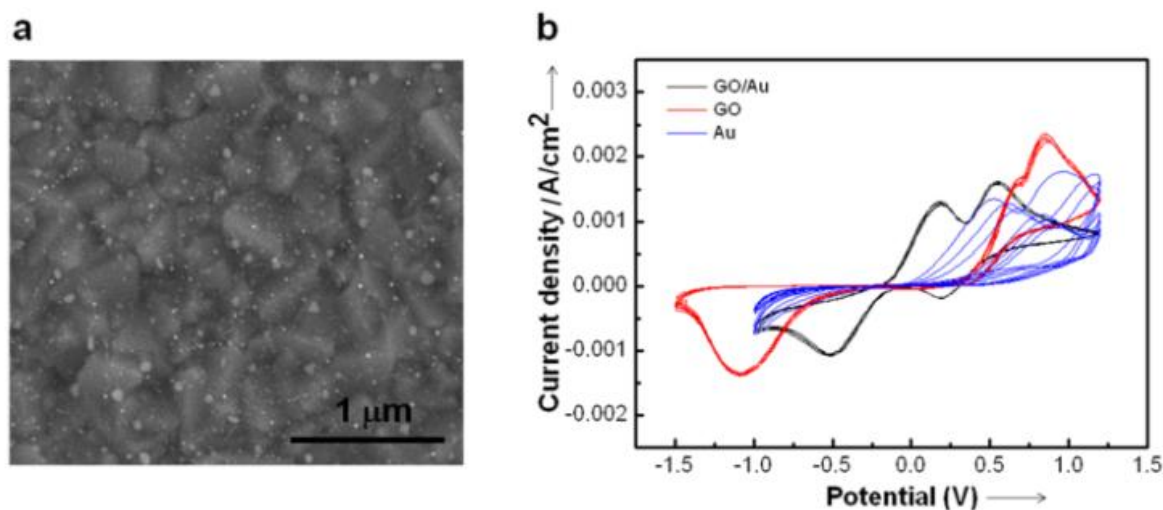
Figure 5-7. a. SEM image of the rGO/Au hybrid film after the operation of DSSC. b. Cyclic voltammograms of Au (blue), rGO (red), and rGO/Au film (black) at a scan rate of 100 mV/s in acetonitrile electrolyte with 0.1 M lithium iodide, 0.01 M iodine, and 1 M tetrabutylammonium perchlorate. An Ag/AgCl (Sat. KCl) reference electrode and a Pt counter electrode were used. The rGO/Au film did not show any change in the reduction peaks of I_3^- after many scans, whereas Au showed considerable changes.

The same phenomena were shown in C-V (current density *vs* potential) scans of a symmetrical sandwich cell, providing information about the performance and stability of the counter electrode (Figure 5-8.)
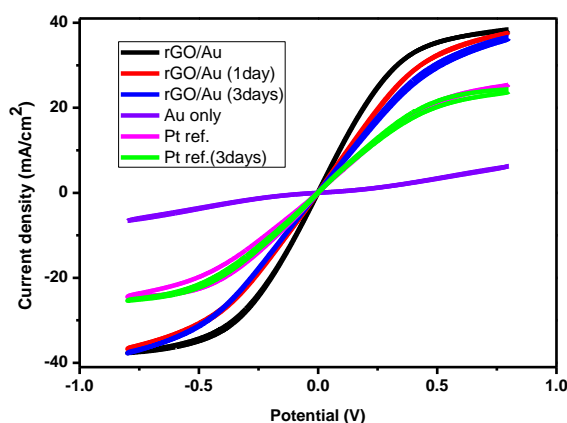
Figure 5-8. C-V of bare Au (violet), rGO/Au film (black, red, blue), and Pt (magenta, green) on FTO substrates at a scan rate of 100 mV/s in symmetrical sandwich cells with the same electrolyte as used in the actual DSSC devices. When bare Au electrode is employed, Au is easily etched away by high concentration of iodine, therefore, no noticeable current was observed.

These results indicate that the rGO/Au nanoparticle film is stable in the iodide/tri-iodide electrolyte while the pristine Au catalyst is corroded. Further, we investigated electrocatalytic activity of rGO/Au, rGO/Pt, and bare Pt to see if rGO/Au can be used for catalytic counter electrodes. In the electrochemical impedance spectroscopy (EIS) data on simplified sandwich cell with electrolyte concentrations equal to those used in DSSCs, we find that the first semicircles for rGO/Au and rGO/Pt are smaller than that for bare Pt (See Figure 5-9.), suggesting that rGO/Au and rGO/Pt are indeed electrocatalytically more active than bare Pt. The EIS results are consistent with the C-V results in Figure 5-8. that the charge transfer in rGO/Au electrodes is substantially better than that in bare Au or Pt electrode.
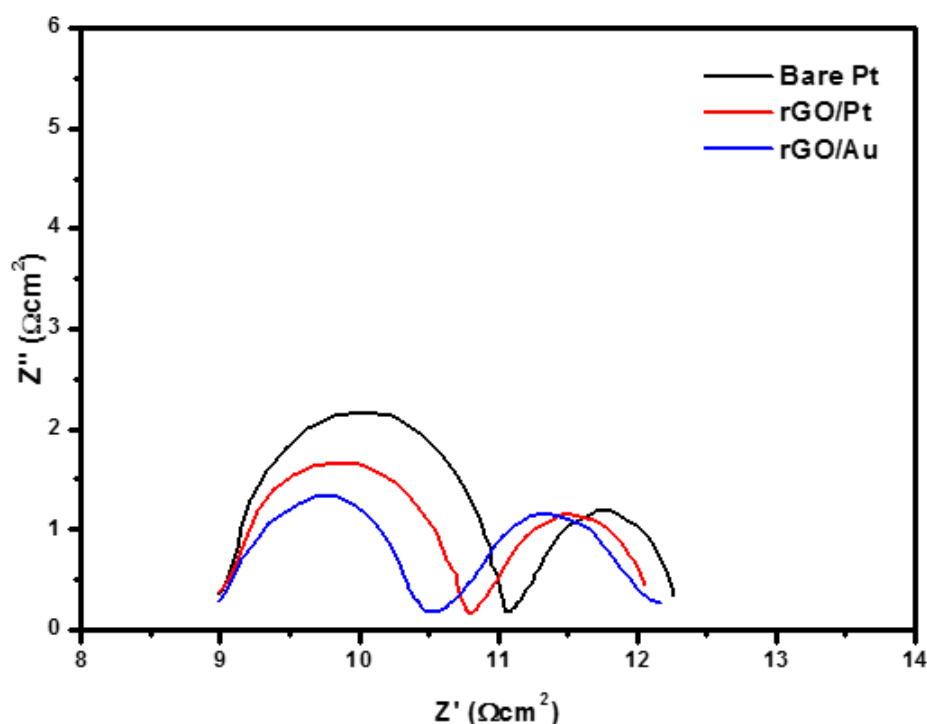
Figure 5-9. The impedance spectra of Pt, rGO/Pt, and rGO/Au measured using symmetric sandwich cells with the same electrolyte as used in the actual DSSC devices (acetonitrile electrolyte with 0.6 M 1-hexyl-2,3-dimethyl-imidazolium iodide, 0.1 M lithium iodide, 0.05 M iodine, and 0.5 M 4-*tert*-butylpyridine). The equivalent circuit describing the EIS data is provided and the resulting fitting results are summarized in the table

To investigate the microscopic origin of the observed electrochemical stability of rGO/Au nanoparticle hybrid counter electrodes, we carried out first-principles calculations. The electronic ground states were calculated within the framework of the density functional theory (DFT).[122-124] As a result of the computational study, we identified that two mechanisms can contribute to the stabilization of Au nanoparticles on rGO. The strongly adsorbed Au nanoparticles onto defective sites of graphene

are more resistive against the geometrical reconstructions upon adsorption/desorption of iodide. As shown in Figure 5-10. (a) and (b), Au_{13} particle chemically anchored on a graphene defect site preserves its shape upon adsorption of tri-iodide. On the contrary, the bare Au_{13} particles spontaneously transforms to an under-coordinated geometry, indicating breaking of Au-Au bonds (Figure 5-10. (c)). Relaxation of the surface strain energy of the Au nanoparticle can be obtained by such strong anchoring of the Au nanoparticles. The rGO surface is expected to have many imperfections compared with perfect graphene, providing greater chance of strong interaction with Au nanoparticles.[125]
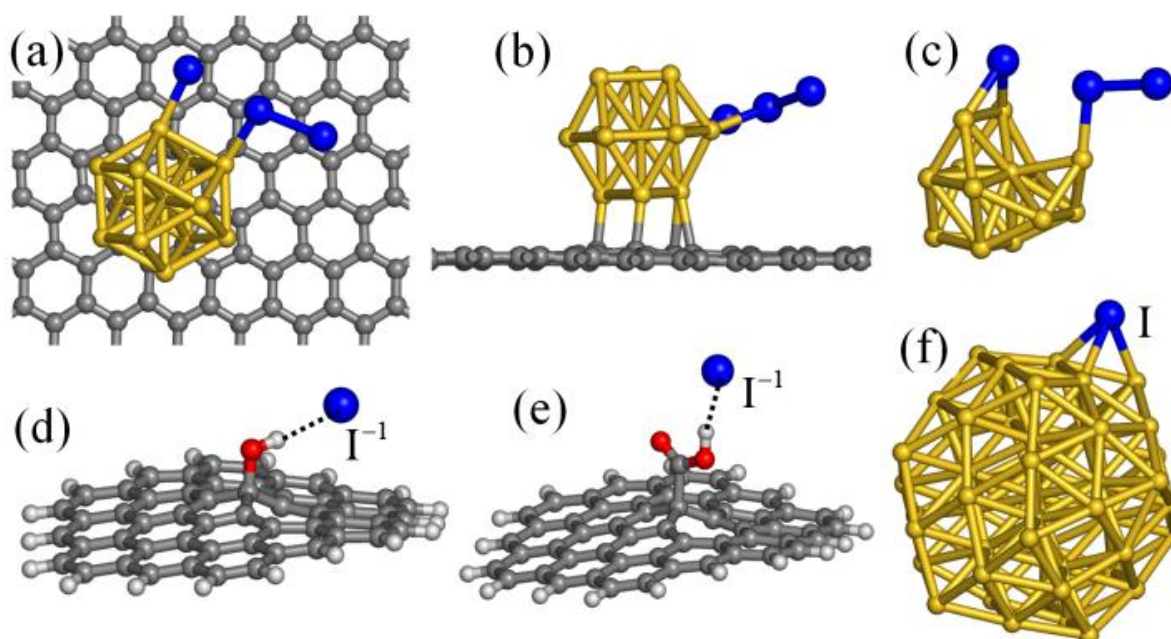
Figure 5-10. The first-principles computation results for iodine and iodide adsorptions onto Au nanoparticles and rGO. (a) The optimized geometry of I_3^- onto Au_{13} anchored onto defective graphene. (b) Side view of (a). (c) The same geometry without graphene plane. (d) and (e), The adsorption geometries of I^- onto OH and COOH groups on graphene fragment. (f) The same geometry of iodine onto Au_{55} nanoparticle. Grey, red, white, yellow, and blue balls represent carbon, oxygen, hydrogen, gold, and iodine atoms, respectively.

As an independent mechanism, the presence of various functional groups on rGO (for example, OH or COOH) is thought to help desorption of iodides from Au surface. In order to model this effect, we positioned OH and COOH groups on graphene fragments, as shown in Figure 5-10. (d) and (e). On Au surfaces, the tri-iodide spontaneously dissociates and strongly bonded to the Au surface as a form of almost neutral iodine, as depicted in Figure 5-10. (f). The binding strength is quite strong (2.0 eV) but iodine is mobile within the Au surface after dissociation from tri-iodide. On the other hand, as a result of our DFT calculation, the iodide is attached to the OH and COOH groups with reasonable binding strength (about 0.7 eV), as denoted in Figure 5-10. (d) and (e). Therefore, the presence of such terminal groups on rGO provide a stepping-stone that promotes hoping of iodine from Au surfaces onto rGO

that eventually helps the desorption as iodide (I^-). This can alleviate the etching process of Au in the iodide/tri-iodide electrolyte. It is known that the etching process involves the formation gold iodides, like AuI_2^{-1}. The increased chance of hopping to neighboring rGO surfaces reduces the rate of formation of such anionic species, leading to an increased electrochemical stability of Au nanoparticles.

The rGO/metal hybrid films were successfully applied to catalytic counter electrodes in DSSCs. Table 5-1. summarizes average cell efficiencies of DSSCs with rGO/Pt, rGO/Au, and rGO/Ni nanoparticle thin films as counter electrode materials. (See Figure 5-11.) Interestingly, the cell efficiencies of the rGO/Au and rGO/Ni nanoparticle counter electrodes are comparable or slightly higher compared to that of the conventional Pt counter electrode. It means that the rGO/Ni hybrid film is stable in the iodide/tri-iodide electrolyte system as the the rGO/Au hybrid film. The stability and the charge transfer of rGO/Ni in the iodide/tri-iodide electrolyte were proved by C-V curves in Figure 5-12.
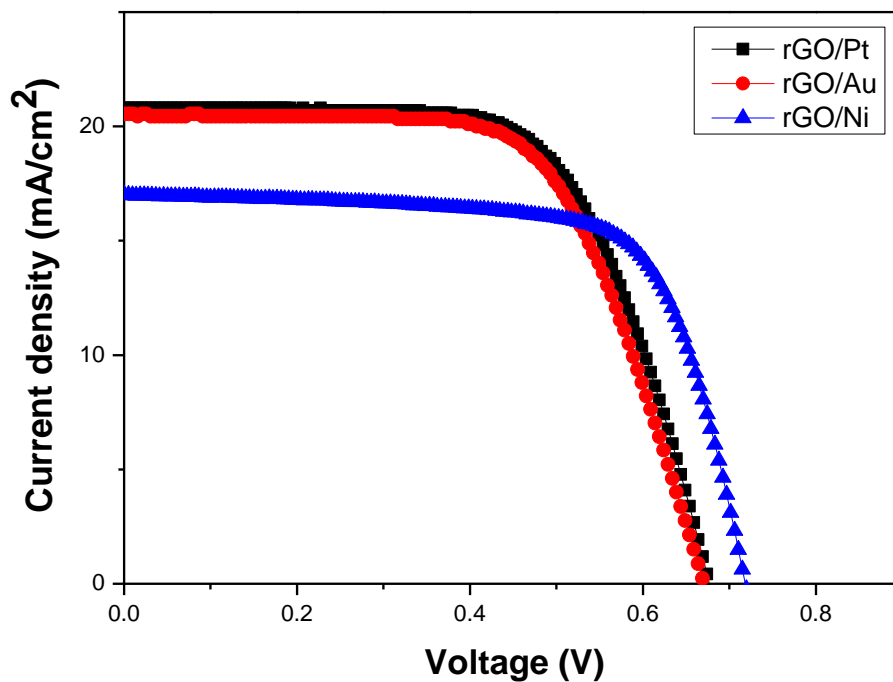
Figure 5-11. J-V curves of DSSCs with counter electrodes of rGO/Pt hybrid film, rGO/Au hybrid film, and rGO/Ni hybrid film.
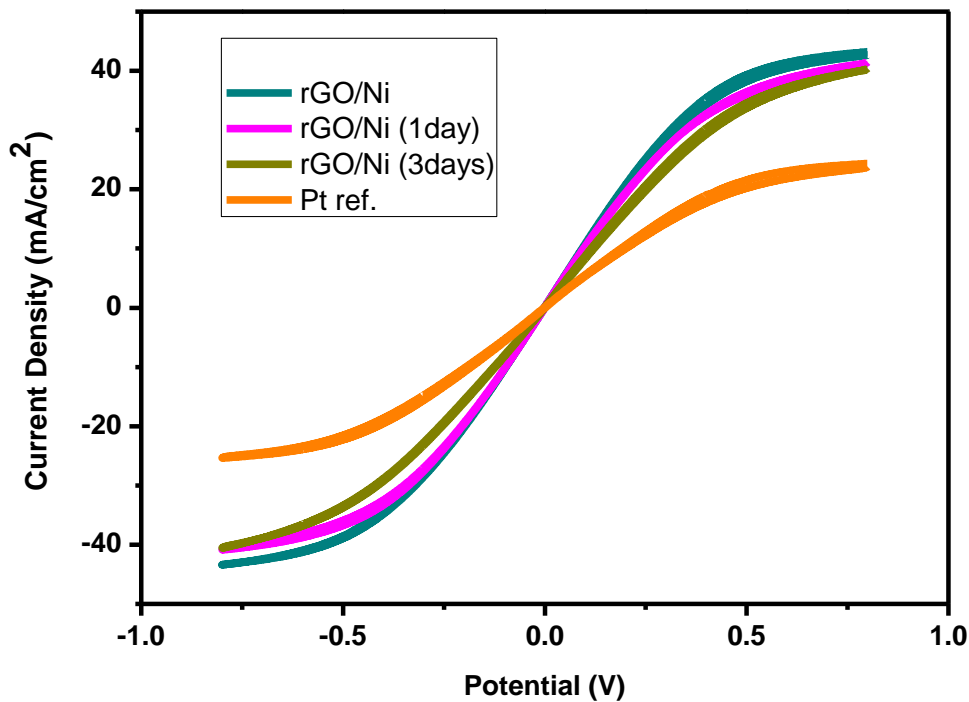
Figure 5-12. C-V of rGO/Ni film (cyan, pink, dark yellow) and Pt (orange) on FTO substrates at a scan rate of 100 mV/s in symmetrical sandwich cells with the same electrolyte as used in the actual DSSC devices. The rGO/Ni hybrid film shows quite steady current after a day.

5.4. Conclusion

Inexpensive and stable rGO/metal nanoparticle hybrid films for counter electrodes in DSSCs as Pt replacement counter electrodes are described. The enhanced electrochemical stability of the Au nanoparticles on rGO was attributed to the unique combination of the presence of defects as well as hydroxyl and carboxyl functional groups. Furthermore, rGO/Au and rGO/Ni hybrid films were demonstrated to be effective hybrid counter electrode materials in DSSCs. The results reported here could lead to the elimination of Pt from DSSCs, which could lead to their widespread use.

Chapter 6. A novel dye coating method for DSC

6.1. Introduction

In DSSC production, the most time consuming process is coating dye on working electrodes. Currently, one of the most reliable dyes for commercialization is an N719 dye, which has been considered as a standard reference for many DSSC systems for a long time.[126-127] Ru-based N719 dye adsorption on a photo anode takes a long time; over 6 h at 60 ^{o}C, or overnight at a room temperature in solvents such as ethanol, tertiary-butyl alcohol (TBA). According to a few reports, 5−10 min are enough to coat dyes up to 83−93% of their maximum amounts by 5−20 mM concentration of N719.[128-129] For a comparable efficiency to fully covered working electrode, still more than 10 min are required. Another recent report shows the effect of sensitizer adsorption temperature on the DSSC performance. In the paper, the best performance was observed when C101 dye molecules were coated at 4 ^{o}C for 14 h.[130] Here, in this article, we report a new method to shorten dyecoating time, down to 3 min by controlling dye coating temperatur eand concentration in alcohol solvents. Currently, an ethanol or a TBA/acetonitrile mixture is the most common solvent for coating dyes, but their low boiling point limits temperature controls over 90 ^{o}C. Although there are many candidate solvents applicable to N719 coating at high temperature, we chose alcohol series because of a few reasons. Firstly, they are advantageous as solvents due to low cost and low toxicity. Secondly, a few alcohols such as ethanol and TBA are already proved as good solvents for dye coating with good solubility. Thirdly, various alcohols including mono-/di- /tri-/alcohols with different chain lengths are available for specific characteristics such as viscosity and boiling points.

6.2. Experimental

6.2.1. Preparation of TiO$_2$ photo-anodes

The TiO$_2$ paste (ENB Korea, 20 nm) was coated on the F-doped SnO$_2$ conducting glass (FTO, TEC 8, 2.3 mm, Pilkington) using thedoctor blading method. The resulting layer was sintered at 500 ^{o}C for 2 h in a muffle furnace. The thickness of the main active layer was12 μm (±0.5 μm) without a scattering layer. Dye solution was prepared by mixing N719 with various alcohols (from Aldrich). The concentration and reaction time are varied as mentioned in the main article. Before applying dye solution on photo-anodes, the anodes were placed on a hot plate which is set at specific temperatures. Dye solution was also warmed close to hot plate temperatures right before the application. In order to wash out the residual dye solution in porous TiO$_2$ working electrode, the electrodes were soaked in the

lukewarm ($\sim$40 °C) ethanol for 5 min with gentle disturbance.

6.2.2. Fabrication of DSSCs

10 mM hydrogen hexachloroplatinate (IV) hydrate (99.9%, Aldrich) in 2-propanol was placed on transparent FTO glass. After eat treatment at 450 °C for 2 h, the counter electrode was assembled ith the dye-adsorbed TiO_2 electrode. 25 μm of Surlyn as used to seal the sandwiched electrodes, and heating was aplied. Finally, the internal space was filled with the electrolytes through small holes, and then the holes were sealed by Surlyn and coverglass. The electrolyte composite is 0.5 M 1-hexyl-2,3-dimethyl-imidazolium iodide, 0.05 M lithium iodide, 0.02 M iodine, and 0.5 M 4-tert-butylpyridine in acetonitrile.

6.2.3. Characterizations

The photovoltaic properties of the prepared DSSCs were measured by using a computer-controlled digital source meter (Model 2400, keithley) and a solar simulator (AM 1.5G, 100 mWcm^{-2}, Sol3A, class AAA, Oriel) as a light source. The light intensity was adjusted with a reference Si cell (PV measurement co.). The electrochemical impedance spectroscopy (EIS) measurement has been carried out in the range of 10^{-1}~10^{6} Hz at 298 K by CH Instruments Electrochemical Workstation. The UV–Vis spectroscopy was obtained by Cary 5000 UV–Vis spectrometer (Varian), in the range of 200–900 nm. FT-IR characterization was carried out with 670-IR/620-IR Imaging (Varian). The photovoltaic performance has been characterized by V_{oc}, J_{sc}, fill factor (FF), and overall efficiency by J–V curve.

6.3. Results and discussion

When it comes to the kinetics of dye coating reactions, an increase of the concentration of reactants and a higher temperature induces the rate of the reaction. Currently, the major solvents for dye coating are acetonitrile (bp 82 °C) and ethanol (bp 78 °C). They are not suitable for controlling the concentration of the reactants with temperature at the same time. However, multi-alcohols, such as ethylene glycol, could relieve controlling a dye concentration at various temperatures. Due to their viscosity with proper hydrophilic characteristics, they could be applied to solvate the molecules even in higher concentrations. Besides, multi-alcohols have a higher boiling point than the conventional solvents, with the consequence that they could be reliable at high temperatures near 100 °C. To optimize the working electrode coloring performance, various diols and concentrations were applied in this experiment. All the dye coating was prepared at 100 °C for 3 min, unless mentioned otherwise. Since the boiling points of propanol and sec-butanol are lower than 100 °C, the experiments for these alcohols were run at 95 °C.

For diols, 1,2-ethanediol (ethylene glycol), 1,2-propanediol, 1,3-propanediol, and 1,6-hexanediol were employed. For triols, glycerol (1,2,3-propanetriol) was used. A reference cell was based on ethanol solvent. For comparison, normal alcohols and other alcohols such as n-propanol, n-butanol, and terpineol were also tested. Table 6-1 and 6-2. summarizes the cell performance depending on the cell preparation with different alcohols. When the chain length of normal alcohol is increased, the viscosity is also increasing with polarity decrease.

	Alcohol	Visc. (25°C)	BP	V_{oc}	J_{sc}	FF(%)	η
Mono-alcohol	propanol	1.939	97	0.75	15.47	70.9	7.72
	Butanol	2.599	117	0.72	14.82	70.8	7.5
	sec-butanol	3.248	99	0.72	14.62	71.6	7.48
	pentanol	3.425	138	0.71	14.18	67.8	6.78
	hexanol	4.596	158	0.76	10.3	75.7	5.25
Di-alcohol	Ethylene glycol(EG)	13.8	194	0.71	17.13	71	8.58
	EG (with scattering layer)	13.8	194	0.73	18.21	69	9.17
	1,2-propanediol	N/A	188	0.72	15.33	68	7.51
	1,3-propanediol	7.017	210-220	0.74	15.48	68	7.78
	1,6-hexanediol	1.066	250	0.74	12	69.9	6.2
Tri-alcohol	Glycerol	730	290	0.2	3	15	0.30

Table 6-1. Performances for DSSCs with working electrodes which were prepared in different alcohols. The concentration of N719 and reaction time are 20 mM and 3 min, respectively.

Temperature(°C)	20	30	40	50	60	70	80	90	100	110	120	130	140
EG	15.1	9.8	5.8	4.7	3.3	1.5	1.1	0.8	0.5	0.5	0.4	0.3	0.3
Glycerol	1410	612	284	142	81.3	50.6	31.9	21.3	14.8	10.5	7.8	6	4.7

Table 6-2. Viscosity changes for EG and glycerol depending on temperatures.

These terms may affect solubility (solvation) of N719, and delivery process to nano-porous TiO_2 surface. According to the table, the increase of chain length of n-alcohol decreased the cell efficiencies mainly due to current density lowering. For example, while the reference cell (ethanol) solvent showed a cell efficiency of 8.54% with current density over 17 mAcm^{-2}, the cell by hexanol solvent showed

only 5.25% with current density of 10 mAcm^{-2}. Multi-alcohols are more complicated. The best performance was observed from ethylene glycol. While 8.58% efficiency was observed from ethylene glycol, 7.8% and 6.2% efficiencies were observed when the chain length was increased to 1,3-propanediol and 1,6-hexanediol, respectively. When glycerol (triol) was used, the cell performance was only 0.3%. Since the viscosity of ethylene glycol is much lower than glycerol, ethylene glycol can easily penetrate the nano-porous TiO$_2$ electrode and deliver dye onto the surface more efficiently. Although Glycerol is well adsorbed on TiO$_2$ surface, it does not deliver dyes effectively down to the bottom layers of TiO$_2$. We would like to note that the viscosities of ethylene glycol and glycerol are 15.1 mPa s, and 1410 mPa s at 20 $_\circ$C, respectively. When the temperature is increased to 100 ^{o}C, the viscosities of ethylene glycol and glycerol are decreased. While the viscosity of ethylene glycol becomes close to that of ethyl alcohol (0.5 mPa·s), that of glycerol (15 mPa·s) is still a few ten times greater. This high viscosity may impede glycerol to efficiently move into nano-porous channel and deliver dye molecules to TiO$_2$ surface. In order to improve cell efficiency, the same method (by EG) was applied to a working electrode with a scattering layer. 500 nm sized TiO$_2$ was used for the scattering layer, and the thickness was controlled for about 5 μm. Since the thickness was changed, the maximum efficiency was obtained after 3.3 min coating, and the cell performance showed 9.2%.

The reaction time and the concentration of N719 dyes in ethylene glycol have been investigated simultaneously. Since controlling the reaction kinetics is important, higher concentrations were applied than in the conventional methods.
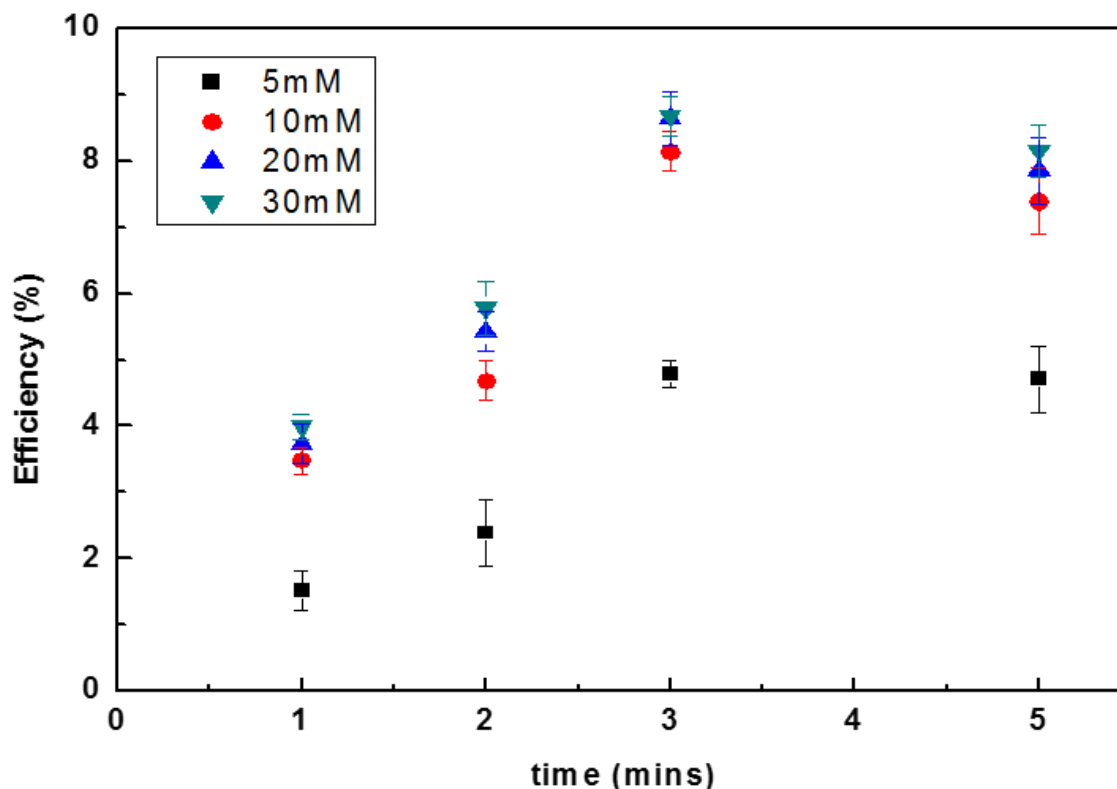
Figure 6-1. Cell performances of DSSCs depending on dye concentrations and coating time.

Figure 6-1. shows the cell performance depending on the reaction time and the concentration of dyes in ethylene glycol. When the concentration of dye is increased from 5 mM to 30 mM in ethylene glycol, the cell performance is improved. The maximum performance was obtained with the concentration of 20 mM or 30 mM and 3 min. Although 10 mM showed a comparable performance, their reproducibility was a bit lower than the experiments with 20–30 mM dye solutions. Therefore, dye can be fully adsorbed within 3 min by 20 mM solution. Coating for more than 3 min lowered cell performances as shown in the figure. Since the coating temperature is high, dye degradation may occur. According to Fredin et al.[131], Ru-based dyes (N719) start to degrade at high temperature from 120 ^{o}C to 250 ^{o}C under air or nitrogen. Although they did not mention the temperature near 100 ^{o}C, we observed the similar trend as will be described later.

In order to confirm that the dye is saturated on TiO_2 surface comparably to the conventional methods, the amount of loaded dye on TiO_2 surface is measured. For this comparison, the dyecoated working electrodes were immersed into a NaOH aqueous solution. The basic solution removes all the dye molecules from the TiO2 surface, and the amount of dye can be compared by UV spectroscopy analysis. When the same area of the electrode is dissolved into the same volume of NaOH aqueous solution[132], the ratio of peak intensities from 5 sets of comparison is 1.0 ± 0.03 (ref)/0.984 (fast dye) ± 0.05. The

average amounts of dye molecules in a unit area are 1.418×10^{-7} mol/cm^2, 1.396×10^{-7} mol/cm^2 for reference cell and EG respectively. Interestingly, the number of dye molecules on TiO$_2$ reached over 80% of saturation within a minute when EG solvent was used (1.121×10^{-7} mol/cm^2). 2 min treatment gives over 90% (1.308×10^{-7} mol/cm^2). 3–4 min treatment did not make any noticeable changes. However, when glycerol was used as solvents, the amount of dyes in TiO$_2$ surface drastically decreased. Theaverage amount of dyes by glycerol solvent is 8.64×10^{-8} mol/cm^2, which is around 60%. Temperature is also a very important factor which affects the dye coating. Since ethylene glycol showed the best performanceamong multiols, temperature dependence was mainly studied with ethylene glycol. In order to study the effect, the temperature was varied from 60 $^{\circ}$C to 160 $^{\circ}$C, while the concentration of dye and the reaction time were fixed at 20 mM and 3 min, respectively. Figure 6-2. shows the cell performance depending on the temperatures. The maximum temperature dye can survive was considered to be 100–120 $^{\circ}$C. This temperature may be extended by removing any oxygen and water from the reaction. Since ethylene glycol is quite viscous and non-volatile near 100 $^{\circ}$C, the working electrode can be protected from environmental oxygen for a short period while coating dye. As expected, the cell performance fell drastically after 120 $^{\circ}$C. As mentioned earlier, dye degradation at temperatures over 120 $^{\circ}$C is main reason for the drop.

(a)

(b)
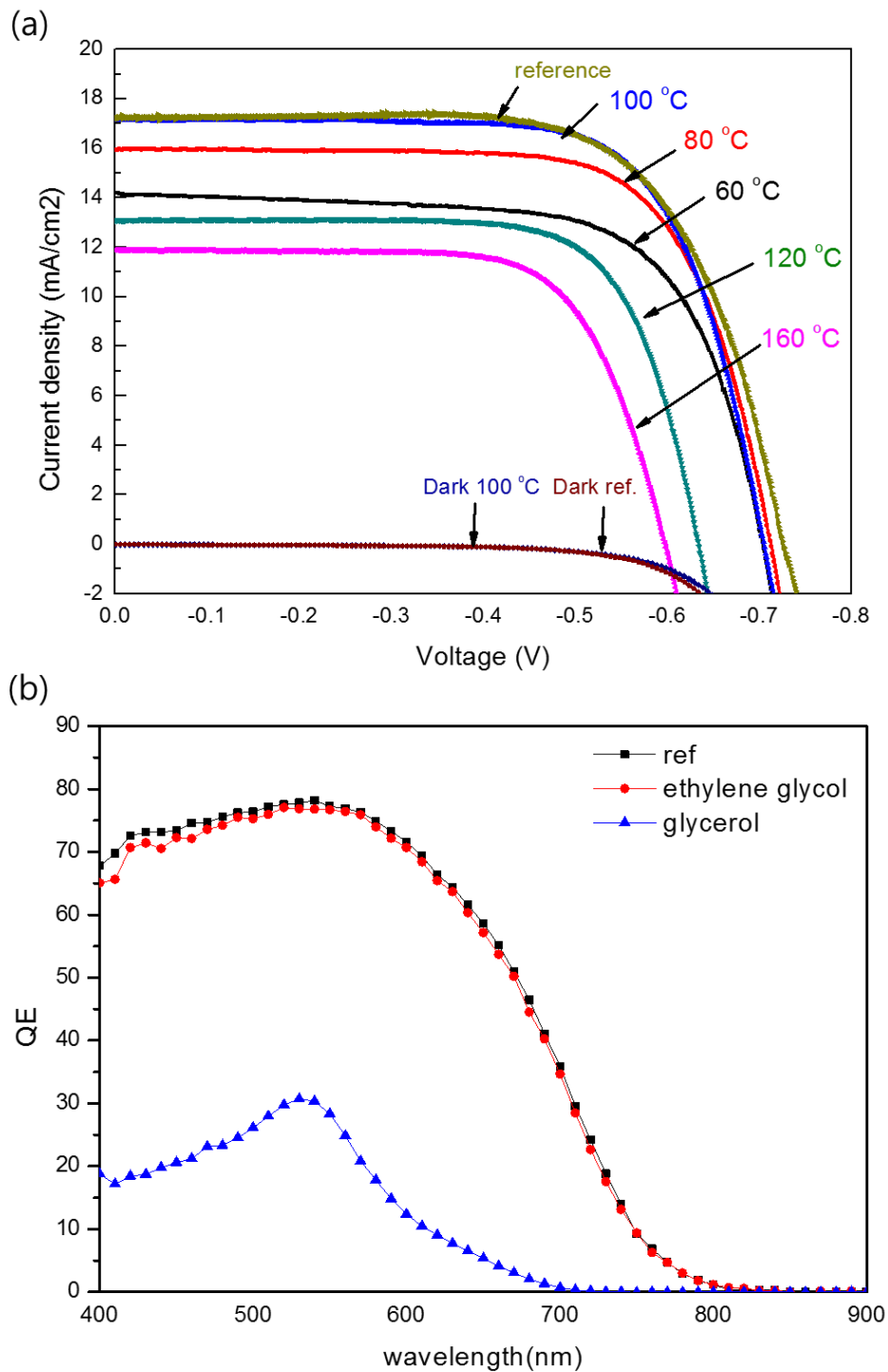
Figure 6-2. (a) JV curves for DSSCs with photo-anodes prepared at different temperatures. (b) The inset is IPCE spectra of cells prepared by conventional method (black), EG solvent at 100 $^{\circ}$C (red), and glycerol (blue).

In order to observe the conformation of dye depending on the preparation methods, diffuse

reflectance infrared Fourier transform (DRIFT) spectra were obtained and compared. These reveal any differences between the dyes which are prepared by a conventional low concentration method or by a higher concentration in ethylene glycol. Fig. 3 shows 4 set of DRIFT spectra.
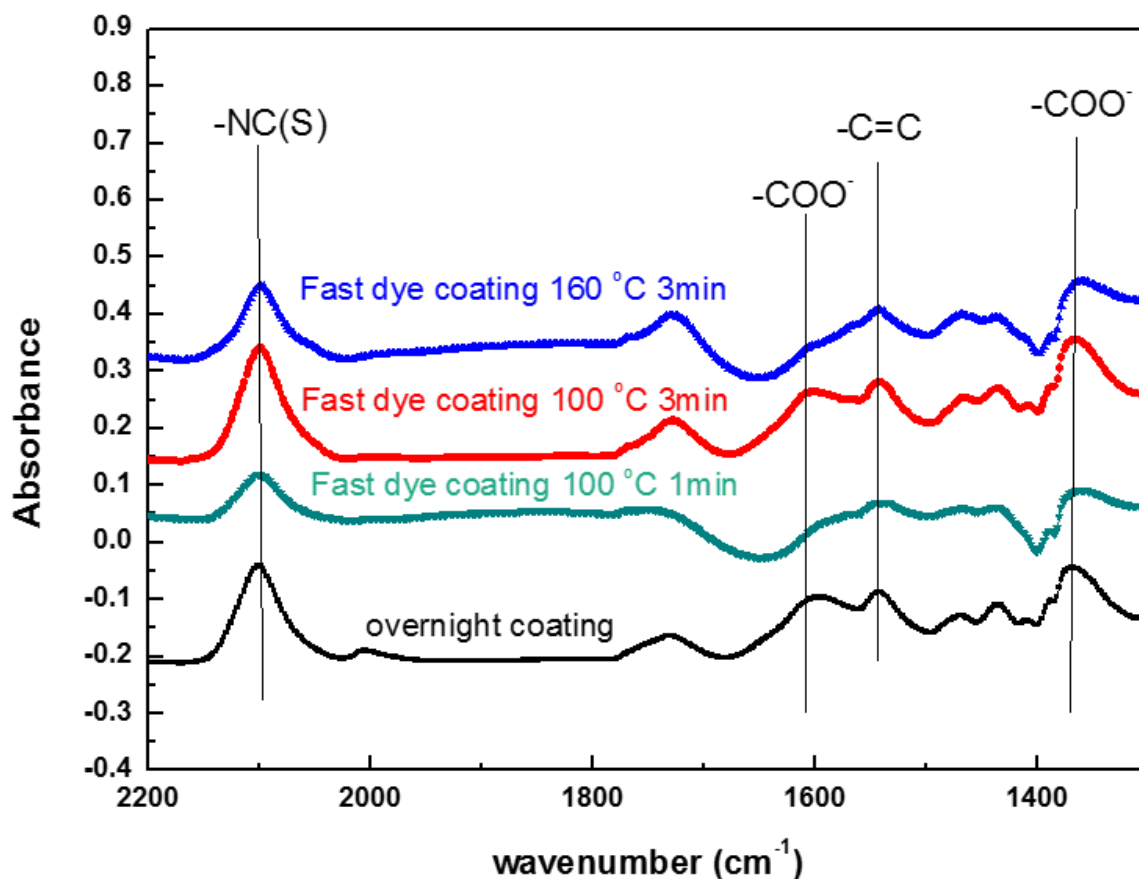
Figure 6-3. A comparison of DRIFT spectra sets obtained from conventional method (bottom,black), fast dye coating at 100 $^{\circ}$C for 1 min, 3 min(third from the bottom, red), and fast dye coating at 160 $^{\circ}$C (top, blue).

The bottom setis obtained from the sample using the conventional method. The second set and the third set from the bottom are obtained from the sample using ethylene glycol at 100 $^{\circ}$C for 1 min and 3 min, respectively. The top set is obtained from the sample which has been prepared at 160 $^{\circ}$C. Although the third set (100 $^{\circ}$C, 3 min) is not completely identical to the bottom one (overnight), most of the peaks which identify the states of the dye, appear to be very similar. There are no noticeable peak shifts between the two spectra sets. The peaks of interest appear at 2100 cm^{-1}, 1607 cm^{-1}, 1541 cm^{-1}, and 1368 cm^{-1}, which are corresponding to NC(S), carbonyl groups asymmetric vibration (COO$_-$), aromatic carbon double bonds, and carbonyl groups symmetric vibration (COO$_-$), respectively[133-136]. When the temperature is controlled at 100 $^{\circ}$C, the main concern is dye degradation due to oxygen and water from the environment. However, the DRIFT spectra are almost identical, which means most of the dye is still functioning without noticeabledegradation. When the peaks at 2098 cm^{-1} are compared in two spectra

sets, the peak shift is only 1 cm^{-1}. The physisorbed or chemisorbed carbonyl group can be identified by analyzing a peak at 1368 cm^{-1}. IR peaks for any isolated dyes (physisorbed ones) will appear at near 1344 cm^{-1}. As shown in Fig. 6-3., we have not observed a noticeable shoulder in DRIFT at near 1344 cm^{-1} [133]. This indicates that dyes are chemically bonded to TiO$_2$ surface. In the case of fast dye coating for 1 min, the peaks are weak, quite broad and dull, which means that dye molecules are not coated clearly yet. The treatment at a high temperature of 160 ∘C degraded dyes, and this was observed by DRIFT too. According to the top set of spectra, most of DRIFT peak intensities are weaker than those of reference or the sample prepared at 100 ºC. This might be due to degradation of dyes. The peak for ligands of NC(S) at 2100 cm^{-1} and the peak for chemisorbed carbonyl group at 1607 cm^{-1} and 1368 cm^{-1} are obviously decreased. Cell performance also proves that most of dyes are chemically bonded when the sample is treated at 100 ºC. Since the dye molecules are surrounded by viscous ethylene glycol, they can remain protected for a short time from the oxygen or water which cause dye degradation. Of course, the risk of oxygen damage can be minimized by placing the experiment in an inert gas condition. In this experiment, we used a normal, in-air condition after purging the ethylene glycol with nitrogen gas. If nitrogen condition is applied, less oxygen can be involved into the reaction, which will be desirable for the cell performance.
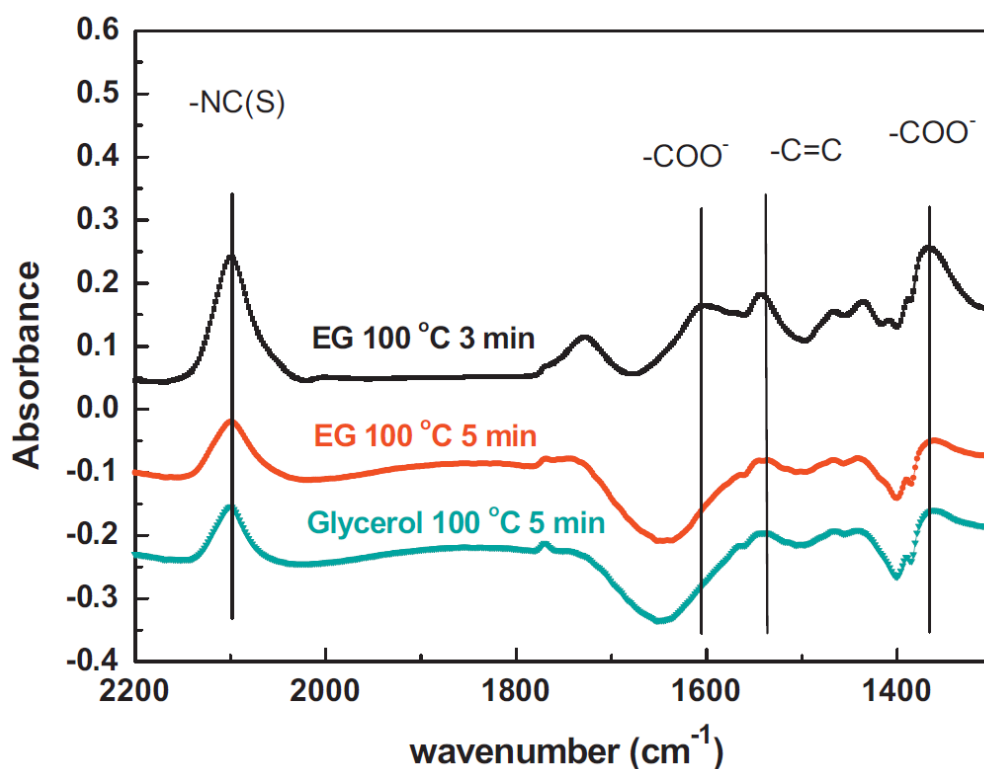
Figure 6-4. comparison of DRIFT spectra sets obtained by controlling coating time for more than 3 min. The top set is from a reference electrode (EG, 3 min), and other sets are from EG/5 min and glycerol/5 min coating, respectively

Fig. 6-4. shows dyes degradation when the working electrodes are treated at 100 $^{\circ}$C for more than 3 min. The top set was obtained from the sample prepared by EG solvent for 3 min as a reference, and other sets were prepared by EG solvent (middle) and glycerol (bottom) for 5 min, respectively. When the electrodes were prepared by 5 min coating at 100 $^{\circ}$C in EG and glycerol, the trend of DRIFT spectra followed the set of DRIFT for 160 $^{\circ}$C treatment. The peak for ligands of NC(S) at 2100 cm^{-1} and the peak for chemisorbed carbonyl group at 1607 cm^{-1} and 1368 cm^{-1} are decreased. This may support dye degradation by longer time coating than 3 min at even 100 $^{\circ}$C.
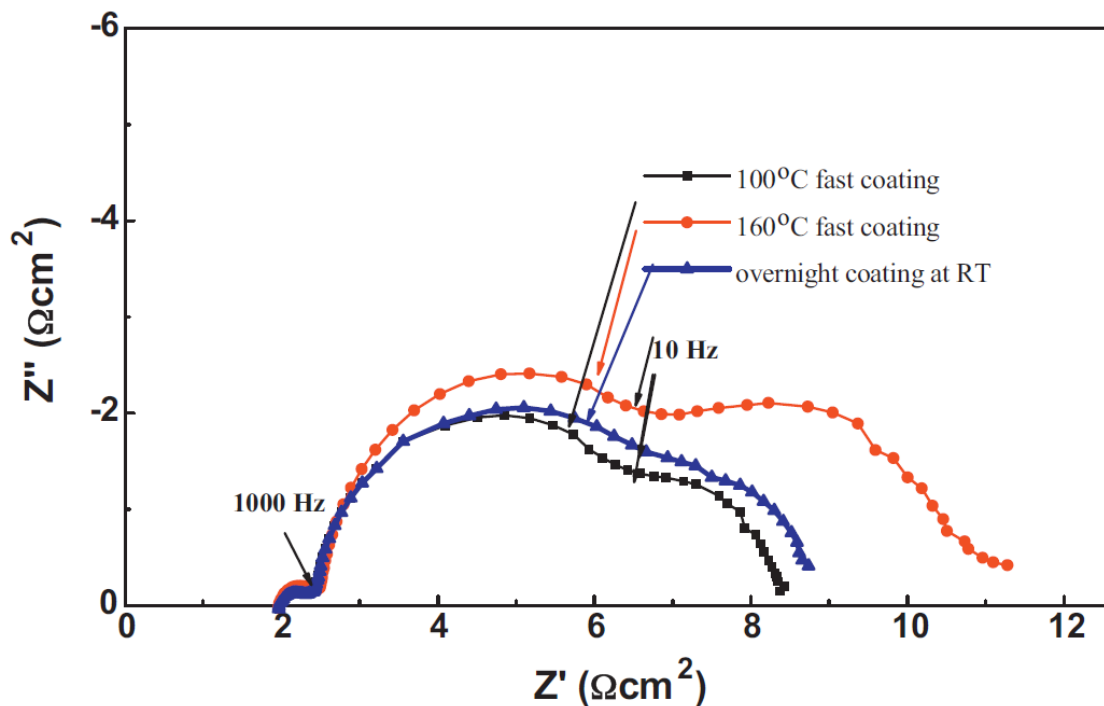
Figure 6-5. EIS spectra for DSSCs with photo-anodes which are prepared at different temperatures.

The cells were compared by EIS analysis. EIS analysis is often used to observe the interfaces in DSSCs such as TiO$_2$/dyes/electrolytes and electrolytes/counter electrode.[137-139] Typical EIS spectra show 3 semi-circles, which correspond to the counter electrode/electrolyte, TiO$_2$/dyes/electrolyte, and electrolytes in order from left. To investigate the dye layers, the second semi-circle were compared. Figure 6-5. shows 3 EIS spectra sets, obtained from samples which are prepared by the conventional method (black square), at 100 $^{\circ}$C (green triangle), and at 160 $^{\circ}$C (red circles). The EIS spectra for the sample prepared at 100 $_{\circ}$C are very similar to the spectra for the reference cell. An apparent change was observed from the sample whose dye-coating was prepared at 160 $_{\circ}$C. The EIS spectra for a sample prepared at 160 $^{\circ}$C showed an increased semi-circle for the second arc, which is representing a resistance at the TiO$_2$/dye/electrolyte interface. Normally, the increased resistance for the second arc represent a better barrier for electron back transferring from TiO$_2$ to the electrolyte, which can improve cell

performance. In this experiment, the increased resistance did not improve the cell performance. We are suggesting two possibilities. (1) N719 is a Ru complex surrounded by bipyridil group ligands. When dye molecules are degraded, the products of the degradation could be pyridine derivatives. (There could be many different forms, which have not been investigated clearly yet.) These derivatives could adsorb on TiO_2 surface, and then acts as barrier for electron back transferring. Since many dyes are degraded after high temperature treatment, the current densities are drastically decreased, and which may also affect open circuit voltage lowering. These degraded products may diffuse into the electrolyte, and affect the electrolyte function too, and this increased the third arc (resistance by diffusion in an electrolyte). (2) The main frame of N719 molecules can still adsorb on TiO_2, and partial ligands could be disassembled from the molecules. Especially, NC(S) functional groups might be detached from the molecules. (According to DRIFT in Figure 6-3., NC(S) peaks are drastically reduced.) Then, N719 might be malfunctioning. These broken N719 dye molecules may not generate electrons properly, and they act as light-inactive molecules. When degraded dyes are not fully functioning for electron flow path, they may act as blocking agent at the TiO_2 surface.

Finally, the cells by new method we developed were tested for stability. Figure 6-6. shows the comparison of stabilities for cells by conventional method (black) and fast coating method (red) for a short period, 3 weeks. All the parameter changes are not noticeable for 3 weeks, which means both of the electrodes are quite comparable to the conventional ones. Therefore, this new method may be adopted to coat dyes on TiO_2 working electrode.
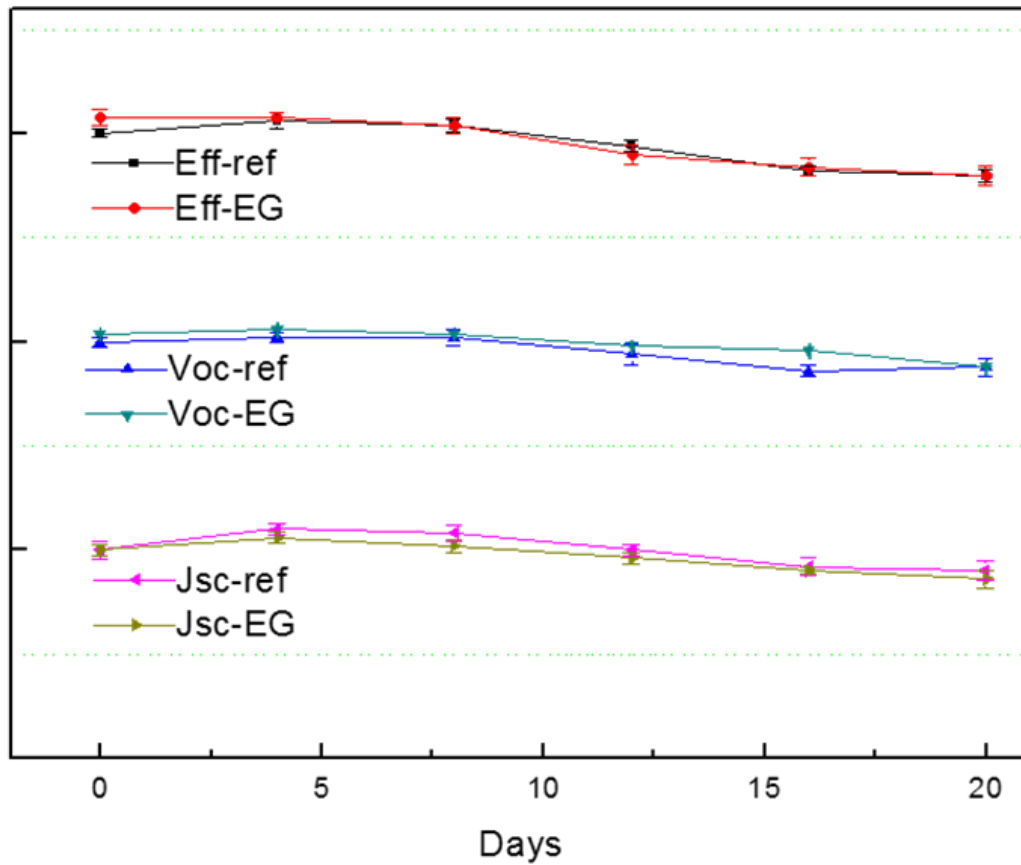
Figure 6-6. Comparison of stabilities for cells prepared by conventional method and fast coating method for a short period, 3 weeks.

6.4. Conclusion

In this paper, we showed a new coating method for DSSC working-electrode preparation. The method controls the reaction temperatures with concentrations of N719 in various solvents. Diol, especially ethylene glycol, was ideally applied to shorten the coating time to only 3 min which is much improved from the several hour scale needed for the conventional solvents such as acetonitrile and ethanol. The cells were compared by characterization with JV measurement, dye uptake amount, DRIFT, and EIS. Performance and other characteristics of the cells with working electrodes prepared by this new method were very comparable to those prepared by conventional methods. We believe that this new solvent system to coat dyes on working electrode is quite comparable to the conventional coating methods, and gives many advantages such as shortening coating process and removing container to dip the cells.

Chapter 7. Study of dye adsorbing with DMSO

7.1. Intriduction

Optimization of high density dye adsorption is also one of the important parameters to electron injection results in enhanced cell efficiencies.[140-141] Till date ultrafast femtosecond transient absorption technologies has been used to determine the kinetics of electron injection and absorption change processes[142] occurring from the singlet excited state[143-144] and competing with itra-molecular relaxation states has been reported.[145-146] It was also explained that strong spin-orbit coupling from the ruthenium heavy metal atom accelerates intersystem crossings to 100 fs[147] resulting in increased injection mechanism via lowering energy in triplet excited state. To achieve higher efficiencies studies have been also carried out as a function of pH environment,[148-149] excitation wavelength,[149-150] inclusion of cationic ions,[151] TiO_2 fermi level,[152] bridging positioned between dye and TiO_2 surfaces,[153] and variation of solvent choices.[154-155] Moreover, dye aggregation at room temperature suggested to reduce the efficiency of electron injection for some sensitizer dyes, thereby reducing device performance.[156] DMSO is one excellent solvent having low vapor pressure and largely in use of pharmocological actions such as membrane transport, dieresis, radioprotective and it is colorless with boiling point of 189 ℃. So to use this solvent at high temperature dye adsorption can be the obvious choice to address dye aggregation and high temperature dye adsorption which have potential to reduce time of dye adsorption.

Nazeeruddin et al. investigated N719 dye adsorption on TiO_2 by FTIR[157] and concluded that dye anchors through caboxylate ions, Perez Leon et al. speculated carbozylate coordination by ligand linkages.[133] Test fabrications of DSCs with various N719 exposures suggested that the degeneration of the physisorbed N719 and the enhancement of the chemisorbed dye adsorption are effective in enhancing power generation. Based on the above information, to achieve high quantum yields of the excited state electron transfer process the dye ideally needs to be in intimate contact with the semiconductor surface, the enhancement of N719 adsorption on the TiO_2 electrodes is important to promote power generation in DSCs. In this paper we employ and investigated a novel method by using DMSO solvent for the N719 sadsorption and enhancing the dye adsorption by immersing the TiO_2 electrode at high temperature of 160℃ such as high temperature have great chance to increase chemisorptions and prevent aggregation of dyes in the uniform film along with the possible anchoring of sulphoxide bonding to the titania in addition to carboxylate group, we have confirmed the enhancement of dye adsorption density by employing FT-IR and drift IR. The influence of heat treatment over dye-sensitized electrodes with respect to the resultant photovoltaic efficiency was remarkable when used as working electrodes in DSCs.

7.2. Experimental

7.2.1. Preparation of TiO_2 photo-anodes

The TiO_2 paste consisting of 20 nm sized anatase particle was purchased from (ENB Korea), it was then coated on the F-doped SnO_2 conducting glass substrate (FTO, TEC 8, 2.3 mm, Pilkington) by using a doctor blading technique. Prior to doctor blading the purchased FTO glass substrate was cleaned with acetone, ethanol, nitrogen blowing and drying at 80 $^{\circ}$C in a owen. Then the TiO_2 paste coated layer after room temperature air drying was sintered at 500 $^{\circ}$C for 2 h in a muffle furnace. The thickness of the main active layer was 12μm ($\pm$ 0.5μm) with a scattering layer, with the active area of 1.2 mm^2 (3 mm×4 mm).

7.2.2. Preparation of Dye solution

The TiO_2 photoanode was dissolved in the prepared dye solution by using 0.35g of $(Bu_4N)_2[Ru(dcbpyH)_2(NCS)_2]$ (N719, Ever Solar) in 10 ml of dimethyl sulfoxide (DMSO, 99.9%, Aldrich) with the smooth stirring at 80℃ for 4h. Since DMSO is stable at higher temperature so the dye solution was heated up to 160℃ then prepared electrode was immersed in the solution for 30s only and subsequently carefully rinsed with ethanol solution. Sensitized solution was sonicated prior to heat treatment in order to avoid any aggregate formation. The above prepared sample was compared with room temperature prepared N719 dye adsorption for 18h and was prepared in usually laboratory made solvent of 10 ml tertiay-butyl alcohol in 10 ml acetonitrile (Aldrich).

7.2.3. Device Fabrication and Characterization

Transparent counter electrode were prepared by chemically depositing 10 mM hydrogen hexachloroplatinate (IV) hydrate (99.9%, Aldrich) in 2-propanol was placed onto a second set of transparent conducting FTO glass. Sandwiched cells were prepared by the heat treated dye adsorbed anode prior at 500°C for 2h with the counter electrode by using a 2μm of transparent Surlyn 1472 polymer film with heating at 60℃. Finally, the electrolyte was introduced to internal space through the drilled small holes in the counter electrodes which were immediately sealed covered slides and additional strips of Surlyn film to avoid the leakage of any spilled electrolyte. Photocurrent-voltage (I-V) curves of the DSC was measured by current-voltage characteristics measurement (digital source meter; model 2400, Keithly) in conditions illumination (AM1.5, 100mW/cm^2 ;model ORIEL-Sol-3A,

Newport) was calibrated to 100 mM/cm² using a reference Si photodevice. The incident photon to current conversion efficiency (IPCE) was the equipment of PV measurements, Inc. (model QEX7 series). IR spectra (nominal 4-cm^{-1} resolution) were measured using a IR : 670-IR / 620-IR Imaging (Varian, USA) , equipped with a liquidN$_2$ cooled MCT detector. FE-SEM images were taken from field emission scanning electron microscope (Quanta 200, FEI, USA).

7.3. Results and discussion

Figure 7-1. shows the photocurrent action spectrum of N719 dye dissolution in DMSO at 160℃ for 30s and the solar cells fabricated based on 12μm thick nanocrystalline TiO$_2$ films immersed into it.

Figure 7-1. IPCE characteristic curves obtained from the dye sensitized solar cell (DSC) made with N719 solutions (a) at room temperature with solvent acetonitrile and alcohol (b) in DMSO as solvent at high temperature (160℃)

The measurements of IPCE were carried out with white bias light and modulated monochromatic

light and it is a good evidence of the spectra reflecting dye adsorption. The incident monochromatic photon-to-current conversion efficiency (IPCE) plotted as a function of excitation wavelength reaches a value of 90% in the plateau region as shown in figure and defined by the equation 1.

$$IPCE = \eta fH$$

where η is net electron injection efficiency, f is fraction of incident light adsorbed by the dye and H is charge collection efficiency. The important effect of the high temperature dye adsorption is obviously seen where possibility of better charge injection (η) and owing to better spatial dye adsorption by thermal treatment for very small time (30s) takes place as seen in the red region and where as when we use general method of dye adsorption in mixture of acetonitile and ethanol as a solvent the IPCE was observed as 85%. This results shows that the even at 30s in hot solvent substantial dye molecule adsorbed.

Fig.2 shows the performance J-V curve of the prepared sandwiched devices analyzed under the illumination (100mW/cm^2).
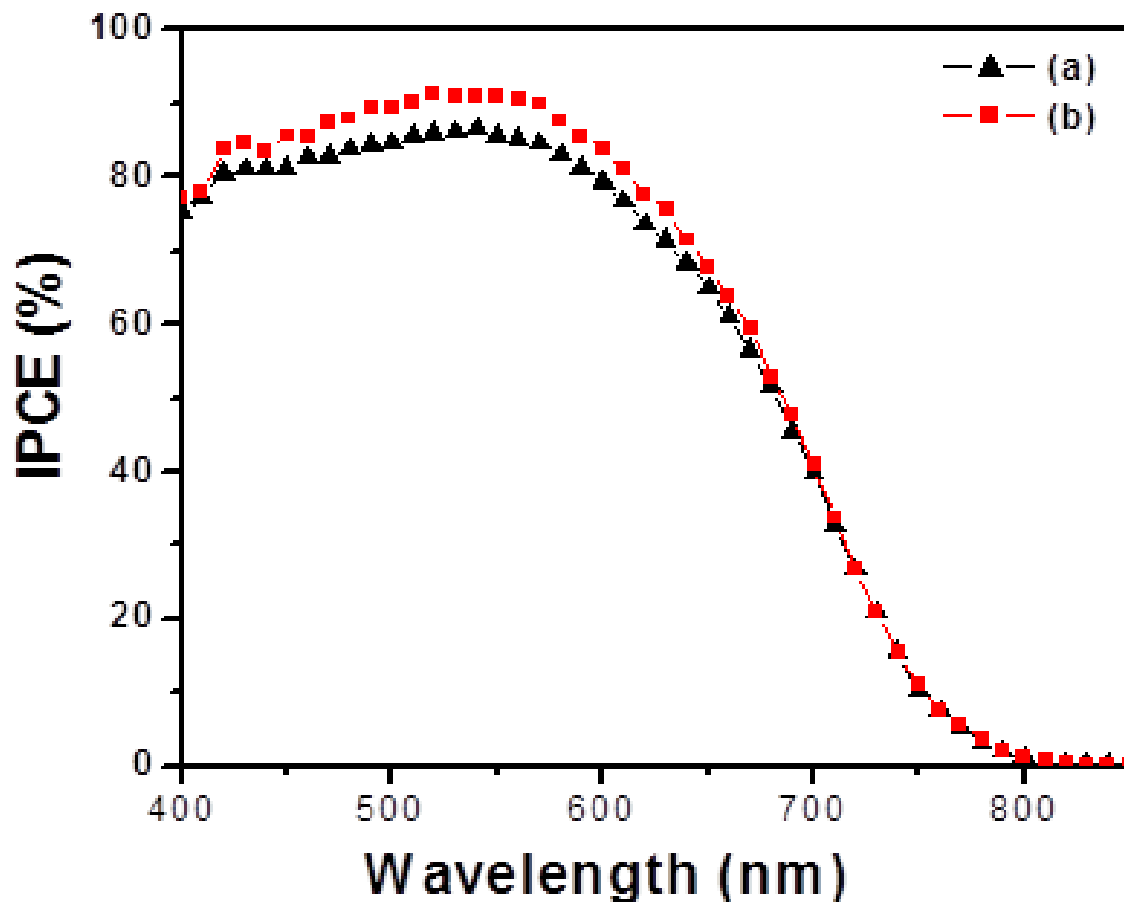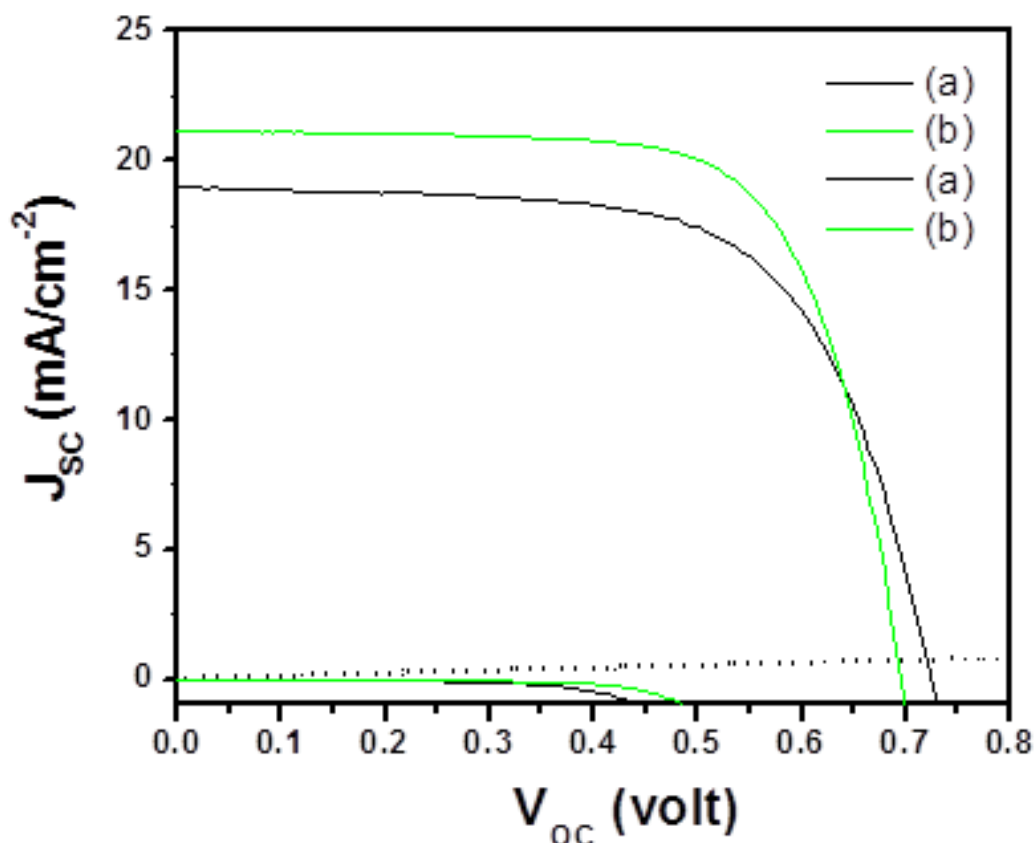

Figure 7-2. J-V characteristic curves obtained from devices of dye sensitized solar cell (DSC) made with N719 solutions (a) at room temperature with solvent acetonitrile and alcohol (b) in DMSO as solvent at high temperature (160℃)

It can be observed that the immersion in DMSO with solution temperature of 160 ℃ giving a maximum efficiency of 10.3% (J_{SC} of 21.1, V_{OC} of 0.69 and FF of 70.4%) better than the room temperature solvent adsorption process in and acetonitrile for longer duration (18h, 24h) measuring a short circuit photocurrent density of 19 mA/cm^2, V_{OC} of 0.72 and FF of 65.2%. The high efficiency of the immersed sample in DMSO at high temperature is conjectured to be high N719 dye adsorption is very much effective in efficiency enhancement. However, we have expected degradation of photovoltaic efficiency as mechanical and vibrionic displacement of nanoparicle due to high temperature of dye solution treatment and we kept it for very short time but longer time do show enhancement, contrary we have found that better efficiency results from the enhanced chemical bonding between the TiO$_2$ anode and N719 dye molecules which may induces by thermodynamically increased velocities of dye molecules causing no aggregation and the energy induces by heat to dye molecules help them to penetrate deeper into the photoactive layer. The similar results was also confirmed by Hiros el al.[135] where they carried out dye adsorption at 80℃ in acetonitrile and tertiary butyl alcohol solution and measured in respect of electrical characterization on the anode by measuring series (R_s) and shunt (R_{sh}) resistances by Ishibashi method. They explained contaminated water removal which may cause lowering of electric field between the TiO$_2$ and dye molecule linkages by generating high dielectric constant with the heat treatments. However, we thinks that it's very difficult to water desorption takes place at lower than 100℃. Only high temperature (160℃) dye adsorption contributes to promotion of high efficiency where contaminated water desorption have substantial no effect. Figure 2 shows dark currents are almost same except a little increase in V_{OC} of the high temperature dye adsorption.

Fig.3 shows the IR spectra of the N719 dye adsorbed on the TiO$_2$ surfaces with high temperature DMSO immersion and room temperature adsorption in mixed acetonitrile and ethanol solution up to 24h immersion. For reference bare powder of N719 spectra was also taken (Fig.3(a)). Region 1000 to 2200 cm^{-1} is supposed to be in particular interest owing to various C-O stretching bands such as carboxylate and carboxylic acid contribute in anchoring with the titania surface. The isocyanato ligand has intense υ (C-N) at 2100 cm^{-1}. The spectrum in all the cases exhibits C=O stretching modes at 1712 and 1784 cm^{-1}. There are five bands in the region 1700-1400 cm^{-1}, at 1604, 1544, 1468, 1440, and 1404cm^{-1}. However, in the high temperature adsorption the bands at 1468 are absent and other peaks are little shifted and less intense shoulder observed. The first four peaks agree well with literature values for the ring stretching modes of [Ru(bpy)3]2+, reported at 1608, 1563, 1491, and 1450 cm-, given that some shifts are expected due to ring substitution. The bands at 1229 cm-1 ascribed to be due to υ(C-O) slightly shifts in the DMSO solution. There are a number of less intense bands to lower energy (~1000 cm^{-1}) in [Ru(bpy)$_3$]$^{2+}$ which contain both C-C and C-N stretching and CCH deformation character. The

double IR absorption peaks of the symmetric vibration of the COO⁻ group can also be seen ~1350 cm⁻¹ in the figure. Perez Leon et al. also reported that the physisorbed N719 molecules, such as N719 powder on its own, exhibited the IR absorption of COO at 1350 cm⁻¹, while the chemically bonded N719 with bidentate or bridging linkage causes a shift to 1375 cm⁻¹. Some N719 molecules were chemisorbed to the TiO_2 surface and the others were isolated or physisorbed on its surface. In case of high temperature adsorption carboxylate linkage bands located at 1406 and 1604 a difference of 200 cm⁻¹, however in the normal dye solution it was observed as 1350 and 1604 a difference of 252 cm⁻¹ which is consistent with bridging or bidentate coordination.
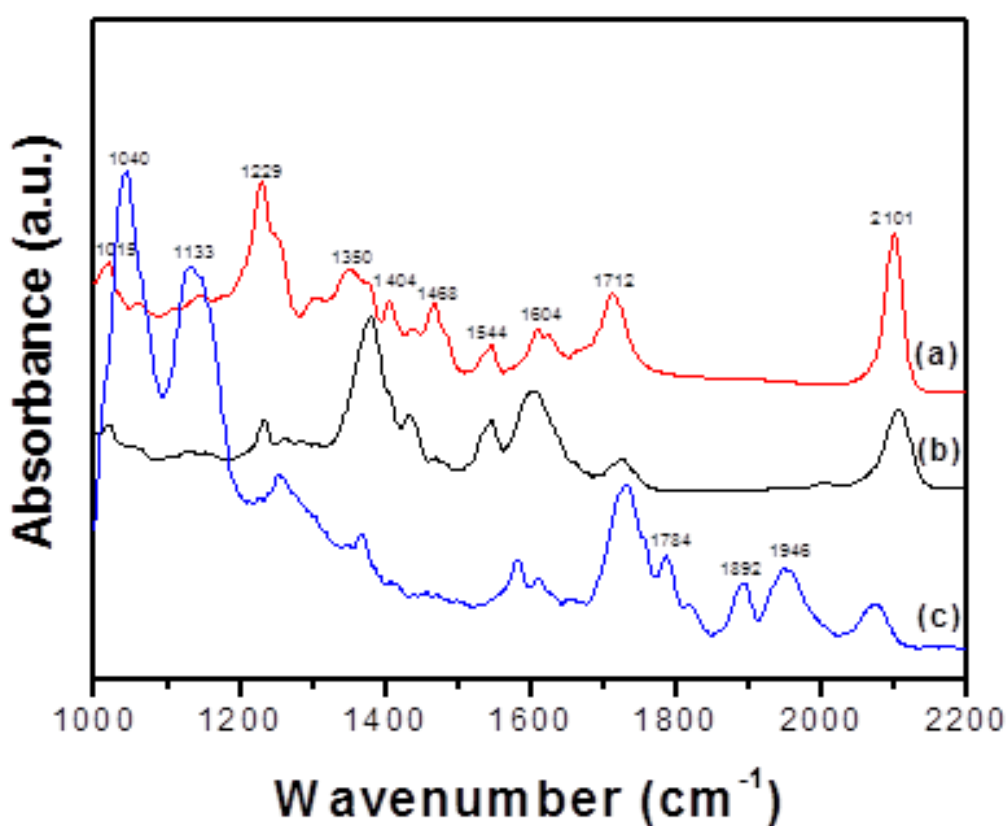
Figure 7-3. FTIR spectra of N719 adsorbed on nanocrystalline TiO_2 film obtained from N719-adsorbed films compared with the signals (a) of the dye powder, (b) at room temperature with solvent acetonitrile and alcohol, (c) in DMSO as solvent at high temperature (160℃)

The IR absorption peak of the COO asymmetric vibration mode at wave numbers from 1608 can be attributed to the two chemical states of physisorbed and chemisorbed N719. Previous studies[13] suggest that the N719 dye adsorbs preferentially on the OH sites on TiO_2 surfaces and makes bridges for electrons to the TiO_2 electrode with the bidentate or the bridging linkage. When the solution temperature was increased from room temperature to 160℃, the IR absorbance of NCS was decreased it may be due to the two reason: either it results from dye degradation or change of dipole moments due to the

different deprotonation of the complex adsorb at titania surface. Increasing the solution temperature enhances the chemisorbed state (bidentate bonding), which suggests that we can improve power generation in DSCs using a high temperature dye solution.. When the solution temperature was room temperature, the NCS peak was also enhanced compared to DMSO solvent. In this case, the physisorbed state became prominent. The physisorbed N719 just offers shade to the chemisorbed N719 and suppresses the power conversion efficiency.

Fig.4 depicting DRIFT IR spectra of the high temperature and room temperature of bare DMSO solvent used for dye solution. The DMSO has typical high intense band S=O bonding at 1051 cm^{-1}.
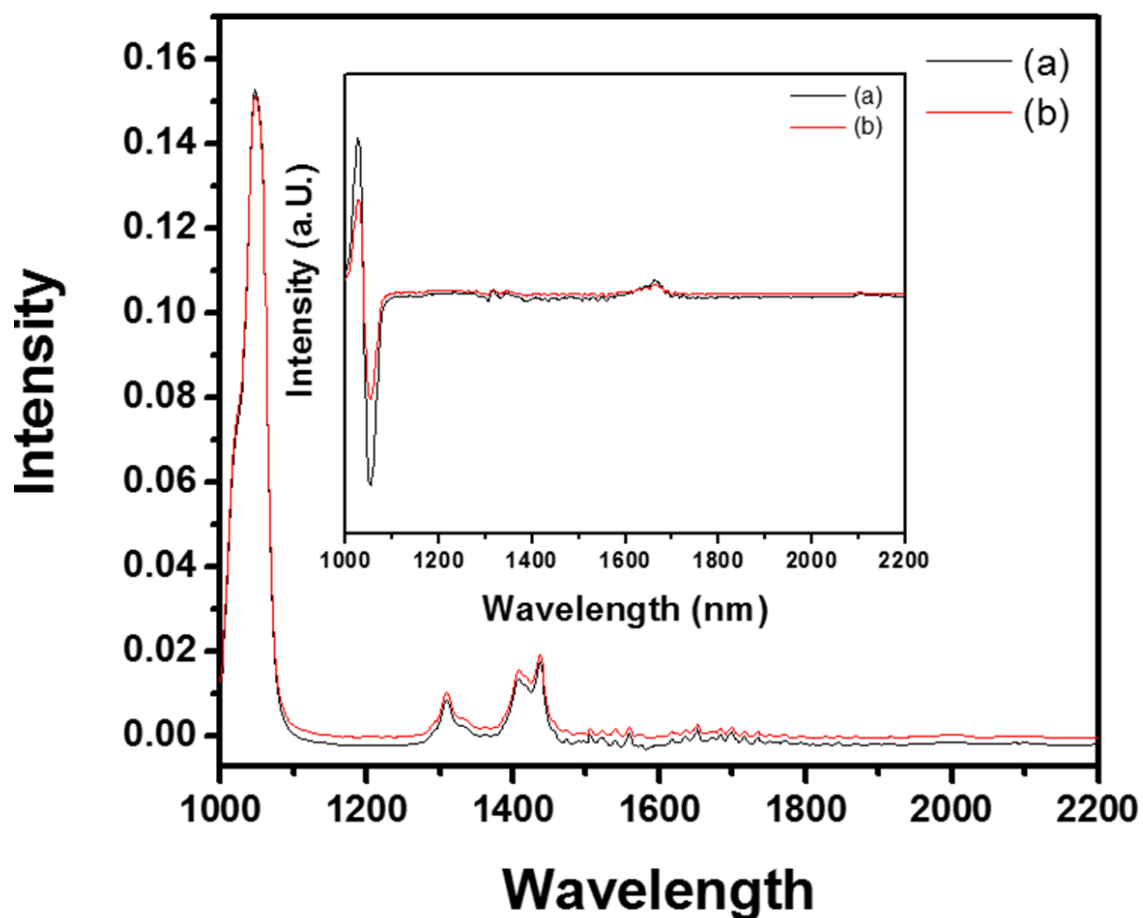
Figure 7-4. Drift IR absorption spectra of bare DMSO (a) high temperature (b) at room temperature, Inset drift IR absorption spectra (a) DMSO with N719 dye at high temperature (160℃), (b) at DMSO with N719 dye at room temperature

It was observed that so specific difference of the solvent properties was observed owing to higher temperature treatment, showing no structure, homogeneity, concentration and absorption coefficient difference. Both the dye adsorbed solution shows similar intensities but higher temperature treated sample shows little higher intensities showing better absorption in solution. Inset figure shows blank

DMSO solution at 160℃ and room temperature treatment in drift IR measurement. We do not observe any spectral difference at higher temperature that means the DMSO is stable at this temperature condition.

Fig.5 shows the details of field emission scanning electron microscopy (SEM) of the cross section and well as film morphology. The cross section measurement shows that TiO_2 active layer thickness of 12 μm and the films observed are quite dense, relatively uniform in appearance. The efficiency of the charge injection process is strongly dependent on the type of binding of the dye to the semiconductor. This suggests that the surface-anchoring form plays an important role for the solar cell efficiency, and it also influences its stability. Electron exchange between the TiO_2 conduction band and one single trap level takes place via trapping and detrapping.
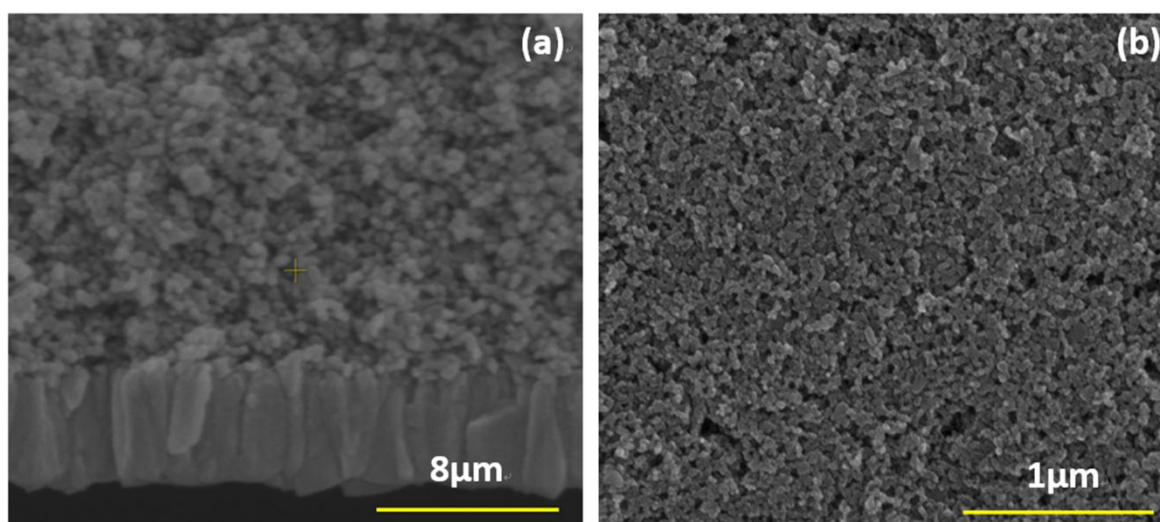
Figure 7-5. Field emission scanning electron microscopy image of the nanocrystalline TiO_2 layer of the dye sensitized solar cell made in DMSO solvent (a) Cross-sectional image (b) morphology image

Electrons which are trapped can also be transferred into the electrolyte, and these electrons, contrary to electrons which undergo trapping and detrapping, are lost for the photocurrent. DMSO may form a charge barrier may retard the interfacial recombination process are often included in the organic photovoltaic (OPV) family because of the organic nature of at least part of its constituents. This inherent geometry of DMSO having S=O bonding, low vapor pressure and very less immersion time offers the unique prospective to fashion the ordered interface enhanced high amount of dye adsorption. Such film would impair the flow of dark current across the junction, reducing the back-reaction rate and increasing the overall solar to electric power conversion efficiency of the cell.

7.4. Conclusion

In this study enhanced efficiency of 10.3% was observed by N719 dye adsorption at high temperature (160℃ for 30s) in DMSO solvent on TiO_2 electrodes due to the increased dye adsorption and better carboxylate and sulphoxide groups anchoring process of the dye adsorption on the semiconductor surface. FTIR spectroscopy used to investigate the dye adsorbed surfaces where it can be conjectured that carboxy groups can interact with metal ions in various ways: by physical adsorption via hydrogen bonding or via chemical bond formation with a unidentate linkage, a bidentate linkage, or a bridging linkage. Intense band of S=O linkage was also observed at $1040cm^{-1}$. The high temperature adsorption in DMSO solvent is effective in enhancing the adsorption of N719 dye molecules and substantially reduction in immersion time (30s) promoting the power generation of the DSC. This study provides an insight into achieving the low cost, high performance DSCs in less time.

Chapter 8. General conclusion

This thesis is focused on the improvement of performance of DSC. Unique materias as Zno, odered mesoporous carbon, graphene-metal nonoparticle composit was introduced to DSC to deveolp the performance.

In this thesis ZnO with novel nanostructure was introdueced with adventage of large surface area and good morphology for penetrating of the dye solution. This work provides intriguing way of structurally designing of ZnO with large surface area and moderate morphology for DSSCs and other applications.

rGO/metal nanoparticle hybrid films and OMC–CNT, where the primary particles of the OMCs are interconnected via the CNTs are introduced for counter electrodes in DSC as Pt replacement counter electrode. The enhanced electrochemical stability of the Au nanoparticles on rGO was attributed to the unique combination of the presence of defects as well as hydroxyl and carboxyl functional groups. the OMC–CNT-based cell showed an excellent cell efficiency which was primarily attributed to its remarkably enhanced electrical conductivity as well as its intrinsic catalytic activity. This work provides an intriguing way of structurally designing a low-cost, Pt-free, high-performance counter electrode material for DSC.

New coating method for DSC working-electrode is introduced, too. The method controls the reaction temperatures with concentrations of N719 in various solvents. Sorts of alcohols and DMSO was invetigaed and can be ideally applied to shorten the coating time to only 3 min which is much improved from the several hour scale needed for the conventional solvents such as acetonitrile and ethanol. The cells were compared by characterization with JV measurement, dye uptake amount, DRIFT, and EIS. Performance and other characteristics of the cells with working electrodes prepared by this new methods were very comparable to those prepared by conventional methods.

REFERENCES

1. Hansen, J.; Sato, M.; Ruedy, R.; Lo, K.; Lea, D. W.; Medina-Elizade, M., Global temperature change. *Proceedings of the National Academy of Sciences* **2006,** *103* (39), 14288-14293.

2. Morton, O., Solar energy: A new day dawning?: Silicon Valley sunrise. *Nature* **2006,** *443* (7107), 19-22.

3. Devos, A., Detailed Balance Limit of the Efficiency of Tandem Solar-Cells. *J Phys D Appl Phys* **1980,** *13* (5), 839-846.

4. Muth, J. F.; Lee, J. H.; Shmagin, I. K.; Kolbas, R. M.; Casey, H. C.; Keller, B. P.; Mishra, U. K.; DenBaars, S. P., Absorption coefficient, energy gap, exciton binding energy, and recombination lifetime of GaN obtained from transmission measurements. *Appl Phys Lett* **1997,** *71* (18), 2572-2574.

5. Daub, E.; Wurfel, P., Ultralow Values of the Absorption-Coefficient of Si Obtained from Luminescence. *Phys Rev Lett* **1995,** *74* (6), 1020-1023.

6. Lindholm, F. A.; Fossum, J. G.; Burgess, E. L., Application of the Superposition Principle to Solar-Cell Analysis. *Ieee T Electron Dev* **1979,** *26* (3), 165-171.

7. Ronald, A. S.; Andres, C., Contactless determination of current–voltage characteristics and minority-carrier lifetimes in semiconductors from quasi-steady-state photoconductance data. *Applied Physics Letters* **1996,** *69*.

8. Bard, A. J., Photoelectrochemistry. *Science* **1980,** *207* (4427), 139-144.

9. Bard, A. J., Photoelectrochemistry and Heterogeneous Photocatalysis at Semiconductors. *J Photochem* **1979,** *10* (1), 59-75.

10. Bard, A. J., Semiconductor Photoelectrochemical Cells. *J Electrochem Soc* **1979,** *126* (3), C145-C145.

11. Miller, B.; Heller, A., Semiconductor Liquid Junction Solar-Cells - Efficiency, Electrochemical Stability, and Surface Preparation. *J Electrochem Soc* **1977,** *124* (3), C130-C130.

12. Oregan, B.; Gratzel, M., A Low-Cost, High-Efficiency Solar-Cell Based on Dye-Sensitized Colloidal Tio2 Films. *Nature* **1991,** *353* (6346), 737-740.

13. Fillinger, A.; Soltz, D.; Parkinson, B. A., Dye sensitization of natural anatase crystals with a ruthenium-based dye. *J Electrochem Soc* **2002,** *149* (9), A1146-A1156.

14. Fillinger, A.; Parkinson, B. A., The adsorption behavior of a rutheninm-based sensitizing dye to nanocrystalline TiO2 - Coverage effects on the external and internal sensitization quantum yields. *J Electrochem Soc* **1999,** *146* (12), 4559-4564.

15. Lu, Y. F.; Choi, D. J.; Nelson, J.; Yang, O. B.; Parkinson, B. A., Adsorption, desorption, and sensitization of low-index anatase and rutile surfaces by the ruthenium complex dye N3. *J Electrochem Soc* **2006,** *153* (8), E131-E137.

16. Spitler, M. T.; Calvin, M., Electron-Transfer at Sensitized Tio2 Electrodes. *J Chem Phys* **1977,** *66* (10), 4294-4305.

17. Tributsc.H; Calvin, M., Electrochemistry of Excited Molecules - Photo-Electrochemical Reactions of Chlorophylls. *Photochem Photobiol* **1971,** *14* (2), 95-&.

18. Tributsc.H, Reaction of Excited Chlorophyll Molecules at Electrodes and in Photosynthesis. *Photochem Photobiol* **1972,** *16* (4), 261-&.

19. Gerischer, H., Surface-Reactions of Compound Semiconductors in Contact with Electrolytes. *Abstr Pap Am Chem S* **1976,** *172* (Sep3), 104-104.

20. Gerischer, H., Photovoltaic Phenomena in Electrochemical Cells. *Abstr Pap Am Chem S* **1976,** *172* (Sep3), 15-15.

21. Gerischer, H.; Gobrecht, J., Power-Characteristics of Electrochemical Solar-Cells. *Ber Bunsen Phys Chem* **1976,** *80* (4), 327-330.

22. Hagfeldt, A.; Grätzel, M., Molecular photovoltaics. *Accounts of Chemical Research* **2000,** *33* (5), 269-277.

23. Jun, Y.; Kim, J.; Kang, M. G., A study of stainless steel-based dye-sensitized solar cells and modules. *Sol Energ Mat Sol C* **2007,** *91* (9), 779-784.

24. Park, J. H.; Jun, Y.; Yun, H. G.; Lee, S. Y.; Kang, M. G., Fabrication of an efficient dye-sensitized solar cell with stainless steel substrate. *J Electrochem Soc* **2008,** *155* (7), F145-F149.

25. Martinson, A. B. F.; Elam, J. W.; Hupp, J. T.; Pellin, M. J., ZnO nanotube based dye-sensitized solar cells. *Nano Letters* **2007,** *7* (8), 2183-2187.

26. Mor, G. K.; Shankar, K.; Paulose, M.; Varghese, O. K.; Grimes, C. A., Use of highly-ordered TiO 2 nanotube arrays in dye-sensitized solar cells. *Nano Letters* **2006,** *6* (2), 215-218.

27. Jennings, J. R.; Ghicov, A.; Peter, L. M.; Schmuki, P.; Walker, A. B., Dye-sensitized solar cells based on oriented TiO2 nanotube arrays: Transport, trapping, and transfer of electrons. *Journal of the American Chemical Society* **2008,** *130* (40), 13364-13372.

28. Roy, P.; Berger, S.; Schmuki, P., TiO 2 nanotubes: Synthesis and applications. *Angewandte Chemie - International Edition* **2011,** *50* (13), 2904-2939.

29. Oh, J. K.; Lee, J. K.; Kim, H. S.; Han, S. B.; Park, K. W., TiO2 branched nanostructure electrodes synthesized by seeding method for dye-sensitized solar cells. *Chemistry of Materials* **2010,** *22* (3), 1114-1118.

30. Wu, W. Q.; Lei, B. X.; Rao, H. S.; Xu, Y. F.; Wang, Y. F.; Su, C. Y.; Kuang, D. B., Hydrothermal fabrication of hierarchically anatase TiO2 nanowire arrays on FTO glass for dye-sensitized solar cells. *Scientific Reports* **2013,** *3*.

31. Baxter, J. B.; Aydil, E. S., Nanowire-based dye-sensitized solar cells. *Applied Physics Letters* **2005,** *86* (5), 1-3.

32. Law, M.; Greene, L. E.; Johnson, J. C.; Saykally, R.; Yang, P. D., Nanowire dye-sensitized solar cells. *Nature Materials* **2005,** *4* (6), 455-459.

33. Liu, B.; Aydil, E. S., Growth of oriented single-crystalline rutile TiO 2 nanorods on transparent conducting substrates for dye-sensitized solar cells. *Journal of the American Chemical Society* **2009,** *131* (11), 3985-3990.

34. Feng, X.; Shankar, K.; Varghese, O. K.; Paulose, M.; Latempa, T. J.; Grimes, C. A., Vertically aligned single crystal TiO 2 nanowire arrays grown directly on transparent conducting oxide coated glass: Synthesis details and applications. *Nano Letters* **2008,** *8* (11), 3781-3786.

35. Zhang, Q.; Dandeneau, C. S.; Zhou, X.; Cao, C., ZnO nanostructures for dye-sensitized solar cells. *Advanced Materials* **2009,** *21* (41), 4087-4108.

36. Shankar, K.; Basham, J. I.; Allam, N. K.; Varghese, O. K.; Mor, G. K.; Feng, X.; Paulose, M.; Seabold, J. A.; Choi, K. S.; Grimes, C. A., Recent advances In the use of TiO 2 nanotube and nanowire

arrays for oxidative photoelectrochemistry. *Journal of Physical Chemistry C* **2009,** *113* (16), 6327-6359.

37. Landmann, M.; Rauls, E.; Schmidt, W. G., The electronic structure and optical response of rutile, anatase and brookite TiO 2. *Journal of Physics: Condensed Matter* **2012,** *24* (19), 195503.

38. Park, N. G.; van de Lagemaat, J.; Frank, A. J., Comparison of dye-sensitized rutile- and anatase-based TiO2 solar cells. *J Phys Chem B* **2000,** *104* (38), 8989-8994.

39. Gratzel, M., Photoelectrochemical cells. *Nature* **2001,** *414* (6861), 338-344.

40. Nazeeruddin, M. K.; Kay, A.; Rodicio, I.; Humphry-Baker, R.; Müller, E.; Liska, P.; Vlachopoulos, N.; Grätzel, M., Conversion of light to electricity by cis-X 2bis(2,2′-bipyridyl-4,4′-dicarboxylate)ruthenium(II) charge-transfer sensitizers (X = Cl -, Br -, I -, CN -, and SCN -) on nanocrystalline TiO 2 electrodes. *Journal of the American Chemical Society* **1993,** *115* (14), 6382-6390.

41. Scholl, M.; Ding, S.; Lee, C. W.; Grubbs, R. H., Synthesis and activity of a new generation of ruthenium-based olefin metathesis catalysts coordinated with 1,3-dimesityl-4,5-dihydroimidazol-2-ylidene ligands. *Organic Letters* **1999,** *1* (6), 953-956.

42. Yella, A.; Lee, H. W.; Tsao, H. N.; Yi, C.; Chandiran, A. K.; Nazeeruddin, M. K.; Diau, E. W. G.; Yeh, C. Y.; Zakeeruddin, S. M.; Grätzel, M., Porphyrin-sensitized solar cells with cobalt (II/III)-based redox electrolyte exceed 12 percent efficiency. *Science* **2011,** *334* (6056), 629-634.

43. Mishra, A.; Fischer, M. K. R.; Büuerle, P., Metal-Free organic dyes for dye-Sensitized solar cells: From structure: Property relationships to design rules. *Angewandte Chemie - International Edition* **2009,** *48* (14), 2474-2499.

44. Horiuchi, T.; Miura, H.; Sumioka, K.; Uchida, S., High efficiency of dye-sensitized solar cells based on metal-free indoline dyes. *Journal of the American Chemical Society* **2004,** *126* (39), 12218-12219.

45. Ito, S.; Zakeeruddin, S. M.; Humphry-Baker, R.; Liska, P.; Charvet, R.; Comte, P.; Nazeeruddin, M. K.; Péchy, P.; Takata, M.; Miura, H.; Uchida, S.; Grätzel, M., High-efficiency organic-dye-sensitized solar cells controlled by nanocrystalline-TiO2 electrode thickness. *Advanced Materials* **2006,** *18* (9), 1202-1205.

46. Koumura, N.; Wang, Z. S.; Mori, S.; Miyashita, M.; Suzuki, E.; Hara, K., Alkyl-functionalized organic dyes for efficient molecular photovoltaics. *Journal of the American Chemical Society* **2006,** *128* (44), 14256-14257.

47. Hao, S.; Wu, J.; Huang, Y.; Lin, J., Natural dyes as photosensitizers for dye-sensitized solar cell. *Solar Energy* **2006,** *80* (2), 209-216.

48. Polo, A. S.; Itokazu, M. K.; Murakami Iha, N. Y., Metal complex sensitizers in dye-sensitized solar cells. *Coordination Chemistry Reviews* **2004,** *248* (13-14), 1343-1361.

49. Cao, Y. M.; Zhang, J.; Bai, Y.; Li, R. Z.; Zakeeruddin, S. M.; Gratzel, M.; Wang, P., Dye-sensitized solar cells with solvent-free ionic liquid electrolytes. *J Phys Chem C* **2008,** *112* (35), 13775-13781.

50. Wang, P.; Zakeeruddin, S. M.; Comte, P.; Exnar, I.; Gratzel, M., Gelation of ionic liquid-based electrolytes with silica nanoparticles for quasi-solid-state dye-sensitized solar cells. *J Am Chem Soc* **2003,** *125* (5), 1166-1167.

51. Li, B.; Wang, L. D.; Kang, B. N.; Wang, P.; Qiu, Y., Review of recent progress in solid-state dye-sensitized solar cells. *Sol Energ Mat Sol C* **2006,** *90* (5), 549-573.

52. Nogueira, A. F.; Durrant, J. R.; De Paoli, M. A., Dye-sensitized nanocrystalline solar cells employing a polymer electrolyte. *Adv Mater* **2001,** *13* (11), 826-+.

53. Wang, P.; Zakeeruddin, S. M.; Moser, J. E.; Nazeeruddin, M. K.; Sekiguchi, T.; Gratzel, M., A stable quasi-solid-state dye-sensitized solar cell with an amphiphilic ruthenium sensitizer and polymer gel

electrolyte (vol 2, pg 402, 2003). *Nature Materials* **2003,** *2* (7), 498-498.

54. Kang, M. G.; Kim, K. M.; Ryu, K. S.; Chang, S. H.; Park, N. G.; Hong, J. S.; Kim, K. J., Dye-sensitized TiO2 solar cells using polymer gel electrolytes based on PVdF-HFP. *J Electrochem Soc* **2004,** *151* (7), E257-E260.

55. Bai, Y.; Cao, Y. M.; Zhang, J.; Wang, M.; Li, R. Z.; Wang, P.; Zakeeruddin, S. M.; Gratzel, M., High-performance dye-sensitized solar cells based on solvent-free electrolytes produced from eutectic melts. *Nature Materials* **2008,** *7* (8), 626-630.

56. Kim, S. S.; Park, K. W.; Yum, J. H.; Sung, Y. E., Pt-NiO nanophase electrodes for dye-sensitized solar cells. *Sol Energ Mat Sol C* **2006,** *90* (3), 283-290.

57. Kim, S. S.; Nah, Y. C.; Noh, Y. Y.; Jo, J.; Kim, D. Y., Electrodeposited Pt for cost-efficient and flexible dye-sensitized solar cells. *Electrochim Acta* **2006,** *51* (18), 3814-3819.

58. Kay, A.; Gratzel, M., Low cost photovoltaic modules based on dye sensitized nanocrystalline titanium dioxide and carbon powder. *Sol Energ Mat Sol C* **1996,** *44* (1), 99-117.

59. Imoto, K.; Takahashi, K.; Yamaguchi, T.; Komura, T.; Nakamura, J.; Murata, K., High-performance carbon counter electrode for dye-sensitized solar cells. *Sol Energ Mat Sol C* **2003,** *79* (4), 459-469.

60. Murakami, T. N.; Ito, S.; Wang, Q.; Nazeeruddin, M. K.; Bessho, T.; Cesar, I.; Liska, P.; Humphry-Baker, R.; Comte, P.; Pechy, P.; Gratzel, M., Highly efficient dye-sensitized solar cells based on carbon black counter electrodes. *J Electrochem Soc* **2006,** *153* (12), A2255-A2261.

61. Abayev, I.; Zaban, A.; Fabregat-Santiago, F.; Bisquert, J., Electronic conductivity in nanostructured TiO2 films permeated with electrolyte. *Phys Status Solidi A* **2003,** *196* (1), R4-R6.

62. Agrell, H. G.; Boschloo, G.; Hagfeldt, A., Conductivity studies of nanostructured TiO2 films permeated with electrolyte. *J Phys Chem B* **2004,** *108* (33), 12388-12396.

63. Kroeze, J. E.; Savenije, T. J.; Warman, J. M., Electrodeless determination of the trap density, decay kinetics, and charge separation efficiency of dye-sensitized nanocrystalline TiO2. *J Am Chem Soc* **2004,** *126* (24), 7608-7618.

64. Lobato, K.; Peter, L. M., Direct measurement of the temperature coefficient of the electron quasi-Fermi level in dye-sensitized nanocrystalline solar cells using a titanium sensor electrode. *J. Phys. Chem. B* **2006,** *110* (43), 21920-21923.

65. Peter, L. M., Characterization and modeling of dye-sensitized solar cells. *J Phys Chem C* **2007,** *111* (18), 6601-6612.

66. Jiang, C. L.; Zhang, W. Q.; Zou, G. F.; Yu, W. C.; Qian, Y. T., Precursor-induced hydrothermal synthesis of flowerlike cupped-end microrod bundles of ZnO. *J Phys Chem B* **2005,** *109* (4), 1361-1363.

67. Huang, M. H.; Wu, Y. Y.; Feick, H.; Tran, N.; Weber, E.; Yang, P. D., Catalytic growth of zinc oxide nanowires by vapor transport. *Adv Mater* **2001,** *13* (2), 113-116.

68. Hu, P.; Liu, Y. Q.; Wang, X. B.; Fu, L.; Zhu, D. B., Tower-like structure of ZnO nanocolumns. *Chem Commun* **2003,** (11), 1304-1305.

69. Pan, Z. W.; Dai, Z. R.; Wang, Z. L., Nanobelts of semiconducting oxides. *Science* **2001,** *291* (5510), 1947-1949.

70. Keis, K.; Vayssieres, L.; Rensmo, H.; Lindquist, S. E.; Hagfeldt, A., Photoelectrochemical properties of nano- to microstructured ZnO electrodes. *J Electrochem Soc* **2001,** *148* (2), A149-A155.

71. Rani, S.; Suri, P.; Shishodia, P. K.; Mehra, R. M., Synthesis of nanocrystalline ZnO powder via sol-gel route for dye-sensitized solar cells. *Sol Energ Mat Sol C* **2008,** *92* (12), 1639-1645.

72. Redmond, G.; Fitzmaurice, D.; Graetzel, M., Visible-Light Sensitization by Cis-Bis(Thiocyanato)Bis(2,2'-Bipyridyl-4,4'-Dicarboxylato)Ruthenium(Ii) of a Transparent Nanocrystalline Zno Film Prepared by Sol-Gel Techniques. *Chem Mater* **1994,** *6* (5), 686-691.

73. Kontos, A. I.; Kontos, A. G.; Tsoukleris, D. S.; Bernard, M. C.; Spyrellis, N.; Falaras, P., Nanostructured TiO(2) films for DSSCS prepared by combining doctor-blade and sol-gel techniques. *J Mater Process Tech* **2008,** *196* (1-3), 243-248.

74. Spanhel, L.; Anderson, M. A., Semiconductor Clusters in the Sol-Gel Process - Quantized Aggregation, Gelation, and Crystal-Growth in Concentrated Zno Colloids. *J Am Chem Soc* **1991,** *113* (8), 2826-2833.

75. Nonomura, K.; Yoshida, T.; Schlettwein, D.; Minoura, H., One-step electrochemical synthesis of ZnO/Ru(dcbpy)(2)(NCS)(2) hybrid thin films and their photoelectrochemical properties. *Electrochim Acta* **2003,** *48* (20-22), 3071-3078.

76. Basu, P. K.; Saha, N.; Maji, S.; Saha, H.; Basu, S., Nanoporous ZnO thin films deposited by electrochemical anodization: effect of UV light. *J Mater Sci-Mater El* **2008,** *19* (6), 493-499.

77. Hosono, E.; Fujihara, S.; Kimura, T.; Imai, H., Growth of layered basic zinc acetate in methanolic solutions and its pyrolytic transformation into porous zinc oxide films. *J Colloid Interf Sci* **2004,** *272* (2), 391-398.

78. Xi, Y. Y.; Hsu, Y. F.; Djurisic, A. B.; Chan, W. K., Electrochemical synthesis of ZnO nanoporous films at low temperature and their application in dye-sensitized solar cells. *J Electrochem Soc* **2008,** *155* (9), D595-D598.

79. Shin, Y. J.; Lee, J. H.; Park, J. H.; Park, N. G., Enhanced photovoltaic properties of SiO2-treated ZnO nanocrystalline electrode for dye-sensitized solar cell. *Chem Lett* **2007,** *36* (12), 1506-1507.

80. Shin, Y. J.; Kim, K. S.; Park, N. G.; Ryu, K. S.; Chang, S. H., Enhancement of photovoltaic properties of Ti-modified nanocrystalline ZnO electrode for dye-sensitized solar cell. *B Korean Chem Soc* **2005,** *26* (12), 1929-1930.

81. Pal, B.; Sharon, M., Enhanced photocatalytic activity of highly porous ZnO thin films prepared by sol-gel process. *Mater Chem Phys* **2002,** *76* (1), 82-87.

82. Xu, J. F.; Ji, W.; Wang, X. B.; Shu, H.; Shen, Z. X.; Tang, S. H., Temperature dependence of the Raman scattering spectra of Zn/ZnO nanoparticles. *J Raman Spectrosc* **1998,** *29* (7), 613-615.

83. Exarhos, G. J.; Sharma, S. K., Influence of processing variables on the structure and properties of ZnO films. *Thin Solid Films* **1995,** *270* (1-2), 27-32.

84. Murakami, T. N.; Gratzel, M., Counter electrodes for DSC: Application of functional materials as catalysts. *Inorg Chim Acta* **2008,** *361* (3), 572-580.

85. Sun, H. C.; Qin, D.; Huang, S. Q.; Guo, X. Z.; Li, D. M.; Luo, Y. H.; Meng, Q. B., Dye-sensitized solar cells with NiS counter electrodes electrodeposited by a potential reversal technique. *Energ Environ Sci* **2011,** *4* (8), 2630-2637.

86. Wang, M. K.; Anghel, A. M.; Marsan, B.; Ha, N. L. C.; Pootrakulchote, N.; Zakeeruddin, S. M.; Gratzel, M., CoS Supersedes Pt as Efficient Electrocatalyst for Triiodide Reduction in Dye-Sensitized Solar Cells. *J Am Chem Soc* **2009,** *131* (44), 15976-+.

87. Li, G. R.; Song, J.; Pan, G. L.; Gao, X. P., Highly Pt-like electrocatalytic activity of transition metal nitrides for dye-sensitized solar cells. *Energ Environ Sci* **2011,** *4* (5), 1680-1683.

88. Li, G. R.; Wang, F.; Jiang, Q. W.; Gao, X. P.; Shen, P. W., Carbon Nanotubes with Titanium Nitride as a Low-Cost Counter-Electrode Material for Dye-Sensitized Solar Cells. *Angew Chem Int Edit* **2010,** *49* (21), 3653-3656.

89. Wu, M. X.; Lin, X. A.; Hagfeldt, A.; Ma, T. L., Low-Cost Molybdenum Carbide and Tungsten Carbide Counter Electrodes for Dye-Sensitized Solar Cells. *Angew Chem Int Edit* **2011,** *50* (15), 3520-3524.

90. Jang, J. S.; Ham, D. J.; Ramasamy, E.; Lee, J.; Lee, J. S., Platinum-free tungsten carbides as an efficient counter electrode for dye sensitized solar cells. *Chem Commun* **2010,** *46* (45), 8600-8602.

91. Wu, M. X.; Lin, X.; Wang, T. H.; Qiu, J. S.; Ma, T. L., Low-cost dye-sensitized solar cell based on nine kinds of carbon counter electrodes. *Energ Environ Sci* **2011,** *4* (6), 2308-2315.

92. Lee, K. S.; Lee, W. J.; Park, N. G.; Kim, S. O.; Park, J. H., Transferred vertically aligned N-doped carbon nanotube arrays: use in dye-sensitized solar cells as counter electrodes. *Chem Commun* **2011,** *47* (14), 4264-4266.

93. Han, J.; Kim, H.; Kim, D. Y.; Jo, S. M.; Jang, S. Y., Water-Soluble Polyelectrolyte-Grafted Multiwalled Carbon Nanotube Thin Films for Efficient Counter Electrode of Dye-Sensitized Solar Cells. *Acs Nano* **2010,** *4* (6), 3503-3509.

94. Lee, W. J.; Ramasamy, E.; Lee, D. Y.; Song, J. S., Efficient Dye-Sensitized Cells with Catalytic Multiwall Carbon Nanotube Counter Electrodes. *Acs Appl Mater Inter* **2009,** *1* (6), 1145-1149.

95. Joshi, P.; Zhang, L. F.; Chen, Q. L.; Galipeau, D.; Fong, H.; Qiao, Q. Q., Electrospun Carbon Nanofibers as Low-Cost Counter Electrode for Dye-Sensitized Solar Cells. *Acs Appl Mater Inter* **2010,** *2* (12), 3572-3577.

96. Choi, H.; Kim, H.; Hwang, S.; Han, Y.; Jeon, M., Graphene counter electrodes for dye-sensitized solar cells prepared by electrophoretic deposition. *J Mater Chem* **2011,** *21* (21), 7548-7551.

97. Kavan, L.; Yum, J. H.; Gratzel, M., Optically Transparent Cathode for Dye-Sensitized Solar Cells Based on Graphene Nanoplatelets. *Acs Nano* **2011,** *5* (1), 165-172.

98. Roy-Mayhew, J. D.; Bozym, D. J.; Punckt, C.; Aksay, I. A., Functionalized Graphene as a Catalytic Counter Electrode in Dye-Sensitized Solar Cells. *Acs Nano* **2010,** *4* (10), 6203-6211.

99. Veerappan, G.; Bojan, K.; Rhee, S. W., Sub-micrometer-sized Graphite As a Conducting and Catalytic Counter Electrode for Dye-sensitized Solar Cells. *Acs Appl Mater Inter* **2011,** *3* (3), 857-862.

100. Fang, B. Z.; Fan, S. Q.; Kim, J. H.; Kim, M. S.; Kim, M.; Chaudhari, N. K.; Ko, J.; Yu, J. S., Incorporating Hierarchical Nanostructured Carbon Counter Electrode into Metal-Free Organic Dye-Sensitized Solar Cell. *Langmuir* **2010,** *26* (13), 11238-11243.

101. Ramasamy, E.; Lee, J., Large-pore sized mesoporous carbon electrocatalyst for efficient dye-sensitized solar cells. *Chem Commun* **2010,** *46* (12), 2136-2138.

102. Wang, G. Q.; Xing, W.; Zhuo, S. P., Application of mesoporous carbon to counter electrode for dye-sensitized solar cells. *J Power Sources* **2009,** *194* (1), 568-573.

103. Kruk, M.; Jaroniec, M.; Ko, C. H.; Ryoo, R., Characterization of the porous structure of SBA-15. *Chem Mater* **2000,** *12* (7), 1961-1968.

104. Zhao, D. Y.; Feng, J. L.; Huo, Q. S.; Melosh, N.; Fredrickson, G. H.; Chmelka, B. F.; Stucky, G. D., Triblock copolymer syntheses of mesoporous silica with periodic 50 to 300 angstrom pores. *Science* **1998,** *279* (5350), 548-552.

105. Lee, K. T.; Ji, X. L.; Rault, M.; Nazar, L. F., Simple Synthesis of Graphitic Ordered Mesoporous Carbon Materials by a Solid-State Method Using Metal Phthalocyanines. *Angew Chem Int Edit* **2009,** *48* (31), 5661-5665.

106. Kim, N. S.; Lee, Y. T.; Park, J.; Han, J. B.; Choi, Y. S.; Choi, S. Y.; Choo, J.; Lee, G. H., Vertically aligned carbon nanotubes grown by pyrolysis of iron, cobalt, and nickel phthalocyanines. *J Phys Chem*

B **2003,** *107* (35), 9249-9255.

107. Lv, L.; Su, F.; Zhao, X. S., Incorporation of hybrid elements into microporous titanosilicate ETS-10: An approach to improving its adsorption properties toward Pb2+. *Micropor Mesopor Mat* **2007,** *101* (3), 355-362.

108. Trancik, J. E.; Barton, S. C.; Hone, J., Transparent and catalytic carbon nanotube films. *Nano Lett* **2008,** *8* (4), 982-987.

109. Jiang, Q. W.; Li, G. R.; Wang, F.; Gao, X. P., Highly ordered mesoporous carbon arrays from natural wood materials as counter electrode for dye-sensitized solar cells. *Electrochem Commun* **2010,** *12* (7), 924-927.

110. Ramasamy, E.; Lee, W. J.; Lee, D. Y.; Song, J. S., Spray coated multi-wall carbon nanotube counter electrode for tri-iodide (I-3(-)) reduction in dye-sensitized solar cells. *Electrochem Commun* **2008,** *10* (7), 1087-1089.

111. Cha, S. I.; Koo, B. K.; Seo, S. H.; Lee, D. Y., Pt-free transparent counter electrodes for dye-sensitized solar cells prepared from carbon nanotube micro-balls. *J Mater Chem* **2010,** *20* (4), 659-662.

112. Zukalova, M.; Prochazka, J.; Zukal, A.; Yum, J. H.; Kavan, L.; Graetzel, M., Organized Mesoporous TiO2 Films Stabilized by Phosphorus: Application for Dye-Sensitized Solar Cells. *J Electrochem Soc* **2010,** *157* (1), H99-H103.

113. Hong, W. J.; Xu, Y. X.; Lu, G. W.; Li, C.; Shi, G. Q., Transparent graphene/PEDOT-PSS composite films as counter electrodes of dye-sensitized solar cells. *Electrochem Commun* **2008,** *10* (10), 1555-1558.

114. Kou, R.; Shao, Y. Y.; Mei, D. H.; Nie, Z. M.; Wang, D. H.; Wang, C. M.; Viswanathan, V. V.; Park, S.; Aksay, I. A.; Lin, Y. H.; Wang, Y.; Liu, J., Stabilization of Electrocatalytic Metal Nanoparticles at Metal-Metal Oxide-Graphene Triple Junction Points. *J Am Chem Soc* **2011,** *133* (8), 2541-2547.

115. Chen, X. M.; Wu, G. H.; Chen, J. M.; Chen, X.; Xie, Z. X.; Wang, X. R., Synthesis of "Clean" and Well-Dispersive Pd Nanoparticles with Excellent Electrocatalytic Property on Graphene Oxide. *J Am Chem Soc* **2011,** *133* (11), 3693-3695.

116. Zhou, X. Z.; Huang, X.; Qi, X. Y.; Wu, S. X.; Xue, C.; Boey, F. Y. C.; Yan, Q. Y.; Chen, P.; Zhang, H., In Situ Synthesis of Metal Nanoparticles on Single-Layer Graphene Oxide and Reduced Graphene Oxide Surfaces. *J Phys Chem C* **2009,** *113* (25), 10842-10846.

117. Moon, I. K.; Lee, J.; Ruoff, R. S.; Lee, H., Reduced graphene oxide by chemical graphitization. *Nat Commun* **2010,** *1*.

118. Gao, W.; Alemany, L. B.; Ci, L. J.; Ajayan, P. M., New insights into the structure and reduction of graphite oxide. *Nat Chem* **2009,** *1* (5), 403-408.

119. Watcharotone, S.; Dikin, D. A.; Stankovich, S.; Piner, R.; Jung, I.; Dommett, G. H. B.; Evmenenko, G.; Wu, S. E.; Chen, S. F.; Liu, C. P.; Nguyen, S. T.; Ruoff, R. S., Graphene-silica composite thin films as transparent conductors. *Nano Lett* **2007,** *7* (7), 1888-1892.

120. Mattevi, C.; Eda, G.; Agnoli, S.; Miller, S.; Mkhoyan, K. A.; Celik, O.; Mostrogiovanni, D.; Granozzi, G.; Garfunkel, E.; Chhowalla, M., Evolution of Electrical, Chemical, and Structural Properties of Transparent and Conducting Chemically Derived Graphene Thin Films. *Adv Funct Mater* **2009,** *19* (16), 2577-2583.

121. Eda, G.; Fanchini, G.; Chhowalla, M., Large-area ultrathin films of reduced graphene oxide as a transparent and flexible electronic material. *Nat Nanotechnol* **2008,** *3* (5), 270-274.

122. Perdew, J. P.; Burke, K.; Ernzerhof, M., Generalized gradient approximation made simple. *Phys Rev Lett* **1996,** *77* (18), 3865-3868.

123. Kresse, G.; Furthmuller, J., Efficient iterative schemes for ab initio total-energy calculations using a plane-wave basis set. *Phys Rev B* **1996,** *54* (16), 11169-11186.

124. Kohn, W.; Sham, L. J., Self-Consistent Equations Including Exchange and Correlation Effects. *Phys Rev* **1965,** *140* (4A), 1133-&.

125. Loh, K. P.; Bao, Q. L.; Eda, G.; Chhowalla, M., Graphene oxide as a chemically tunable platform for optical applications. *Nat Chem* **2010,** *2* (12), 1015-1024.

126. Seo, H.; Son, M. K.; Shin, I.; Kim, J. K.; Lee, K. J.; Prabakar, K.; Kim, H. J., Faster dye-adsorption of dye-sensitized solar cells by applying an electric field. *Electrochim Acta* **2010,** *55* (13), 4120-4123.

127. Wang, G. Q.; Lin, R. F.; Lin, Y.; Li, X. P.; Zhou, X. W.; Xiao, X. R., A novel high-performance counter electrode for dye-sensitized solar cells. *Electrochim Acta* **2005,** *50* (28), 5546-5552.

128. Nazeeruddin, M. K.; De Angelis, F.; Fantacci, S.; Selloni, A.; Viscardi, G.; Liska, P.; Ito, S.; Bessho, T.; Gratzel, M., Combined experimental and DFT-TDDFT computational study of photoelectrochemical cell ruthenium sensitizers. *J Am Chem Soc* **2005,** *127* (48), 16835-16847.

129. Lee, C. R.; Kim, H. S.; Jang, I. H.; Im, J. H.; Park, N. G., Pseudo First-Order Adsorption Kinetics of N719 Dye on TiO2 Surface. *Acs Appl Mater Inter* **2011,** *3* (6), 1953-1957.

130. Sauvage, F.; Decoppet, J. D.; Zhang, M.; Zakeeruddin, S. M.; Comte, P.; Nazeeruddin, M.; Wang, P.; Gratzel, M., Effect of Sensitizer Adsorption Temperature on the Performance of Dye-Sensitized Solar Cells. *J Am Chem Soc* **2011,** *133* (24), 9304-9310.

131. Fredin, K.; Anderson, K. F.; Duffy, N. W.; Wilson, G. J.; Fell, C. J.; Hagberg, D. P.; Sun, L. C.; Bach, U.; Lindquist, S. E., Effect on Cell Efficiency following Thermal Degradation of Dye-Sensitized Mesoporous Electrodes Using N719 and D5 Sensitizers. *J Phys Chem C* **2009,** *113* (43), 18902-18906.

132. Murakoshi, K.; Kano, G.; Wada, Y.; Yanagida, S.; Miyazaki, H.; Matsumoto, M.; Murasawa, S., Importance of Binding States between Photosensitizing Molecules and the Tio2 Surface for Efficiency in a Dye-Sensitized Solar-Cell. *J Electroanal Chem* **1995,** *396* (1-2), 27-34.

133. Leon, C. P.; Kador, L.; Peng, B.; Thelakkat, M., Characterization of the adsorption of ru-bpy dyes on mesoporous TiO2 films with UV-Vis, Raman, and FTIR spectroscopies. *J Phys Chem B* **2006,** *110* (17), 8723-8730.

134. Finnie, K. S.; Bartlett, J. R.; Woolfrey, J. L., Vibrational spectroscopic study of the coordination of (2,2 '-bipyridyl-4,4 '-dicarboxylic acid)ruthenium(II) complexes to the surface of nanocrystalline titania. *Langmuir* **1998,** *14* (10), 2744-2749.

135. Hirose, F.; Shikaku, M.; Kimura, Y.; Niwano, M., IR Study on N719 Dye Adsorption with High Temperature Dye Solution for Highly Efficient Dye-Sensitized Solar Cells. *J Electrochem Soc* **2010,** *157* (11), B1578-B1581.

136. Philippopoulos, A. I.; Terzis, A.; Raptopoulou, C. P.; Catalano, V. J.; Falaras, P., Synthesis, characterization, and sensitizing properties of heteroleptic Ru-II complexes based on 2,6-bis(1-pyrazolyl)pyridine and 2,2'-bipyridine-4,4'-dicarboxylic acid ligands. *Eur J Inorg Chem* **2007,** (36), 5633-5644.

137. Hoshikawa, T.; Yamada, M.; Kikuchi, R.; Eguchi, K., Impedance analysis of internal resistance affecting the photoelectrochemical performance of dye-sensitized solar cells. *J Electrochem Soc* **2005,** *152* (2), E68-E73.

138. Han, L. Y.; Koide, N.; Chiba, Y.; Mitate, T., Modeling of an equivalent circuit for dye-sensitized solar cells. *Appl Phys Lett* **2004,** *84* (13), 2433-2435.

139. Bisquert, J.; Vikhrenko, V. S., Interpretation of the time constants measured by kinetic techniques in nanostructured semiconductor electrodes and dye-sensitized solar cells. *J Phys Chem B* **2004,** *108*

(7), 2313-2322.

140. Hirose, F.; Kuribayashi, K.; Shikaku, M.; Narita, Y.; Takahashi, Y.; Kimura, Y.; Niwano, M., Adsorption Density Control of N719 on TiO2 Electrodes for Highly Efficient Dye-Sensitized Solar Cells. *J Electrochem Soc* **2009**, *156* (9), B987-B990.

141. Hirose, F.; Kuribayashi, K.; Suzuki, T.; Narita, Y.; Kimura, Y.; Niwano, M., UV treatment effect on TiO(2) electrodes in dye-sensitized solar cells with N719 sensitizer investigated by infrared absorption spectroscopy. *Electrochem Solid St* **2008**, *11* (7), A109-A111.

142. Anderson, N. A.; Lian, T. Q., Ultrafast electron transfer at the molecule-semiconductor nanoparticle interface. *Annu Rev Phys Chem* **2005**, *56*, 491-519.

143. Benko, G.; Kallioinen, J.; Korppi-Tommola, J. E. I.; Yartsev, A. P.; Sundstrom, V., Photoinduced ultrafast dye-to-semiconductor electron injection from nonthermalized and thermalized donor states. *J Am Chem Soc* **2002**, *124* (3), 489-493.

144. Kuang, D. B.; Ito, S.; Wenger, B.; Klein, C.; Moser, J. E.; Humphry-Baker, R.; Zakeeruddin, S. M.; Gratzel, M., High molar extinction coefficient heteroleptic ruthenium complexes for thin film dye-sensitized solar cells. *J Am Chem Soc* **2006**, *128* (12), 4146-4154.

145. Asbury, J. B.; Hao, E.; Wang, Y. Q.; Ghosh, H. N.; Lian, T. Q., Ultrafast electron transfer dynamics from molecular adsorbates to semiconductor nanocrystalline thin films. *J Phys Chem B* **2001**, *105* (20), 4545-4557.

146. Watson, D. F.; Meyer, G. J., Electron injection at dye-sensitized semiconductor electrodes. *Annu Rev Phys Chem* **2005**, *56*, 119-156.

147. Kallioinen, J.; Benko, G.; Sundstrom, V.; Korppi-Tommola, J. E. I.; Yartsev, A. P., Electron transfer from the singlet and triplet excited states of Ru(dcbpy)(2)(NCS)(2) into nanocrystalline TiO2 thin films. *J Phys Chem B* **2002**, *106* (17), 4396-4404.

148. Tachibana, Y.; Nazeeruddin, M. K.; Gratzel, M.; Klug, D. R.; Durrant, J. R., Electron injection kinetics for the nanocrystalline TiO2 films sensitised with the dye (Bu4N)(2)Ru(dcbpyH)(2)(NCS)(2). *Chem Phys* **2002**, *285* (1), 127-132.

149. Asbury, J. B.; Anderson, N. A.; Hao, E. C.; Ai, X.; Lian, T. Q., Parameters affecting electron injection dynamics from ruthenium dyes to titanium dioxide nanocrystalline thin film. *J Phys Chem B* **2003**, *107* (30), 7376-7386.

150. Bruggemann, B.; Organero, J. A.; Pascher, T.; Pullerits, T.; Yartsev, A., Control of electron transfer pathways in a dye-sensitized solar cell. *Phys Rev Lett* **2006**, *97* (20).

151. Kelly, C. A.; Farzad, F.; Thompson, D. W.; Stipkala, J. M.; Meyer, G. J., Cation-controlled interfacial charge injection in sensitized nanocrystalline TiO2. *Langmuir* **1999**, *15* (20), 7047-7054.

152. Tachibana, Y.; Haque, S. A.; Mercer, I. P.; Moser, J. E.; Klug, D. R.; Durrant, J. R., Modulation of the rate of electron injection in dye-sensitized nanocrystalline TiO2 films by externally applied bias. *J Phys Chem B* **2001**, *105* (31), 7424-7431.

153. Asbury, J. B.; Hao, E. C.; Wang, Y. Q.; Lian, T. Q., Bridge length-dependent ultrafast electron transfer from Re polypyridyl complexes to nanocrystalline TiO2 thin films studied by femtosecond infrared spectroscopy. *J Phys Chem B* **2000**, *104* (50), 11957-11964.

154. Pollard, J. A.; Zhang, D. S.; Downing, J. A.; Knorr, F. J.; McHale, J. L., Solvent effects on interfacial electron transfer from Ru(4,4 '-dicarboxylic acid-2,2 '-bipyridine)(2)(NCS)(2) to nanoparticulate TiO2: Spectroscopy and solar photoconversion. *J Phys Chem A* **2005**, *109* (50), 11443-11452.

155. She, C. X.; Guo, J. C.; Lian, T. Q., Comparison of electron injection dynamics from re-bipyridyl

complexes to TiO2 nanocrystalline thin films in different solvent environments. *J Phys Chem B* **2007,** *111* (24), 6903-6912.

156. Wenger, B.; Gratzel, M.; Moser, J. E., Rationale for kinetic heterogeneity of ultrafast light-induced electron transfer from Ru(II) complex sensitizers to nanocrystalline TiO2. *J Am Chem Soc* **2005,** *127* (35), 12150-12151.

157. Nazeeruddin, M. K.; Humphry-Baker, R.; Liska, P.; Gratzel, M., Investigation of sensitizer adsorption and the influence of protons on current and voltage of a dye-sensitized nanocrystalline TiO2 solar cell. *J Phys Chem B* **2003,** *107* (34), 8981-8987.